![Tampere University logo] Tampere University

TIINA VUORINEN

Development of Printed Conformable Sensors

TIINA VUORINEN

Development of Printed Conformable Sensors

ACADEMIC DISSERTATION
Tampere University, Faculty of Information Technology and Communication Sciences
Finland

Responsible supervisor and Custos	Professor Matti Mäntysalo Tampere University Finland	
Pre-examiners	Associate Professor Tse Nga (Tina) Ng University of California USA	Professor Ravinder Dahia University of Glasgow Scotland
Opponent	Assistant Professor Shweta Agarwala Aarhus University Denmark	

The originality of this thesis has been checked using the Turnitin OriginalityCheck service.

Cover design: Roihu Inc.

PREFACE

First of all, I would like to express my gratitude to my supervisor Prof. Matti Mäntysalo for his time and effort he has given me throughout my doctoral studies. I would also like to thank my master's thesis supervisor Prof. Donald Lupo and my bachelor's thesis supervisor Assoc. Prof. Sampo Tuukkanen for giving me the opportunity to work in this field. I want to thank Prof. Karl-Heinz Bock and Martin Schubert, M.Sc., from TU Dresden, for the international experience and for getting to work in their laboratory.

Million thanks to all the co-authors, and especially without these people: Assist. Prof. Antti Vehkaoja, Thomas Kraft Ph.D., Mari Zakrzewski, D.Sc., Kai Noponen, M.Sc., Vala Jeyhani, M.Sc., and Timo Onnia, M.Sc. I would not have been able to make these articles. I have been privileged to share the ups and downs with some of the most awesome colleagues/friends. For that reason, I would especially like to thank Juha Niittynen, D.Sc., Jari Keskinen, D.Sc., Mika-Matti Laurila, D.Sc., Suvi Lehtimäki, D.Sc., Marika Janka, D.Sc., Behnam Khorramdel, D.Sc., Riikka Mikkonen, M.Sc., Anna Railanmaa, M.Sc., Milad Mosallaei, M.Sc., Hanna Christophliemk, M.Sc., and Vänni Panula, M.Sc. Kiitos! Also, thanks to all the other colleagues, I have had the opportunity to work with.

With all my heart, I would like to thank my parents and my brother for being there for me.

Finally, Petri, Emma, and Amalia, you are my everything.

Tampereella 25.10.2020

Tiina Vuorinen

ABSTRACT

Electronics is already controlling a large number of everyday items. Due to that, electronics are found from all kinds of devices and surfaces. The traditional rigid circuit boards are the most common options in adding electronics to the surroundings. However, a new class of electronics is needed to enable the transition to a higher level of seamless integration. This transition can be done with so-called conformable electronics. Using printed electronics could bring down material consumption and allow the use of new materials in conformable electronics. In the present thesis, three different printing methods – spray coating, screen printing, and inkjet printing – were investigated to fabricate different conformable electronics: transparent touch panel, ECG electrodes, and on-skin temperature sensors. It was also studied how the printed electrode patch compares to the commercial single electrodes and how well they function in real-life situations.

A transparent touch panel with 64.7% transparency was fabricated using spray-coated graphene/PEDOT:PSS ink on a piezoelectric film. The touch panel exhibited 35 pC N^{-1} sensitivity, and it was able to be used both in dry and moist environments. Screen printing and stretchable silver inks were used to manufacture ECG monitoring patches on a stretchable polyurethane substrate. The ECG signal quality of the printed patch was compared with commercial electrodes in volunteer trials to verify the functionality before testing with cardiac patients. The overall signal quality was similar, and thus the electrode patches were tested with cardiac patients. E-jet printing was used to fabricate silver temperature sensors on bacterial nanocellulose substrate with a 20 µm line width. Also, inkjet-printed graphene/PEDOT:PSS temperature sensors were fabricated on thermoplastic polyurethane. The temperature sensors exhibited TRC of 0.06% that does not compete with the most efficient sensors but indicates that alternative substrate materials such as nanocellulose can be used instead of plastics. Additionally, inherently conformable materials like thermoplastic polyurethane and graphene/PEDOT:PSS ink can be used to make temperature sensors.

Printed structures do not yet compete with the efficiency with some of the already existing systems, but the benefits arise from the novel materials and reduced material consumption in conformable electronics manufacturing. However, for example, the ECG monitoring system, with stretchable conductors and soft substrate, provided similar signal quality as its commercial counterpart. Also, novel materials and fabrications processes enable new applications that are not limited by the traditional electronics fabrication processes and materials.

CONTENTS

List of Figures

List of Tables

LIST OF SYMBOLS AND ABBREVIATIONS

ADC	Analog-to-Digital Converter
Ag	Silver
AgCl	Silver Chloride
CIJ	Continuous Inkjet
CNT	Carbon Nanotubes
CTE	Coefficient of Thermal Expansion
CVD	Cardio Vascular Disease
DoD	Drop-on-Demand
EES	Epidermal Electronic System
ECG	Electrocardiogram
E-jet	Electrohydrodynamic inkjet
γ	Interface tension
IoT	Internet-of-Things
ITO	Indium Tin Oxide
LED	Light-Emitting Diode
MEMS	Microelectromechanical System
PCB	Printed Circuit Board
PDMS	Poly(dimethylsiloxane)
PEDOT:PSS	Poly(3,4-ethylenedioxythiophene poly(sturenesulfonate))
PET	Poly(ethylene terephthalate)
PI	Polyimide
PLA	Polylactide
PUR	Polyurethane
PVA	Poly(vinyl alcohol)
PVDF	Poly(1,1-difluoroethylene)
TCR	Temperature Coefficient of Resistance
TPU	Thermoplastic Polyurethane
TSV	Through-Silicon Via
θ	Contact angle
UV	Ultraviolet
VF2	1,1-difluoroethylene
wt%	Weight percentage

ORIGINAL PUBLICATIONS

Publication I   Vuorinen T., Zakrzewski M., Rajala S., Lupo D., Vanhala J., Palovuori K. and Tuukkanen S. "Printable, transparent, and flexible touch panels working in sunlight and moist environments," Adv. Funct. Mater., vol. 24, no. 40, 2014.

Publication II   Vuorinen T., Vehkaoja A., Jeyhani V., Noponen K., Onubeze A., Kankkunen T., Puuronen A. K., Nurmentaus S., Preejith P. S., Joseph J., Seppänen T., Sivaprakasam M. and Mäntysalo M. "Printed, skin-mounted hybrid system for ECG measurements," 2016 6th Electronic System-Integration Technology Conference (ESTC). pp. 1–6, 2016.

Publication III   Vuorinen T., Noponen K., Vehkaoja A., Onnia T., Laakso E., Leppänen S., Mansikkamäki K., Seppänen T. and Mäntysalo M. "Validation of Printed, Skin-Mounted Multilead Electrode for ECG Measurements," Adv. Mater. Technol., vol. 4, no. 9, p. 1900246, Jun. 2019.

Publication IV   Vuorinen T., Noponen K., Jeyhani V., Aslam A., Junttila J. Tulppo M., Kaikkonen K., Huikuri H., Seppänen T., Mäntysalo M. and Vehkaoja A. "Unobtrusive, Low-Cost Out-of-Hospital and In-Hospital Measurement and Monitoring System" Adv. Int. Syst.

Publication V   Vuorinen T., Laurila M.-M., Mangayil R., Karp M., and Mäntysalo M. "High resolution E-jet printed temperature sensor on artificial skin," in IFMBE Proceedings, 2018, vol. 65.

Publication VI   Vuorinen T., Niittynen J., Kankkunen T., Kraft T. M., and Mäntysalo M. "Inkjet-printed graphene/PEDOT:PSS temperature sensors on a skin-conformable polyurethane substrate" Sci. Rep., vol. 6, 2016.

1   INTRODUCTION

Rigid printed circuit boards (PCBs) have been the basic building blocks for electronics for several decades. The first patent about creating an electrical path directly on an insulated surface was filed already in 1925 by Charles Ducas [1], and nowadays, the PCBs can be found all around us. Cars, mobile phones, washing machines, smartwatches, and many other everyday items are functioning due to the invention of printed circuit boards. Traditional PCBs are rigid, so they do not combine well with complex surfaces without adapters. Recently, the development is going towards intrinsically adaptable electronics that can be better integrated with different surfaces [2][3][4]. This type of conformable electronics can be attached to surrounding infrastructures or even to a human body.

Several applications would highly benefit from conformability. Different kinds of touch panels can be found from all around us, and measuring and monitoring the human body is widely done both in the fitness tracking and in the medical field. Figure 1 presents three different concepts for conformable electronics; one to control the surroundings and two to sensor different physiological phenomena. For example, a window may have a touch panel to control the light transmission properties, or a human body could have wireless temperature sensors or ECG recorders attached to it.

Conformable electronics have been widely studied and fabricated using traditional electronics fabrication methods such as evaporation and lithography processes [5]. Photolithography is a well-established microfabrication process to pattern different substrates, and it includes a series of different process steps and chemical treatments [6]. Printed electronics, in which electronic devices and systems are fabricated using conventional printing technologies, could be used to overcome the multiple process steps and excessive material usage. Printed electronics offers the possibility to simplify the manufacturing processes, reduce the raw materials consumption, and bring down the fabrication costs compared to, for example, photolithography included processes. Besides, the combination of highly customizable materials and a wide range of different printing technologies enables

the fabrication of totally new structures [7]. For example, stretchable inks can be used together with stretchable substrates to make highly conformable structures [8]. Different skin-attached electrodes and sensor systems are disposable and should integrate well with the skin [9]. For that reason, they are an example of applications that would highly benefit from advantages such as new material options, low-cost, and low material consumption.
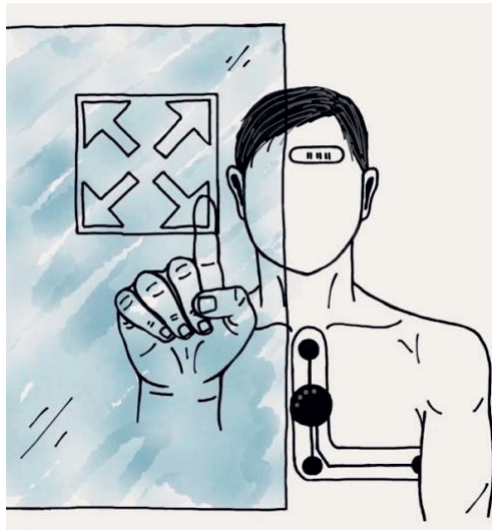
Figure 1. Conformable electronics both on glass and on human skin.

1.1   Aim and scope of the thesis

This thesis aims to investigate if different printing methods, substrate materials, and inks can be used to fabricate conformable electronics and what would be their electrical functionality. In addition, the aim was to verify how well the novel printed electrodes compare to the commercial electrodes and how they function in real-life situations. Spray coating was used to fabricate touch panels, two different inkjet printers were used in temperature sensor fabrication, and ECG monitoring patches were screen printed.

First, the spray coating method is used to fabricate transparent graphene/PEDOT:PSS touch panels on a flexible PVDF substrate. This is followed by the fabrication of ECG monitoring patches using screen printing. The ECG patches are then compared with the commercial ECG electrodes in different

physical activities to investigate the motion artefacts. After motion artefact studies, the ECG patches were combined with a measurement unit, and these monitoring systems were tested with cardiac patients in collaboration with Oulu University Hospital. The electrode patches and the measurement units record three channels of ECG (EAS electrode system) and impedance pneumography. Finally, two types of temperature sensors were fabricated using digital printing methods. A high-precision electrohydrodynamic inkjet (E-jet) printer was used to fabricate a silver temperature sensor on the nanocellulose substrate, and an inkjet printer was used to fabricate graphene/PEDOT:PSS temperature sensors on the polyurethane substrate.

1.2   Structure of the thesis

This thesis consists of an introduction, four journal publications, and two conference articles. The Introduction is divided into five chapters and a conclusion. The first chapter provides a general introduction to the topic, presents the structure of the thesis, and explains the author's contribution to different publications. Chapter 2 describes the different printing methods and their pros and cons. Functional inks are discussed in Chapter 3, and different substrate materials are presented in Chapter 4. Chapter 5 introduces conformable electronics and demonstrates three conformable electronics applications fabricated using additive manufacturing methods. The final chapter summarizes the results, and the publications are appended to the end of the thesis.

1.3   The author's contribution

Publication I. The author shared the main contribution with M. Zakrzewski. The author participated in designing the samples and fabricated the samples. The author conducted the measurement together with M. Zakrzewski. The author also handled the data and participated in the writing process. Other writers participated in the designing of the experiments, writing, and improving the manuscript.

   Publication II. The author was the main contributor and designed the manufacturing process for the electrode patches and fabricated the samples. T. Kankkunen assisted in the design and fabrication processes. The author was the main responsible for writing the manuscript. A. Vehkaoja, V. Jeyhani, P.S. Preejith, J. Joseph, and Sivaprakasam M. fabricated the measurement unit and wrote about

the electronics module. A. Onubeze, A. K. Puuronen, S. Nurmentaus made the system-level description and wrote the mobile app and cloud paragraph. The author, A. Vehkaoja, and V. Jeyhani conducted the experiments, and A. Vehkaoja and V. Jeyhani analyzed the results and wrote about the electronics module. K. Noponen wrote the EAS lead system chapter. Other writers revised and improved the manuscript.

Publication III. The author was the main contributor and designed the manufacturing process for the electrode patches. The author fabricated the samples with T. Onnia. The author participated in the writing of the ethical review and recruited the volunteers for the tests. The author designed and conducted the test protocol with the volunteers and organized the collaboration with bioanalysts E. Laakso and S. Leppänen. They assisted in the setting of the electrode patches in plaace. The author was the main responsible for writing the publication, and K. Noponen analyzed the results. Other writers revised and improved the manuscript.

Publication IV. The author shared the main contribution and wrote the manuscript with K. Noponen. The author fabricated the measurement patches in collaboration with Screentec Oy. The author designed and conducted measurements with V. Jeyhani in collaboration with Oulu University Hospital. J. Junttila, M. Tulppo, K. Kaikkonen, and H. Huikuri provided medical expertise. V. Jeyhani designed and fabricated the data collecting device, and K. Noponen analyzed the results. They also wrote about these topics in the manuscript. Other writers revised and improved the manuscript.

Publication V. The author was the main contributor and designed and measured the test structures. R. Mangayil prepared the nanocellulose substrates and wrote a chapter about them. The author fabricated the test structures together with M-. M. Laurila, and M-. M. Laurila wrote the E-jet printing chapter. The author analyzed the results and was the main responsible for writing the conference article. Other writers revised and improved the manuscript.

Publication VI. The author was the main contributor and designed, fabricated, and measured the test structures. The author also analyzed the results and wrote the manuscript. T. Kankkunen designed and assembled the temperature logging setup. Other writers revised and improved the manuscript.

2 PRINTED ELECTRONICS FABRICATION PROCESSES

In printed electronics, different printing technologies are used to fabricate various electrical devices on a wide range of substrates. Used printing methods are, for example, screen printing, flexography, gravure, offset, and inkjet printing [10][11][12][13][14]. Printing means that electrically functional inks are deposited on a substrate to create active or passive devices, such as conductors, resistors, coils, transistors, and diodes [15][16][17][18][19]. The electrically functional inks can be conductive, semi-conducive, and dielectric.

Each printing method requires specific properties from the ink and provides patterns with different line widths and thicknesses. Hence, to achieve the desired pattern, the most suitable printing method and ink combination has to be chosen. Table 1 presents various printing methods and selected features. Line widths and thicknesses are values that correspond to routinely achievable values. [20]

Table 1. Different printing methods and selected features. Adapted from [20].

Printing method	Ink viscosity (mN m^{-1})	Line width (µm)	Line thickness (µm)	Printing speed m min^{-1}
Inkjet	1-100	30-50	0.1-1	1-500
E-jet	1-10^4	1	0.001-0.1	<1
Screen	500-10^5	30-50	5-100	50-150
Gravure	100-10^3	10-50	0.1-1	1000
Flexo	50-500	45-100	<1	500
Offset	100-10^5	10	1-10	1000

Printing methods can be divided into two categories; digital printing methods and traditional printing methods. In digital printing the printing is done according to a

digital-based image, whereas traditional printing requires physical masks, plates, and screens. In Table 1, inkjet and E-jet printing are digital printing methods, and the rest are traditional fabrication methods. Both printing methods, digital and traditional, have their benefits and challenges. Figure 2 presents three different material deposition methods. Figure 2 a) is an airbrush, b) is TIC SCF-300 semiautomatic screen printer, and c) is Dimatix DMP-2850 Material Printer. All these devices are used to deposit material on a specific area on a substrate. In an inkjet printer, a digital picture file defines the printed pattern, and with the screen printer and with the airbrush, a separate screen or masks are used for patterning.
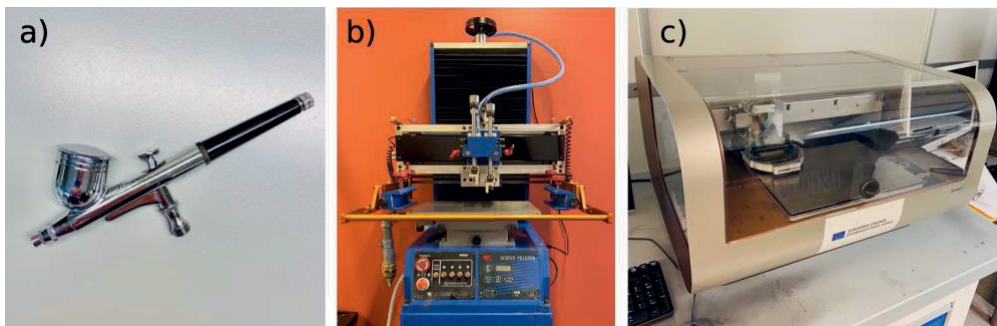
Figure 2. a) An airbrush, b) TIC SCF-300 semiautomatic screen-printing machine, and c) Dimatix DMP-2850 Material Printer.

2.1 Spray coating

The spray coating technique has advantages when it comes to a coating of large areas. There are no limits for the substrate size, it is roll-to-roll compatible, and it does not require a specific atmosphere (such as a vacuum). For these reasons, the spray coating is studied in the fabrication of transparent graphene films [21], solar cells [22][23][24], carbon membranes for air separation [25], and electrodes [26].

Spray-coating can be done, for example, with an airbrush (Figure 2 a)). A so-called nozzle pin is used to prevent the ink from leaving the reservoir before the release trigger is pulled. After pulling the release trigger, a stream of gas transfers the ink from the reservoir into the moving gas. The fast-moving gas breaks down the liquid into small droplets. Finally, the gas stream carries out the droplets through the nozzle of the spray-coater onto a substrate. The ink and gas can form the droplets

either inside the nozzle or outside the nozzle. The inner and outer air mixing is shown in Figure 3. [27]

Internal mixing   External mixing
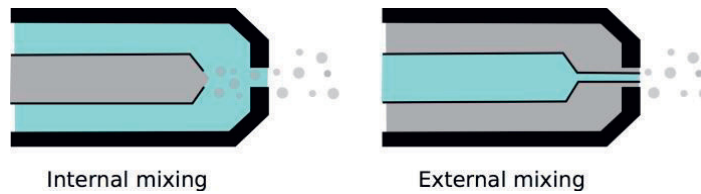
Figure 3. Inner and external mixing in an airbrush nozzle.

The material deposition with an airbrush can be controlled, for example, by changing the ink properties (viscosity, surface tension, and solid content), the nozzle-to-substrate distance, gas pressure, and ambient and substrate temperature. Since the ink spreads over a wide area, separate shadow masks are needed for pattern formation. Also, the spray coating creates more waste material compared to some other material deposition methods since all the material outside the pattern defined by the stencil will be waste material. Nevertheless, the spray coating is still widely used among industrial-scale coating methods since it can produce uniform coatings even for complex-shaped objects. [27]. Spray coating was used as a manufacturing method in Publication I.

2.2   Screen printing

Nowadays, a graphic screen printing is used to fabricate patterns on t-shirts and posters, and in electronics, it is used to mark the locations of components. In addition to graphical printing the screen printing can be used in printed electronics to create for example light-emitting diodes (LED) [28], solar cells [29], sensors [30][31][32] and antennas [33]. Figure 4 shows the basic principle of screen-printing in which a mesh and a squeegee is used to transfer ink onto a substrate. The screen printer has a screen that is stretched over a rigid frame, and a stencil is used to define the printed pattern on the screen. The pattern is formed in a way that the stencil blocks the non-image areas, and the image areas contain openings. The ink is then spread on the screen so that it covers the whole stencil area. Next, a squeegee wipes across the screen and simultaneously forces the ink through the stencil openings onto substrate. [34][35]
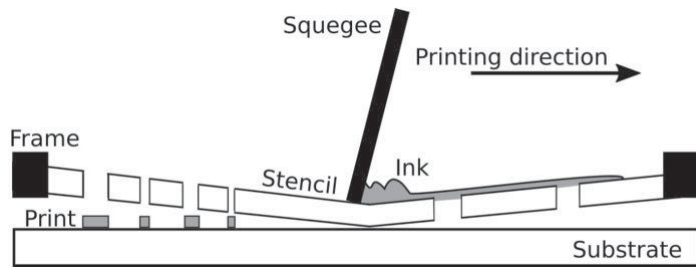
Figure 4. Screen printing process. Adapted from [35]

The quality of the final pattern is a result of many parameters. The printing mesh, stencil, frame, ink properties, snap-off distance, and squeegee all affect the result. In addition, the ink might limit the screen and squeegee material options. Many materials such as cotton, silk, nylon, polyester, or metal can be used to make the mesh, but the most commonly used is polyester. Polyester has replaced silk as a mesh material since it is not affected by cleaning chemicals, expands less during the printing process, and is more uniform in shape. In addition to the mesh material, the mesh count influences the print quality. The higher the mesh count (threads per cm), the better the print quality. Also, the thickness of the mesh and the stencil affect the thickness of the printed pattern. [35][36] The mesh is stretched over the frame, which is supposed to provide constant mesh tension during printing. The frame is most often made out of aluminum since the aluminum frame is rigid, stable, and durable. Other possible frame materials are, for example, steel and wood. [35]

2.3 Inkjet printing

The basic idea in inkjet printing is that small droplets of functional material are deposited on a substrate in predefined locations to form a specific pattern. Inkjet printing is a digital fabrication method, meaning that the final pattern is designed using a computer program. This pattern-design method gives the advantage that patterns can be modified in a short time frame compared to traditional printing methods. [37] Currently, essential methods for inkjet printing are continuous inkjet (CIJ) or drop-on-demand (DOD). In CIJ, the droplet flow is continuous, and in DOD, the droplets are ejected one by one. Specific droplets are selected from the continuous flow to form the print in CIJ, and in the DOD technique, the droplets

are produced only when needed. An electrospray technique is used in addition to CIJ and DOD techniques. In this technique, a jet of liquid is drawn from the print head using an electric field. [38]

In a simplified inkjet process, the printhead is ejecting droplets onto a substrate, and these droplets finally form the pattern. However, to be able to manufacture precisely correct functional structures, the technology requires synchronization of several different parameters. These parameters are, for example, ink rheology, substrate properties, and printing conditions (humidity, room temperature). The droplet formation is most often done either with thermal expansion or with a piezoelectric actuator in DOD printheads. In thermal printheads, a resistive heater rapidly heats the ink adjacent to the heater. Next, a thin layer of ink vaporizes, and the vapor bubble expands and forces a droplet out from the nozzle.

Hansell of the Radio Corporation of America invented the first DOD piezo inkjet device, and it was patented in 1950 [39]. After this pioneering patent, the basis of piezoelectric printers is an outcome of three patents [40]; Zoltan proposed a squeeze mode in 1972 [41], Stemme of Chalmers University in 1973 utilized the bending mode of piezoelectric operation, and Kyser and Sears of the Silonics company also patented a bend mode in 1976, but with a different shaped piezo element [42]. Figure 5 a) presents a present-day cartridge-style piezoelectric printhead, and b) shows a theoretical inner structure of the piezoelectric printhead.
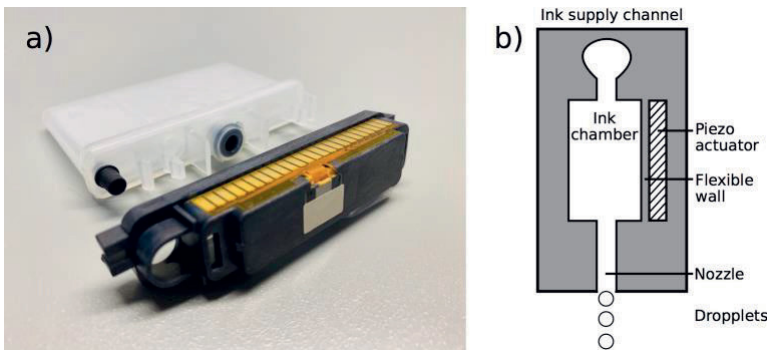
Figure 5. a) A piezoelectric printhead and b) an example structure of a nozzle.

The piezoelectric printhead can work in different modes due to the different possible configurations. The basic principle of operation relies on piezoelectric material's (piezo actuator) ability to change its shape when a voltage is applied on it. The

mechanical deformation of the ink chamber generates a pressure that forces the droplet out from the nozzle. Different printhead technologies may utilize different angles between the polling direction of the piezo element and the applied voltage. [40]

Droplet formation can also utilize electrostatic force instead of ink pressurization. A desk-top electrohydrodynamic inkjet (E-jet) printer manufactured by Super Inkjet Technology uses an electric field to make droplets [43]. This technology enables the printing of droplets that are sub-femtoliter in size and can make patterns with less than 1 μm line width. Figure 6 a) shows the SIJ printer and b) the basic operating principle of the printing. The droplet size is controlled by adjusting the field intensity between the meniscus and the grounded X-Y table. This adjustment can be made, for example, by changing the DC-, or peak voltage, and nozzle-to-substrate distance. Both the droplet ejection frequency and the printing speed affect the conductor width, whereas the number of printed layers controls the pattern thickness. (Publication V)
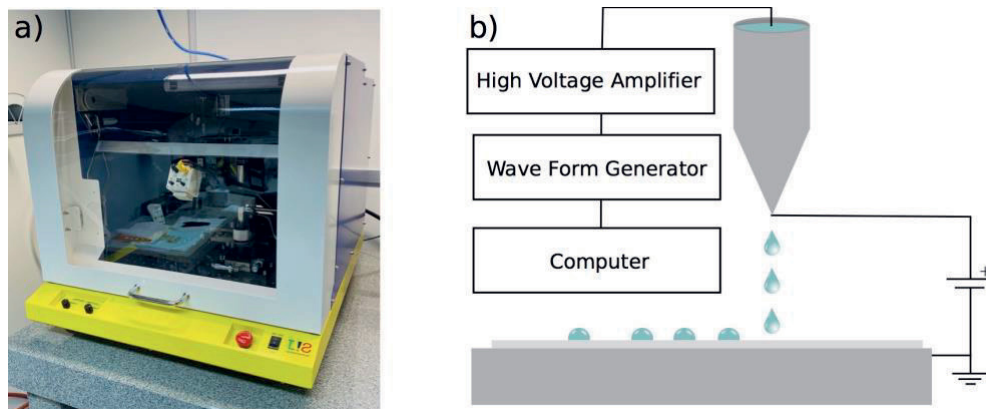
Figure 6. a) SIJ printer and b) the operating principle for patterning

Super inkjet technology has been used, for example, in the fabrication of metallization of high-density through-silicon vias (TSVs) [44], fabricate multilayer high-density redistribution layers (RDLs) of silicon interposers [45], single layer high-density circuitry for a microelectromechanical system (MEMS) device [46], and to increase the I/O density of 3D TSV interposers [47].

3   CONDUCTIVE INKS

The primary function of the conductive inks is to deliver the functional material from the printer to the substrate. The ink properties have to be well compatible with the requirements of the printer so that high-quality printed patterns can be achieved. Viscosity, or fluids resistance to change in shape, is one of the most significant properties of an ink. Table 1 shows viscosity values for different printing methods. It can be seen that inkjet printing inks are low viscosity inks, and in contrast, screen and offset printing requires high viscosity inks. However, the viscosity might not be constant during printing, and these types of different behaviors are shown in Figure 7. The fluid is said to be a Newtonian fluid if the shear stress of the fluid is directly proportional to the shear velocity. In other words, the viscosity of the fluid is independent of the strain rate. [48]
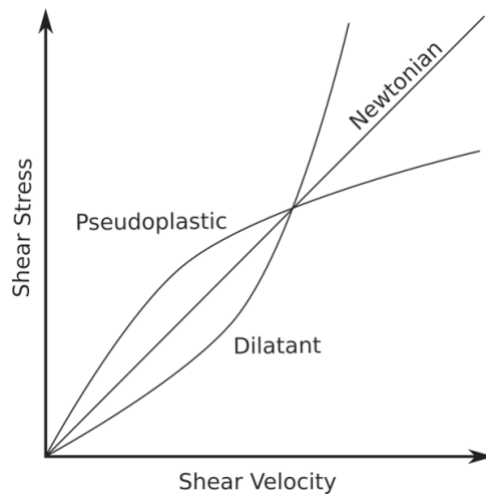
Figure 7. The behavior of Newtonian and non-Newtonian (dilatant and pseudoplastic) fluids [49].

In addition to Newtonian fluids, the ink can behave as a non-Newtonian liquid. In non-Newtonian fluids, the viscosity changes if the velocity gradient changes. The fluid is called dilatant (shear-thickening) if the viscosity increases when the shear velocity increases, and if the viscosity decreases when the liquid is moving faster, the liquid is called pseudoplastic (shear thinning). [48] For example, in inkjet printing, the organic solvents behave like Newtonian fluids and thus ensures the uniform droplet formation [38]. While in turn, screen printing inks are shear-thinning materials. The shear-thinning behavior ensures that the ink travels through the screen without difficulty when the squeegee presses the ink towards the screen [50].

3.1   Conductive materials

To ensure the proper integration with the skin, conformable electronics need to withstand the dynamic behavior and uneven surface of the skin, and this creates demands for the conductive patterns. One option is to design the conductive patterns to form 3D structures, which will then improve the mechanical properties of the patterns. In a stretching-patterning-release process, the substrate stretched before the patterning and released afterward. This type of process will create stretchable "wavy" patterns [51]. Several studies are done with the in-line horseshoe-like structures [52][53][54][55]. Honeycomb mesh structure was used by Takahashi et al. to make stretchable structures. [56]

In addition to creating stretchability with different 2D and 3D structures, the functional material can be inherently stretchable. Stretchable, functional materials may be single- or multi-component composites containing functional polymers, nanostructural carbon, and metal components [57][58][59]. The basic building blocks of functional inks are the functional material itself and the liquid medium in which the functional material is dispersed in. Metal nanoparticles, nanowires and nanoflakes, carbon nanotubes, graphene, and conductive polymers are examples of conductive functional materials used to fabricate conformable electronics. [60] Table 2 presents the conductive materials used in functional inks and their selected properties.

Table 2. Conductive materials in functional inks for conformable electronics. [61][62][51][63][64][65][66][67][68]

Conductive material	Resistance (Ω/sq)	Particle/molecule size
silver nanoparticles	0.7-8	2-10 nm
silver nanowires	13-50	1-20 µm
silver flakes	0.04 - 0.13	2-20 µm
PEDOT	1200	10-50 nm
PANI	5000	65 nm
graphene	>100	0.3-1 µm
CNT	>100	5-20 nm (diameter)

The conductive material and solvent are rarely enough to make properly functional inks. Post-processing parameters, adhesion to substrate, long shelf life, and appropriate surface tension and viscosity can be tuned with the right additives. Additives are components that are added in small amounts to modify the ink properties. Surfactants, such as siloxanes and fluorosurfactants, are used to stabilize the dispersion of particles in the ink and to reduce the surface tension. Humectants prevent the ink from drying too early and thus clogging, for example, in the inkjet nozzles. Dispersants are used to maintain stable dispersion of particles since the smaller particle size furthers the agglomeration. Steric stabilization is the most common way to stabilize highly loaded conductive inks. After finding the right additives and the ink is stable and jettable and forms uniform patterns, it also has to fasten to the substrate. The adhesion of the printed pattern can be improved with adhesion promoters such as acrylates, alkoxysilanes, and mercaptans. [69][37]

3.2   Ink on Substrate

In low viscosity inks, such as an inkjet or spray coating inks, the pattern formation is affected by the shape of the liquid droplet when the droplet finally reaches the substrate. In a pure liquid droplet, all the molecules pull each other equally in every direction, resulting in a zero-net force. An exception is the molecules at the surface that do not have neighboring molecules in all directions. These molecules are pulled

inward to maintain the balanced net force. This phenomenon creates an internal pressure that forces the droplet to maintain the lowest surface free energy and thus the smallest surface area. [70][71]

Three interfacial tensions define the mechanical equilibrium, and thus the contact angle of the liquid drop, on an ideal solid surface. These tensions are liquid-gas (γ_{LG}), solid-gas (γ_{SG}), and solid-liquid (γ_{SL}) interfacial tension. Figure 8 illustrates the three tensions and the contact angle θ. In the case of a good wetting, the contact angle is small (less than 90°), and the droplet spreads over a large area on the substrate. In contrast, the surface is unfavorable for wetting if the contact angle is more than 90°. [72][70][71]
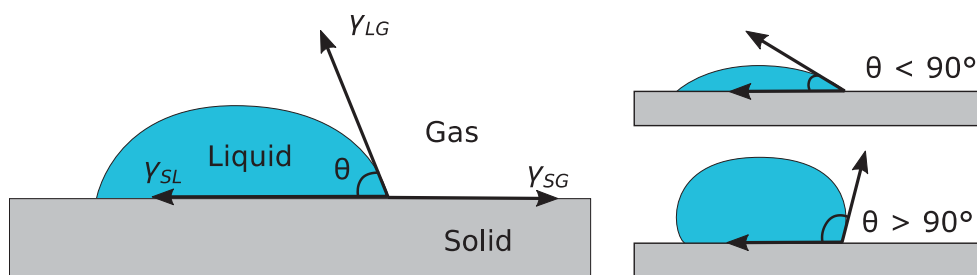
Figure 8. Contact angles formed by liquid on a smooth solid surface. [72]

$$\gamma_{LG} \cos \theta = \gamma_{SG} - \gamma_{SL} \qquad (1)$$

Equation 1 is Young's equation, and it relates to the surface tension between the phases: solid, liquid, and gas. Those, as mentioned earlier, apply only in ideal situations, and both real substrates and inks are never completely smooth and homogeneous. Besides, the droplet also has a high velocity when it lands on the substrate. The kinetic energy of the droplet is then converted into deformation energy and surface energy. The energy transfer creates an oscillatory motion of the contact line of the droplet. The motion is finally suppressed by the viscosity of the droplet and the adhesion between the droplet and the substrate. [73][74] The contact angle and thus, the spreading of the droplet, is often controlled with different physical and chemical treatments. Oxygen plasma treatment [75], silanization [76], ultraviolet (UV) radiation [77], ultraviolet/ozone (UVO) treatment [77] are some examples of the surface treatments that can be used for substrates.

The young equation shows how one droplet behaves on a substrate. However, the final pattern consists of multiple droplets printed closely one by one. The time difference between two droplets landing on a substrate and the distance between them is defining the line morphology. This morphology is demonstrated in [75], and Soltman and Subramanian showed five principal printed line behaviors. Figure 9 shows the delay as a function of drop spacing (left side) and shows examples of different line types (right side) when delay or drop spacing or both changes. These different line behaviors are individual drops, scalloped, uniform, bulging, and stacked coins. For example, if the drop spacing is too small, the printed pattern starts to flow over (bulging), and in turn, if the delay is too large, the individual drops are forming a line of drops (stacked coin).
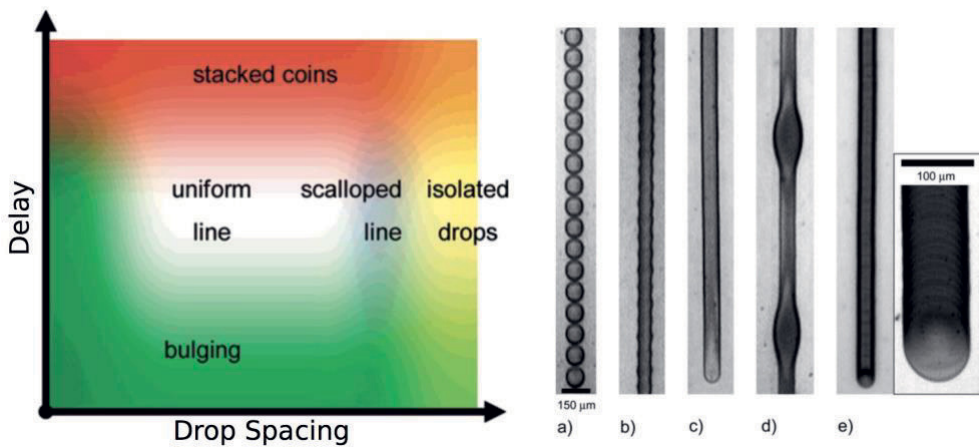
Figure 9. Delay in a function of drop spacing indicates how the printed line will form (left side). The different line variations are: a) individual drops, b) scalloped, c) uniform, d) bulging, e) stacked coins (right side). Adapted with permission from [78]. Copyright (2008) American Chemical Society

Wetting relates to another important factor in print quality, and that is an adhesin. When the ink pattern is on a substrate, an adhesion describes how well the ink is attached to the substrate. In other words, the adhesion tells how much work is needed to separate two interfaces from each other. Many mechanisms can explain the adhesion between the surfaces. Mechanical effects, such as surface roughness, affect the adhesion. Increasing the surface roughness increases the contact area between two interfaces and enables mechanical anchoring and thus results in better adhesion. [27][79]

In addition to wetting and mechanical interlocking chemical interactions affect the adhesion. The strongest chemical interaction is created by covalent bonding. Other chemical bonds are, for example, hydrogen bonds between H-donating and H-accepting groups. Two materials can also be joined by weak forces, such as Van-der-Waals forces. In these cases, the adhesion is a result of uneven distribution of charges due to the Heisenberg uncertainty principle. This transient charge in a particle may attract the nearby particles. [79][80]

In diffusive adhesion, materials merge into each other. In these cases, material components are being mobile, and at least one of the materials should be soluble in the other. This adhesion mechanism is common with polymers since the different polymer chains can intertwine. [81] The diffusive adhesion is also an active mechanism in sintering [82].

3.3 Post-processing

The printed ink pattern needs to be post-processed to bring the nanoparticles nearby and thus to ensure good electrical conductivity. The wet ink on a substrate is illustrated in Figure 10 a). nanoparticles have the polymer coating, and the solvent surrounds them. In thermal sintering, the printed pattern is heated so that the solvent evaporates, and the polymer coating starts to break (Figure 10 b)). Sintering temperatures are typically between 100–400 °C. [82]

After the removal of the polymer coating, the conductive nanoparticles are brought into contact with each other, which enables the metal-metal contact between the nanoparticles (Figure 10 c)). Metal-metal contacts or neck structures start to form between the nanoparticles (Figure 10 c)), and the surface energy reduction drives this during nanoparticle coalescence. The improved conductivity is a result of the percolation channels connecting adjacent nanoparticles rather than nanoparticles fusing to bulk metal. [82]
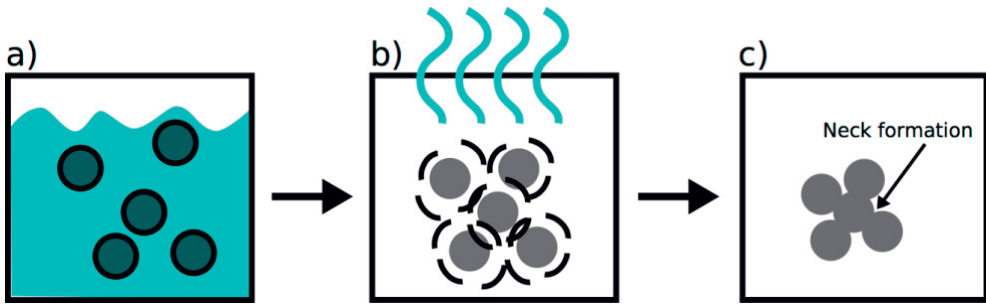
Figure 10. Inkjet-printed nanoparticles in different sintering phases.

Particle size, sintering temperature, and sintering time affect the sintering process. Many common substrate materials, such as PET or PUR, have glass transition temperatures considerably lower than 200 °C. Because of this, alternative sintering processes, such as plasma, microwave, and photonic sintering have been studied for local sintering. [82]

4 SUBSTRATES

The main function of the substrate is to provide both mechanical support and electrical connections for electronic components [83]. Rigid substrates provide adequate mechanical support, but at the same time, the integration to complex surfaces is not seamless. Flexible substrates are one step towards more conformable electronics. The requirements for the appropriate substrate are, for example, low thermal expansion, low cost, lightweight, and suitable surface properties. [84] Conductive structures on a rigid, flexible, and stretchable substrate are shown in Figure 11.
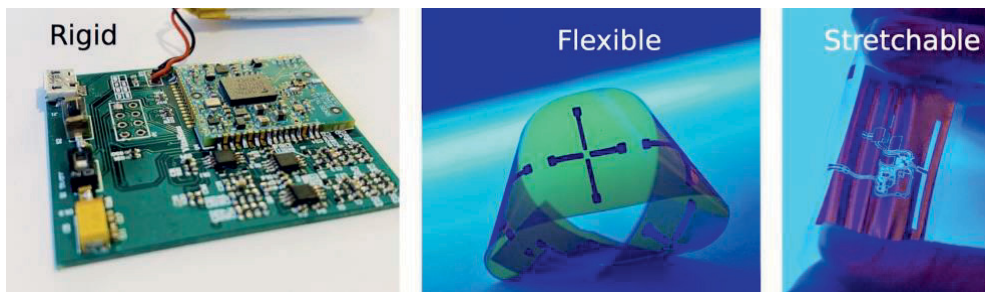
Figure 11. Conductive structures on rigid, flexible, and stretchable substrates.

Much used flexible substrate materials are, for example, polyimide (PI), poly(ethylene terephthalate) (PET), and poly(1,1-difluoroethylene) (PVDF). However, to be able to seamlessly integrate electronics, for example, to the human body, the flexible substrates are not conformable enough. In this case, the substrates need to be stretchable. Different silicones, such as poly(dimethylsiloxane) (PDMS) and polyurethane (PUR) are used as a substrate material in stretchable electronics. Table 3 lists different substrate materials and their selected properties. [84]

Table 3. Substrate materials and their selected properties. [84][85][86][87][88][89][90][91]

Material	Thickness (µm)	T_g (°C)	T_m (°C)	Modulus (GPa)	CTE (°C^{-1})	Surface energy (mN m^{-1})
PVDF	25–500	-40	175	1-3	70–180 x 10^{-6}	25
PET	1–350	80	260	4	20 x 10^{-6}	35–50
PI	7.5–125	410	406	2.7	20 x 10^{-6}	40
PUR	25–1000	-	155–185*	0.0036	-	38
nanocellulose paper	20–200	-	-	140	8 x 10^{-6}	50–60
PDMS	20–1000	-125	-40	0.001	325 x 10^{-6}	10–20

*softening range for thermoplastic polyurethane

Polymer materials are widespread substrate materials, but especially in disposable electronics also other types of substrates are studied. Alternative materials can be, for example, nanocellulose or paper-based substrates since they are disposable due to the biodegradability. [84] Other biodegradable substrate materials are, for example, silk [92][93] and aliphatic biodegradable polymers such as poly(vinyl alcohol) PVA [94] and polylactide (PLA) [95]. Water-soluble PVA substrates have recently been studied to fabricate conformable electronics. PVA can be used, for example, in nanomesh form in which the mesh structure improves the gas permeability and minimizes unwanted skin reactions [96].

4.1 Polymer substrates

PVDF is a thermoplastic fluoropolymer, which is generally synthesized from 1,1-difluoroethylene. The molecular weight, molecular weight distribution, the chain configurations, the crystalline form, and the defects of chaining are defining the physical and electrical properties of the PVDF. Due to the high dielectric dipole moment of the monomer, the PVDF acts as a crystal but is not inherently piezoelectric. Piezoelectricity means that material can produce an electrical charge in response to applied mechanical stress. Melt crystallized PVDF is oriented and subjected to a high electric field at elevated temperature to produce a large

polarization within the PVDF crystal. PVDF has a melting temperature in the range of 155–192 °C, however, the material will lose its polarization if it is heated up to its Curie temperature (T_c) of 80 °C. PVDF is not soluble in water, various solvents, oils, or acids. The advantage of PVDF, like other polymer films, is that it can be produced as thin, flexible, and lightweight films that can be cut into any shape and be integrated into various shaped surfaces. The PVDF has been used to fabricate different sensors [97] [98] [99] and energy harvesting applications [100][101]. [102]

Poly(ethylene terephthalate) (PET) is produced in a polymerization reaction of ethylene glycol and terephthalic acid under the influence of chemical catalysts. The repeating unit in the polymer chain contains a sizeable aromatic ring that gives stiffness and strength for the material. This happens especially when the chains are aligned with one another by drawing (stretching). PET film has low moisture absorption, high optical clarity, and good chemical resistance. Due to these favorable properties, PET film is the most widely used plastic film, and it is commonly used as a packaging and dielectric material, and as a substrate material in printed electronics. [85]

Polyimide (PI) films are high-performance, thermoplastic amorphous polymers originally developed by the DuPont™ Company. The material has several useful properties, and PI films are especially suitable for high-temperature applications due to the very high thermal stability. The thermal stability comes from the imide group that is formed by a condensation reaction of an aromatic anhydride group with an aromatic amine. PI also has good dielectric properties, chemical resistance, and mechanical strength. [85][103]

Elastomers are rubber-like polymers with low elastic modulus and high yield strain. The material can recover the initial shape even after large elastic deformations, and this makes elastomers suitable options for stretchable electronics. Silicones and polyurethanes are examples of materials commonly used in microtechnology. [86] Polyurethanes are a class of polymers formed by reacting a polyol with a diisocyanate or polymeric isocyanate. Multiple different segment arrangements can be involved, but the only necessary condition is the presence of the urethane group (-NHC-O-) on the macromolecular chain more or less frequently. The properties of the polyurethane originate from the types of isocyanates and polyols used to make the polymer. Polyurethanes can either be thermoset – does not melt when heated – or thermoplastic. They have excellent mechanical and elastic properties, high abrasion and chemical resistance, and long lifetime expectancy. By changing the formulation, the polyurethanes can be manufactured with properties ranging from soft elastomers

to relatively hard reinforced rubbers. Polyurethane is a common material in conformable electronics [104][8][105][106][Publication III][Publication VI]. [107]

The most common elastomer in microfabrication is poly(dimethylsiloxane) (PDMS). PDMS has an inorganic backbone of alternating oxygen and silicon atoms with two methyl groups in each silicon atom. PDMS has a low elastic modulus that can be tuned by altering the cross-link density or by changing the film thickness. PDMS is a hyperelastic, isotropic material that does not obey Hook's law in its stress-strain behavior, and this needs to be considered when simulating the mechanical properties of the material. Very hydrophobic PDMS often needs surface treatments, for example, plasma, UV, and corona treatments, to increase the low surface energy and decrease the large contact angles. The contact angle between water and PDMS on an untreated substrate is $116 \pm 1°$. PDMS has a large coefficient of thermal expansion (CTE) value compared to metals and other plastics, and this can cause compatibility issues with other materials deposited on the PDMS. This CTE mismatch restricts the process temperatures when fabricating on PDMS. [86]

4.2   Nanocellulose substrate

Nanocellulose is a nature-based material in which the cellulose fibrils are in the nanometer widths. Nanocelluloses such as cellulose nanocrystals, microfibrillated cellulose, and bacterial nanocellulose has attracted attention over the last decades. These kinds of cellulose-based materials are biodegradable, lightweight, and widely available. They also have excellent chemical and electrochemical stability, excellent mechanical strength, and large surface area. Bacteria synthesize bacterial nanocellulose, unlike plant-based cellulose nanocrystals and microfibrillated cellulose. This production method of nanocellulose does not include chemical treatments or mechanical shearing and thus reduces the environmental impact by making the production process sustainable. Bacterial nanocellulose is highly pure, being free from other plant components (pectin, lignin, and hemicellulose impurities) compared to plant-based cellulose. The material exhibits some unique physical characteristics such as a high level of crystallinity (60–90 %), a high degree of polymerization, and high water content. In addition to good biocompatibility, the bacterial nanocellulose exhibits good tissue integration and mechanical properties similar to soft tissues. Bacterial nanocellulose membranes are an effective substrate for tissue engineering [108] and for wounds dressing [109]. [110] [111]

5   CONFORMABLE ELECTRONICS

Internet-of-Things (IoT) is a vision of the future in which the Internet and the Web extent into the physical realm. In other words, this means that all kinds of devices, from coffee makers to complex medical devices, would be connected to the Internet. IoT would utilize spatially distributed devices with embedded identification, sensing, and actuation capabilities. In this way, it is possible to collect information, communicate, compute, and produce action. Electronics need to be embedded in physical objects to make them smart. [112] Rigid printed circuit boards have been around for several decades [1], but with new materials and manufacturing methods, the development is going towards more conformable electronics. This type of electronics would enable the seamless integration of electronics to both the physical objects and even to the people themselves.

In addition to devices, also people could be connected to IoT. Low levels of electrical current drive most of the physiological phenomena of the human body, and the human body is radiating heat. For example, nerve functions, heart beating, brain activity, and body temperature can be measured from the skin. Continuous monitoring of these quantities is a life-saving process for several patient groups. Two examples are given in Figure 12 a) and b).
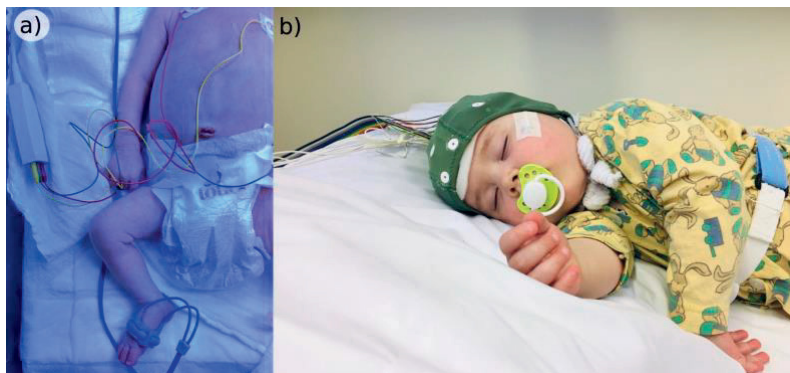
Figure 12. a) Wire-connected ECG and b) EEG monitoring events.

In Figure 12 a), a premature baby is connected to an ECG monitoring system that also measures the oxygen saturation levels. An electroencephalography (EEG) recording is performed in Figure 12 b). In both of these situations, the movements of the patient are restricted, and this is causing discomfort.

Stationary, wire-connected, or portable monitoring systems are shrinking in size and weight, and the monitoring systems are brought closer to the user. This transition has already been seen with wearable monitoring systems. This new type of mobile monitoring with wireless systems will limit everyday activities as little as possible and thus improve the patients' quality of life. So-called epidermal electronic systems (EES) are the state-of-the-art systems in unobtrusive vital sign monitoring. The mechanical properties of the EESs are aimed to match the mechanical properties of the human epidermis, and the structures have to be very thin to enable seamless integration with the skin [113]. The fine structure of the EESs predisposes it to wrinkling and self-adhesion. Besides, the adhesion may wear out when the system is peeled off from the skin. Because of these reasons, the EESs would highly benefit if they were fabricated as low-cost, disposable measurement systems [9]. Figure 13 presents an inkjet-printed push-button, which is attached to a fingertip to illustrate possible EESs.

Figure 13. Conformable inkjet-printed push-button [114].

5.1   Fabrication methods in different applications

Different applications benefit from combinations of different printing methods, inks, and substrates. The fabrication method and the materials should be decided based on the final application. For example, if the device will be attached to the skin or to another surface, they benefit from a different approach. Table 4 shows three different applications, their printing methods, inks, and substrates. These applications are presented with more details in the following chapters.

Table 4. Printing method, ink, and substrate combinations for different conformable electronics systems.

Application	Printing method	Ink	Substrate
Touch panel	spray coating	graphene/PEDOT:PSS	PVDF
ECG sensor	screen printing	Ag/AgCl silver flake	polyurethane
Temperature sensor	inkjet printing	graphene/PEDOT:PSS	polyurethane
	E-jet printing	silver nanoparticle	nanocellulose

A touch panel is a large-area application compared to, for example, local skin sensors. In addition, this application does not require high-resolution patterning, so spray coating with a shadow mask was chosen as a manufacturing method. Spray coating enables the covering of large surface areas, and the shadow mask defines the coarse button shapes required to determine user actions. The thickness of the sprayed material layer can be controlled by controlling the sprayed material volume, and with this method, you can define your layer thickness linearly and not layer-by-layer, such as in screen printing. This application was designed to be used only on a flat or curved surface, and hence flexible PVDF substrate provides both adequate mechanical properties and electrical functions. Graphene/PEDOT:PSS ink was chosen for its transparent nature.

ECG sensor is placed on the human body, and for that reason, flexibility is not enough, but more conformable substrates are needed. When electronics are placed on human skin, the mechanical properties of the substrate should mimic the mechanical properties of the skin as much as possible. But at the same time, the substrate should work as a supportive base for the measurement unit. Soft thermoplastic polyurethane provides mechanical support for the measurement system and worked as a conformable substrate for stretchable silver conductors and silver-silver chloride electrodes. The mechanical properties of the PUR also ensure the safety aspects of the ECG patch, so that in clinical trials, the patient can be sent home with the device. Silver and Ag/AgCl were chosen as conductor and electrode materials since silver provides high conductivity and Ag/AgCl works as a reliable ECG electrode material. In addition, the used inks were stretchable, so they improved the user comfort together with the stretchable PUR substrate. ECG patches were screen printed since the printed pattern was relatively large, and screen

printing enables thick print layers and thus lower resistance values even with uneven substrates like PUR.

Human skin has a high sensor density, and to reach this, high-resolution printing methods, such as inkjet and E-jet printing, are needed. For that reason, inkjet printing was chosen as a fabrication method for the graphene/PEDOT:PSS temperature sensors. Due to its digital nature, inkjet printing enables fast pattern geometry variation and optimization compared to, for example, to gravure or flexographic printing. This is useful since the geometry of the printed pattern affects its stretching properties. Graphene/conductive polymer solution was chosen as a sensor material due to its good sensor properties based on literature surveys and its inherently more conformable mechanical nature compared to, for example, metals. Substrate material was a skin-conformable PUR with an adhesive layer to fix the sensor in place. E-jet printing was chosen for the silver temperature sensor since the super inkjet can achieve even higher resolution. The substrate material was bacterial nanocellulose, since it is very pure material due to the fabrication process and thus good to be used in skin applications. In addition, nanocellulose would be a more environmentally sustainable option compared to the polymer substrates. In the following chapters, these different applications are defined in more details.

5.2 Touch panel

All kinds of smart systems are nowadays controlled with a touch screen. For example, mobile phones, tablet computers, and interactive info terminals at shopping centers are controlled with a touch of a finger. To enable the widespread integration of the touch screens envisioned in IoT, the development is going towards conformable touch screens. Indium tin oxide (ITO) is the most common option for transparent electrodes in the touch screens. However, using ITO has several drawbacks, and that is why there is a need to replace the material in touch screens. Another perspective is the manufacturing processes. A roll-to-roll manufacturing and new solution processable materials would enable the manufacturing of low-cost, large-area touchscreens. [115][116]

In Publication I, solution-processable, nanostructural carbon materials were used in the fabrication of flexible touch panels onto a PVDF substrate. CNT/xylan nanocomposite ink and two different graphene-based inks were used to fabricate PVDF touch panels. Electron-beam evaporated copper electrodes were fabricated as a reference. The spray-deposition of the graphene/PEDOT:PSS ink was done on

a 60 °C hot-plate to ensure even layer formation. Without the hotplate, the ink tends to form large individual drops on the substrate. The ink was then dried in an oven at 65 °C for 8 minutes per side. The sheet resistance of the touch panel was 76 ± 8 Ω sq^{-1}

The setup shown in Figure 14 was used to measure the response of the touch panels. The setup consisted of a computer connected charge amplifier and an analog-to-digital converter (ADC). The temperature of the touch panel was simultaneously recorded. A custom-made stylus ("Artificial finger" in Figure 14) was utilized in the water immersion test to exclude the pyroelectric phenomenon generated by the heat convection from the human finger during pressing. The stylus had a cylinder-shaped metallic weight with a rubber tip to mimic a real fingertip.
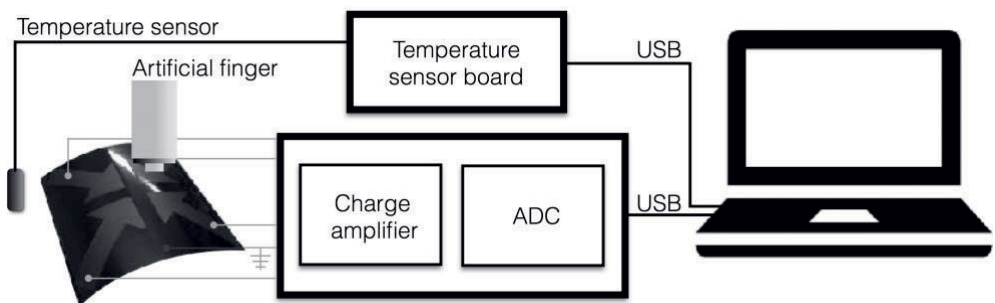
Figure 14. Touch panel measurement setup. (from Publication I)

Figure 15 illustrates a) the sample and b) the response signals recorded in dry ambient air. Figure 15 shows that there is no cross-talk effect between two adjacent keys. However, considerable cross-talk was observed, due to the movements of the PVDF film, if the samples were not firmly attached to a rigid surface.
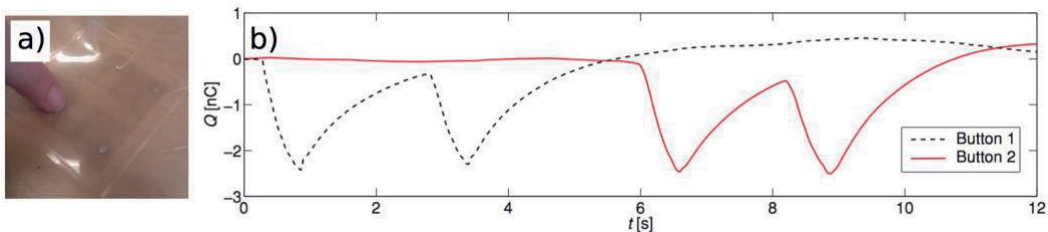
Figure 15. a) The sample and b) the received response signal in dry ambient air. (from Publication I)

5.3   ECG sensor bandage

Cardiovascular diseases (CVDs) are the most common cause of death globally. The number of CVD related deaths is fast-growing, for example, on account of growth and aging of the population, unfavorable transformations in living habits. Premature deaths can be prevented by the identification of high-risk groups and by ensuring proper treatment and monitoring both out-of-hospital and in-hospital situations. [117][118] Bulky electrodes, wires, connectors, and stationary or portable separate central units are common in traditional ECG monitoring systems. The development is transitioning towards more unobtrusive patch-type and epidermal electronics monitoring systems to improve user comfort and, thus, the quality of life [119][53][2]. Different mobile ECG monitoring devices and their selected properties are shown in Table 5. The patch type of devices have also led to more extended study periods and higher study completion rate due to the user-friendly design. [120]

Table 5. Different mobile ECG monitoring devices and their selected properties. [121]

Description	Device type	Number of leads (channels)	Status	Examples
12 leads	chest strap	12	commercial	SmartHeartpro
reconstructed 12 leads	portable	12+ (4 electrodes)	commercial	Cardiosecur Pro
less than 12 leads	chest strap	1	commercial	Quardiocore
	portable	3	commercial	Bittium Faros 360™, MCT 3 Lead
	patch	1	commercial	ZIO®XT Patch, NUVANT™, CAM™
	patch	2 (derived 3rd)	commercial	Peerbridge
	epidermal electronics		prototype	

Publication II presents the first version of the printed, skin-mounted hybrid system for ECG measurements. The measurement system consists of a printed electrode patch and a measurement electronics module. The measurement data from the electronics module is transmitted wirelessly to a mobile device using Bluetooth Low Energy. The data can then be visualized in the mobile device and sent further to the cloud if needed.

The ECG measurement system utilizes EAS electrode configuration that is a subset of an extensively studied EASI lead configuration system introduced by Dower et al. [122] In EASI electrode configuration, the electrode E is at the lower part of the sternum, the electrode A locates on the standard V5 electrode location

of the 12-lead system, and the electrode S locates on the manubrium. The measurement unit uses the single-ended configuration and measures the potentials of E-, A-, and S-electrode with respect to a common reference. The common electrode locates between the S- and the E-electrodes. The bipolar leads A-E, A-S, and E-S are formed as potential differences between the A-, E-, and S-electrodes.

Figure 16 a) shows the printed electrode patch and the monitoring unit worn on a volunteer and b) the material layers. Layer 1 is a 50-µm-thick Platilon 4201 AU thermoplastic polyurethane film (Covestro, Germany). Layer 2 is the same polymer material with stretchable conductors and electrodes. The conductive pattern is screen-printed with TIC SCF-300 screen printer and using CI-4040 stretchable Ag/AgCl ink (ECM, USA). The silver ink contains 40–50 wt% silver powder and 5–15 wt% silver chloride powder diluted in a diethylene glycol ethyl ether acetate solvent. The printed pattern is cured at 130°C for 30 minutes in a convection oven. Layer 3 is a polyurethane film with an acrylic adhesive layer. Cutout holes are made
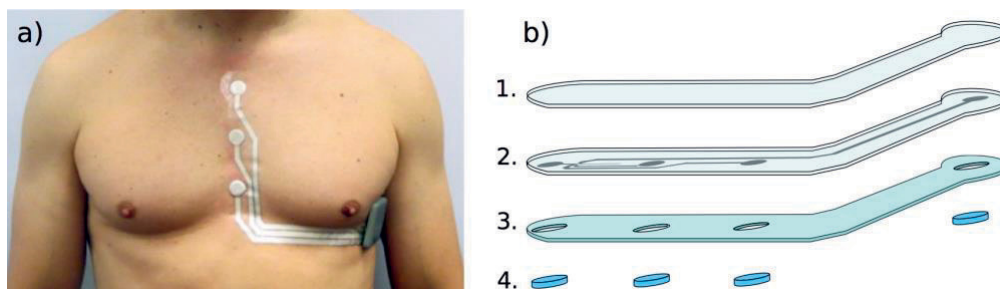
Figure 16. a) A volunteer wearing the printed electrode patch and the monitoring unit. (from Publication II) © [2016] IEEE and b) the material layers in the ECG patch.

to layer 3, and then the layers 1–3 are heat-laminated together. Copper tape provided electrical contact from the print to the surface of the patch, and anisotropic conductive adhesive was used to secure the measurement unit in place bot mechanically and electrically. The measurement unit can be seen in Figure 16 a) near the armpit. Finally, round-shaped pieces of AG635 sensing gel (Axelgaard Manufacturing Co., Ltd., USA) were used at the electrode-skin interface to ensure stable electrical contact.

The performance of the developed ECG monitoring system and printed electrodes was demonstrated with a series of activities. Within these activities, a male volunteer was lying still for 2 minutes, sitting for 2 minutes, and walking for 2 minutes, and an ECG signal was recorded simultaneously. Figure 17 presents five-second extracts of the recorded ECG signals from each of the activities. The

uppermost signal (red) is the A-E lead signal, the one in the middle (blue) is the A-S lead signal, and the lowest one (yellow) is the E-S lead signal. Figure 17 shows a good signal-to-noise ratio even without pre-processing, and ECG morphology is clearly visible and sufficient for ECG analysis.
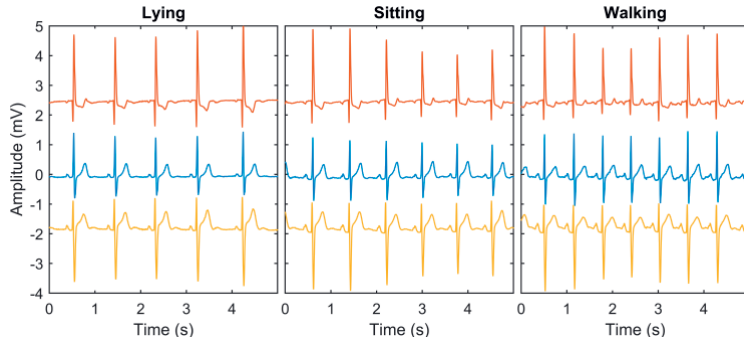
Figure 17. ECG signal from different activities; lying still, walking, and sitting. Red: A-E lead signal, blue: A-S lead signal and yellow: E-S lead signal. (from Publication II) © [2016] IEEE

Movement artifacts in the ECG signal are a challenge in long-term recordings. Because of this, in Publication III, a printed multi-lead ECG electrode patch was compared with Ambu Blue Sensor R-00-S electrodes during different physical activities to estimate differences in their vulnerability to motion artifacts. Figure 18 A) shows a volunteer wearing the Ambu Blue electrodes and the data collecting device, and B) shows a volunteer with the printed bandage and the data collecting device. The fabrication process of the patch is overall similar to the fabrication process shown in Publication II, but the connector type was changed to micro-USB.
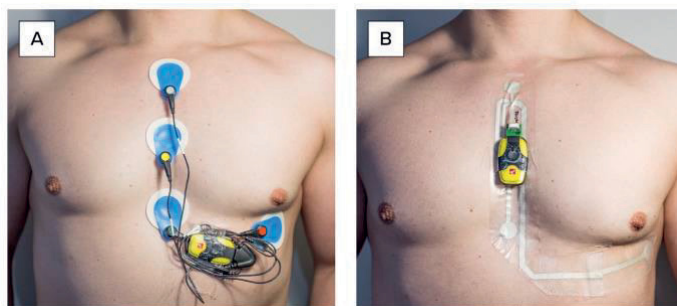
Figure 18. A) volunteer wearing the Ambu-Blue sensor electrodes with the data collecting device. B) a volunteer wearing the printed bandage with the data collecting device. (from Publication III)

Volunteers, with different body types, did two identical, approximately 30 min long test rounds. The volunteers were resting for 1 hour between the test rounds. Physical activities were lying still in a supine position, standing, walking on a treadmill (3km/h), walking on a treadmill (6km/h), running on a treadmill (10 km/h), and sitting. Each activity was 5 minutes long, except for the running, which was 2 minutes long. Both test rounds were done by wearing either printed ECG electrodes or traditional electrodes, and the order was randomized. Faros 360 (Bittium Biosignals, Finland) recording device was used to record the signals in both cases. Volunteers were both males and females, with an age range from 23 to 50, and they had a different level of physical performance and no diagnosed cardiac-related diseases.

Figure 19 presents the result from one randomly selected volunteer. Figure 19 shows the beat-to-beat variation in the A-S lead both with the printed electrode bandage (left) and with the commercial electrodes (right) in five different activities. The beat-to-beat variability patterns are very similar in both cases. However, some natural beat-to-beat variations can also be seen, and this may be caused, for example, by respiration, movements, and noise.
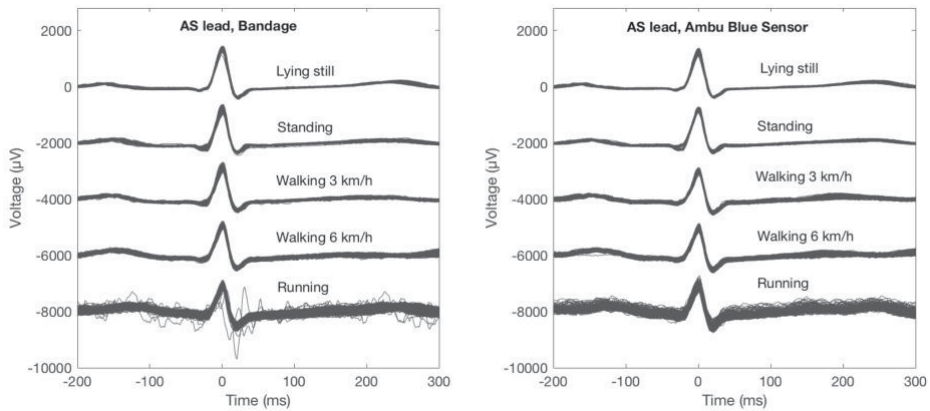
Figure 19. Superimposed beats recorded from the A-S lead with the bandage (left) and commercial electrodes (right) during the physical activities. Activity levels are biased by −2 mV from top to bottom to enable a simultaneous inspection. (from Publication III)

Figure 20 shows the median discrepancies of each volunteer, and it can be noted that with some volunteer in some physical activities, the median beat-to-beat deviations differ between the patch and the commercial electrodes. This phenomenon can be seen as a displacement from the diagonal line.
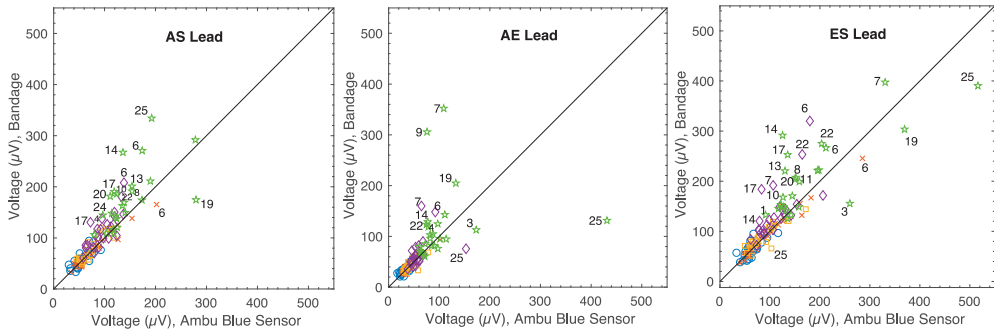
Figure 20. Scatter plot comparison of median RMS (µV) beat-to-beat variabilities of the QRS waves in electrodes and bandages in the A-S, the A-E, and the E-S lead. Activities as marked as follows: lying still; blue circle, standing; red cross, walking 3 km/h; yellow square, brisk walking 6 km/h; purple diamond, and running 10 km/h; green star. Median RMS deviations of over 35 µV are marked with the volunteer number. (from publication III)

The overall signal quality is similar between the printed electrode bandage and the commercial electrodes. The similarity is seen both in average behavior as in beat-to-beat variation intraindividually thought the physical activities. We have validated the signal quality during different activities with printed multi-lead ECG electrode bandage and showed that signal quality, which is comparable to electrodes currently used in healthcare, could be achieved with printed, unobtrusive electrode patches.

Printed electrode bandages were utilized in an unobtrusive, low-cost, out-of-hospital, and in-hospital measurement and monitoring system in Publication IV. The proposed system consists of four main parts, and the parts are shown in Figure 21. Part 1) is the printed patch with a measurement unit, 2) is the gateway unit (for example, a laptop or a tablet compute), 3) are the cloud-based analysis tools, and 4) are the front-end tools for data viewing and decision making.
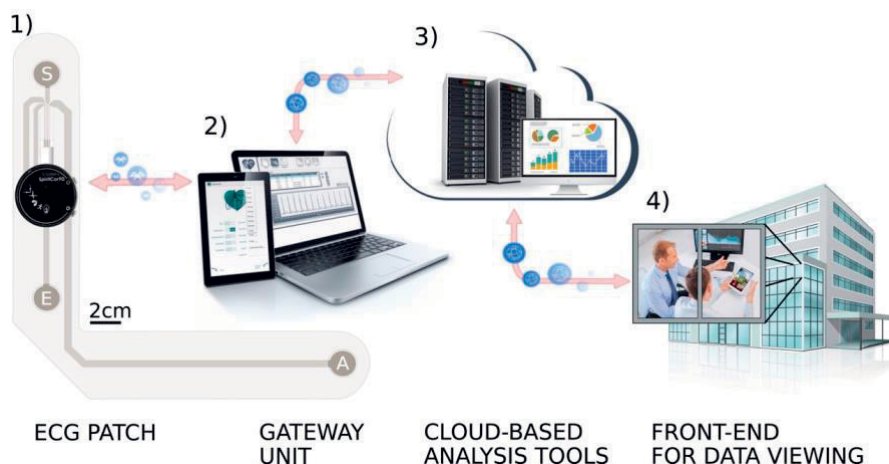
Figure 21. The four parts of the measurement and monitoring system: 1) the measurement unit and the printed electrode, 2) the gateway unit, 3) the cloud-based data analysis and storing tools, and 4) front-end application for viewing the analysis results. (from Publication IV)

The electrode patch and the measurement unit are used to record three channels of ECG (EAS electrode system) and impedance pneumography. The system was tested with cardiac patients in collaboration with Oulu University Hospital to verify the performance in real-life situations. The recording was started at the hospital, and the participants went home for the next 24 hours. The recording stopped automatically after 24 hours, and the volunteers returned the devices to the hospital the next day.

The manufacturing process and the material choices were designed in collaboration with Screentec Ltd., and Screentec produced the patches by our design and instructions. Circular electrode areas were screen printed using CI-4040 stretchable Ag/AgCl ink (ECM, USA), and the circuitry is screen-printed with Cl-1036 (ECM, USA) stretchable silver ink. The Ag/AgCl ink contains 40–50 wt% silver powder and 5–15 wt% silver chloride powder diluted in a diethylene glycol ethyl ether acetate solvent. Cl-1036 silver ink has silver flake content of 50–60 % and 1–5 wt% of polymer material diluted in the same solvent. The pattern is fabricated on a 125-μm-thick T 391 stretchable TPU (Policrom Screens, Italy). Hydrogel circles ware used at the electrode locations to ensure good electrical with the skin. To make sure that the patch stays firmly in place, silicone adhesive is applied on top of the print.

The data was collected from eight volunteers – both males and females – with an age range of 50–59. The analysis was done after the volunteers returned the measurement units. Figure 22 shows the results from one of the volunteers. The NN-intervals in the top figure of Figure 22 a) are measured with the Faros 360, and the NN-intervals in the bottom figure are measured with the developed measurement unit. In Figure 22 b), the corresponding Pointcaré plots of the NN beats are superimposed to illustrate the agreement between the consecutive intervals.
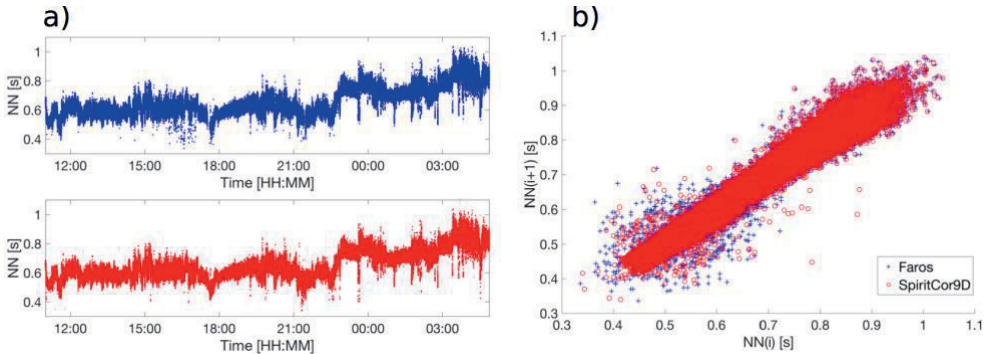
Figure 22. a) The upper subplot shows the NN-tachograms measured with Faros 360, and the bottom figure shows the NN-tachograms from the measurement unit. b) Corresponding results as an overlaid Poincaré plots from Faros 360 (blue cross) and the measurement unit (red circle). (from Publication IV)

The similarity of the signals shows that the developed measurement unit and the printed electrode patch together can provide good quality signal compared to the commercial options. This type of monitoring system can provide critical information on a person s health and even benefit in finding the right diagnosis. Also, the unobtrusive nature of these systems can improve the quality of life in different patient groups.

5.4 Temperature sensors

One of the crucial parameters in healthcare is the body temperature since fever (abnormal elevation in body temperature) is one of the oldest and most familiar sings of disease [123]. The body temperature can be measured from the skin, and because of this, a skin thermometer can be exploited in the examination of cardiovascular health, physical activity, and ulcer prediction and prevention [124][125][126][127].

Different materials have been studied to be used as an active material in temperature sensors. Table 6 presents temperature sensor materials and selected properties of the systems which have been used to fabricate skin temperature sensors.

Table 6. Different temperature sensor materials for skin temperature measurements. [128][129][130][131][9][132][133]

Sensor material	TCR (% °C^{-1})	Substrate	Fabrication method
PEDOT:PSS/CNT	0.61	PI	screen printing
PEDOT:PSS/CNT	0.85	PET	printed
PEDOT:PSS + DMSO	0.25	PEN	Inkjet printing
Polyaniline nanofibers	1.0	PET	transferring
Au/Cr	0.28	PUR	sputtering
Au film	0.17	PET	thermal evaporation (cut-and-paste)
Reduced graphene oxide	0.63	PET	air-spray coating
CNT (multi-wall)	0.068	PET	air-spray coating

Publication V presents a straightforward fabrication of E-jet printed silver temperature sensors on a skin-conformable bacterial nanocellulose substrate. Printing as a manufacturing method and nanocellulose as a substrate material are offering favorable properties since the thin, skin-like sensors systems tend to be disposable. Compared to the traditional processes using lithography, printing processes can enable the decreased number of fabrication steps, reduced material consumption, and the possibility to use new kinds of materials. Whereas using the bacterial nanocellulose instead of plastic substrates would bring down the negative environmental impact.

In Publication V silver conductors (for measurement contacts) were fabricated with CI-4040 stretchable Ag/AgCl ink (ECM, USA) and TIC SCF-300 screen printer with a polyester screen. The screen has a mesh count of 79 threads per cm, a mesh opening of 69 μm, and a stretching angle of 22.5°. The screen-printed conductors were annealed in a convection oven at 130 °C for 30 minutes. DGP 40TE-20C silver nanoparticle ink (Advanced Nano Products Ltd, Korea) was used to fabricate the meander shaped temperature sensor structures. The nanoparticle ink

has a solid content of 30–35 wt% diluted in triethylene glycol monoethyl solvent. Printing was done with a commercially available E-jet device, Super Inkjet (Super Inkjet Technology Inc., Japan), and the pattern was sintered at 150 °C for one hour after printing.

Figure 23 a) shows the cross-section of the temperature sensor. Layer 1 is the temperature sensor printed with the Super Inkjet printer using silver nanoparticle ink. The sensor is printed between the screen-printed silver conductors (2). Layer 3 is the nanocellulose substrate, and 4 is a PDMS that works as a release layer. PET film (5) was used to provide mechanical support during manufacturing and measurement phases. Peltier element (6) is used for the electrical characterization measurements. Figure 23 b) presents the temperature sensor worn on a finger and an optical microscope image of the sensor part. The temperature sensor has an approximately 20 µm line width with 50 µm spacing.
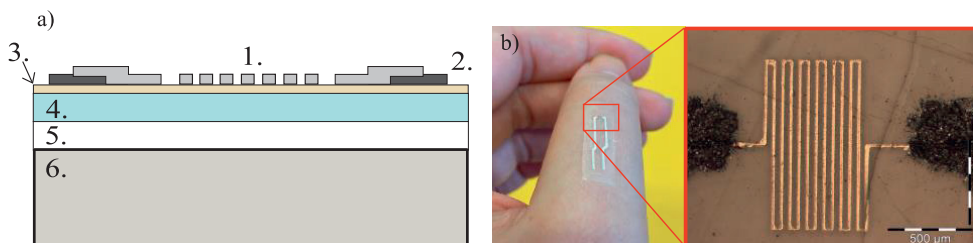
Figure 23. a) Material layers in the temperature sensor. b) The temperature sensor worn on a finger and an optical microscope image of the sensor. (from Publication V)

A resistance measurement setup with a heating and cooling unit was used to measure the resistance dependence on temperature in ambient conditions. The resistance measurement was done with a digital multimeter using VirtualBench (National Instruments, USA). The digital multimeter was controlled with LabVIEW, and the measurement was done with a sampling rate of 1 Hz. The heating and cooling unit consisted of a Peltier element and Silverstone Tundra TD03 liquid cooler. The Peltier element was also controlled with LabVIEW and VirtualBench, and the liquid cooler kept the non-measurement side of the Peltier element at constant room temperature. TC-08 Thermocouple Data Logger (Pico Technology, UK) recorded the temperature of the substrate surface.

The electrical characterization was done by cycling the temperature of the Peltier element. The voltage of the Peltier element was stepwise increased and decreased with the VirtualBench. Each step was 0.4 V, and the voltage was kept constant for 1 minute on every step. The temperature oscillated between 24 °C and 41 °C, and the complete cycles, in which the temperature raised from 24 °C to 41 °C and decreased back to 24 °C, were repeated five times for each sample. The normalized resistance and temperature in a function of time are shown in Figure 24 a) and b). Whereas five complete cycles are shown in Figure 24 c) in the form of normalized resistance as a function of temperature.
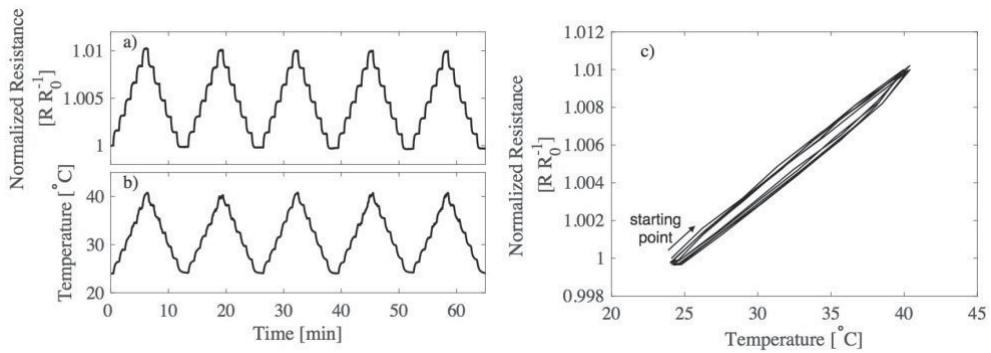
Figure 24. a) Normalized resistance and b) measured temperature in a function of time. c) Five complete cycles plotted as a normalized resistance in a function of temperature. (from Publication V)

Silver is a positive temperature coefficient material, and thus the resistance of the fabricated temperature sensor increased when the temperature was increasing, resulting in a TCR value of 0.0602 % per degree Celsius. Besides, the hysteresis stays low, as can be seen in Figure 24 c). Due to the relatively low TCR value, the fabricated temperature sensor is not competing in efficiency with the already existing temperature sensors, but it combines a high-resolution printing method with the environmentally endurable substrate material. These types of temperature sensors could be used as an indicator of fever or local infections by expressing if the local body temperature is going up or down.

Inkjet-printed graphene/PEDOT:PSS temperature sensors are presented in Publication VI. The sensors are inkjet-printed on stretchable TPU substrate. First, a set of silver conductors were fabricated to be used as contacts for the characterization setup. The silver conductors were printed with the TIC SCF-300 screen printer using stretchable silver ink (CI-1036). A polyester screen was used with the screen printer, and the screen had a 79 threads cm^{-1} mesh count, 69 µm mesh openings, and a 22.5° stretching angle. The silver conductors were cured in the convection oven at 130 °C for 30 minutes. The sensor structure was inkjet-printed with a Phene Plus I3015 transparent graphene/PEDOT:PSS ink. The ink has graphene content of 1–5 wt% and the same amount of PEDOT:PSS. The inkjet-printing was done with Dimatix Materials Printer DMP-2831 (Fujifilm, USA) using a 10 pl drop volume print head. Every sensor had three layers of graphene/PEDOT:PSS ink with 1270 dpi printing resolution. This resolution equates to 20 µm drop spacing. Both the printing plate temperature and the print head temperature were 40 °C. Finally, the graphene/PEDOT:PSS sensors were annealed in a convection oven at 130 °C for 10 minutes. A fluoropolymer coating was used to minimize the effect of the ambient atmosphere. Consequently, Novec 1700 Electronic Grade Coating (EGC) (3M, USA) was pipetted on top of the sensors in an argon atmosphere, and it was allowed to dry at room temperature.
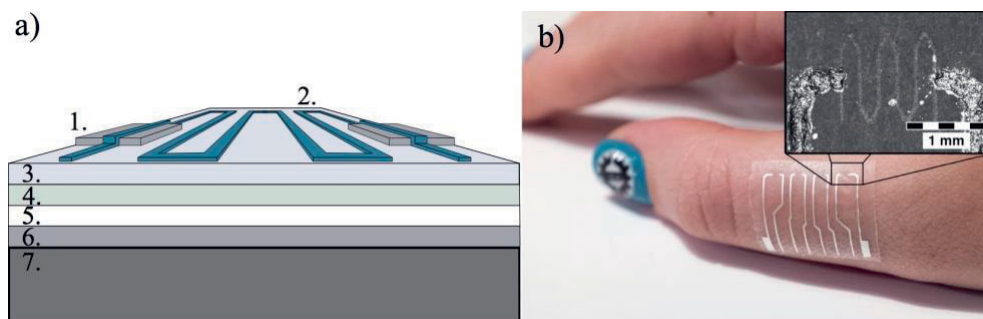
Figure 25. a) The multilayer structure of the Graphene-PEDOT:PSS temperature sensor and the measurement setup and b) an array of sensors attached to a finger. (from Publication VI)

Figure 25 a) shows the different layers in the sensor structure of the printed temperature sensors and the characterization setup. Layers 1 and 2 are the screen printed silver conductors and the inkjet-printed graphene/PEDOT:PSS sensor structure. These functional layers were printed on top of an adhesive bandage (plaster). The bandage had a TPU surface (3) with a polyacrylate adhesive layer (4) underneath it. Layer 5 was a protective paper for the adhesive layer, and layer 6 is a

PET sheet providing mechanical support to keep the sample stable while handling the sample and during measurements. Figure 25 b) shows an array of four temperature sensors being attached to a finger.

To characterize the temperature sensors, they were predisposed to temperature cycling. Each sample went through the temperature cycle five times, and the results are shown in Figure 26. The measurements were done in an inert argon atmosphere to minimize the impact of ambient atmosphere factors, such as oxygen or moisture. Figure 26 a) shows normalized resistance, and b) the corresponding temperature measurements from three different samples. Different samples are marked with different line styles and colors. Figure 26 shows how the resistance is decreasing when the temperature is increasing since the graphene/PEDOT:PSS behaves like negative temperature coefficient material. This negative temperature coefficiency has also been seen in other publications with PEDOT:PSS, graphene, and other nanostructural carbon/PEDOT:PSS. Figure 26 c) presents the normalized resistances as a function of temperatures during the first increase in temperature (from 34 °C to 44 °C). The red rectangle marks the phase of the measurement from which the data is collected for Figure 26 c). The temperature sensors exhibited TCR of 0.047% per degree Celsius.
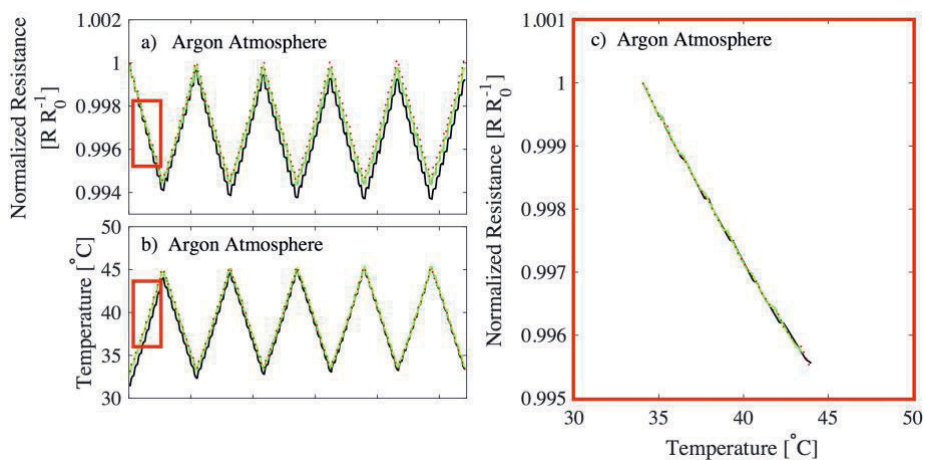
Figure 26. a) Overlaid normalized resistances and b) temperatures from three samples during five temperature cycles. One cycle starts from 34 °C and goes up to 44 °C and decreases back to 34 °C. c) Normalized resistance as a function of temperature formed from the values in a) and b) subplot marked with a red rectangle. (from Publication VI)

The samples were coated with a fluoropolymer to minimize the not temperature-related effects, such as humidity. The coating was done in an inert atmosphere, and the samples were then characterized both in an argon atmosphere and in an ambient atmosphere. Figure 27 a) shows the normalized resistance in a function of temperature in an argon atmosphere, and b) shows the results from a similar measurement done in the ambient atmosphere.
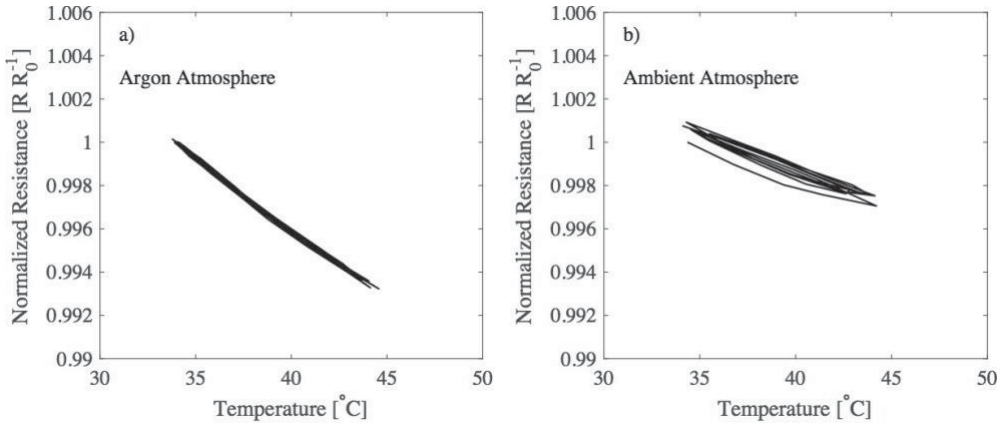
Figure 27. Normalized resistance in a function of temperature in a) an argon atmosphere and b) in an ambient atmosphere. (from Publication VI)

The temperature sensor receives a TRC value of 0.064% per degree Celsius in Figure 27 a), and in Figure 27, the TRC value is 0.034% per degree Celsius. The change in TRC values shows that the ambient clearly affects the behavior of the graphene/PEDOT:PSS composite and efficient barrier coatings are needed to rule out other impacting factors than temperature.

6   CONCLUSIONS

Nowadays, electronics can be found all around us. A remarkable number of everyday gadgets include electronics, and even people are wearing different electronics systems. For that reason, electronics are being integrated with all kinds of surfaces. The integration level could be taken further if the electronics would be more conformable. Nevertheless, the rigid nature of traditional printed circuit boards is not offering the best option for this type of electronics. For that reason, there is a need for new fabrication processes and material combinations to improve the level of integration.

The spray coating fabrication of transparent graphene/PEDOT:PSS touch panels was demonstrated in Publication I. With spray coating technology, it is possible to fabricate thin layers of graphene/PEDOT:PSS on PVDF substrate to fabricate transparent touch panels with 64.7% transparency. The touch panel could then be molded on round surfaces since the PVDF is only sensitive for pressure changes and not for static pressure.

ECG monitoring patches were fabricated using screen printing and stretchable silver ink with TPU substrate (Publications II, III, and IV). The motion artefact comparison study showed that the printed patches were able to provide similar signal quality than the commercial electrodes. The signal analysis verified the possibility to test the electrode patches together with a monitoring unit with cardiac patients. The 24h test period indicated that there is a good overall agreement with signals recorded with the printed electrode patch compared to the commercial electrodes even in unsupervised surroundings.

Both inkjet printing and E-jet printing were demonstrated in the fabrication of conformable temperature sensors (Publications V and VI). The received TCR values of 0.06% do not compete in efficiency, but the material combinations are providing totally new kinds of properties. Using bacterial nanocellulose as a substrate material can bring down the negative environmental impact compared to the plastic materials. Using sensor materials like graphene/PEDOT:PSS offers better, inherently conformable mechanical properties compared to, for example, metals.

In this thesis, it was shown that the printing method, combined with novel materials, enables the fabrication of different conformable sensors. The efficiency of the sensors does not yet compete with the commercial applications, but the new materials and fabrication processes enable the fabrication of completely new kinds of devices that can integrate seamlessly with uneven surfaces. The functionality of the applications was proven with different characterization methods and trials. These tests, with both healthy volunteers and cardiac patients, showed the performance compared to the commercial electrodes and in real-life situations. These results can be utilized when making material and fabrication decisions for conformable healthcare and body-monitoring application. Results also give insight how industrial cost-effective mass-manufacturing can be introduced in conformable electronics manufacturing.

In the future, the use of conformable electronics will be even more widespread due to easier integration and improved user comfort. However, this development requires a lot of work to be done, for example, in different trials, to test the usability of the systems in real-life situations. Another big research theme will be to find suitable biodegradable materials, since especially body-monitoring systems benefit from disposability, and for that reason, it is important to find environmentally sustainable options. A lot of research is done in the field of conformable electronics, but several research questions remain for future work to be solved.

REFERENCES

[1]   D. Charles, "Electrical apparatus and method of manufacturing the same." Google Patents, 01-Dec-1925.

[2]   Y. Liu, M. Pharr, and G. A. Salvatore, "Lab-on-Skin: A Review of Flexible and Stretchable Electronics for Wearable Health Monitoring," *ACS Nano*, vol. 11, no. 10, pp. 9614–9635, Oct. 2017.

[3]   J. A. Rogers, T. Someya, and Y. Huang, "Materials and Mechanics for Stretchable Electronics," *Science (80-.).*, vol. 327, no. 5973, pp. 1603 LP – 1607, Mar. 2010.

[4]   M. G. Mohammed and R. Kramer, "All-Printed Flexible and Stretchable Electronics," *Adv. Mater.*, vol. 29, no. 19, p. 1604965, May 2017.

[5]   A. Hanif *et al.*, "A Skin-Inspired Substrate with Spaghetti-Like Multi-Nanofiber Network of Stiff and Elastic Components for Stretchable Electronics," *Adv. Funct. Mater.*, vol. 30, no. 38, p. 2003540, Sep. 2020.

[6]   Z. Cui *et al.*, *Printed Electronics : Materials, Technologies and Applications*. Hoboken, SINGAPORE: John Wiley & Sons, Incorporated, 2016.

[7]   J. Wade, *Printed electronics*. IOP Publishing, 2018.

[8]   M. Mosallaei *et al.*, "Geometry Analysis in Screen-Printed Stretchable Interconnects," *IEEE Trans. Components, Packag. Manuf. Technol.*, vol. 8, no. 8, pp. 1344–1352, 2018.

[9]   S. Yang *et al.*, "'Cut-and-Paste' Manufacture of Multiparametric Epidermal Sensor Systems," *Adv. Mater.*, vol. 27, no. 41, pp. 6423–6430, Nov. 2015.

[10]   N. Karim, S. Afroj, S. Tan, K. S. Novoselov, and S. G. Yeates, "All Inkjet-Printed Graphene-Silver Composite Ink on Textiles for Highly Conductive Wearable Electronics Applications," *Sci. Rep.*, vol. 9, no. 1, p. 8035, 2019.

[11]   P. Zeng *et al.*, "Screen-Printed, Low-Cost, and Patterned Flexible Heater Based on Ag Fractal Dendrites for Human Wearable Application," *Adv. Mater. Technol.*, vol. 4, no. 3, p. 1800453, Mar. 2019.

[12]   B. B. Maskey *et al.*, "A smart food label utilizing roll-to-roll gravure printed NFC antenna and thermistor to replace existing 'use-by' date system," *IEEE Sens. J.*, p. 1, 2019.

[13]   M. L. Morgan, D. J. Curtis, and D. Deganello, "Control of morphological and electrical properties of flexographic printed electronics through tailored ink rheology," *Org. Electron.*, vol. 73, pp. 212–218, Oct. 2019.

[14]   J. Zhang, J. Tang, W. Sun, Y. Zhang, X. Wang, and B. Yang, "Quality Mapping of Offset Lithographic Printed Antenna Substrates and Electrodes by Millimeter-Wave Imaging," *Electronics*, vol. 8, p. 674, Jun. 2019.

[15]   Y. Wei, Y. Li, R. Torah, and J. Tudor, "Laser curing of screen and inkjet printed conductors on flexible substrates," in *2015 Symposium on Design, Test, Integration and Packaging of MEMS/MOEMS (DTIP)*, 2015, pp. 1–4.

[16]   J. Hlina, J. Reboun, J. Johan, M. Simonovsky, and A. Hamacek, "Reliability of printed power resistor with thick-film copper terminals," *Microelectron. Eng.*, vol. 216, p. 111095, Aug. 2019.

[17]   B. S. Cook *et al.*, "Inkjet-printed, vertically-integrated, high-performance inductors and transformers on flexible LCP substrate," in *2014 IEEE MTT-S International Microwave Symposium (IMS2014)*, 2014, pp. 1–4.

[18]   Y. Jo, H. Park, H. Ahn, Y. H. Kim, and S. Jung, "Influence of bank geometry on the electrical characteristics of printed organic field-effect transistors," *Flex. Print. Electron.*, vol. 4, no. 4, p. 42001, 2019.

[19]   S.-I. Park *et al.*, "Printed Assemblies of Inorganic Light-Emitting Diodes for Deformable and Semitransparent Displays," *Science (80-.).*, vol. 325, no. 5943, pp. 977 LP – 981, Aug. 2009.

[20]   K. Fukuda and T. Someya, "Recent Progress in the Development of Printed Thin-Film Transistors and Circuits with High-Resolution Printing Technology," *Adv. Mater.*, vol. 29, no. 25, p. 1602736, Jul. 2017.

[21]   V. H. Pham *et al.*, "Fast and simple fabrication of a large transparent chemically-converted graphene film by spray-coating," *Carbon N. Y.*, vol. 48, no. 7, pp. 1945–1951, Jun. 2010.

[22]   L.-M. Chen *et al.*, "Multi-Source/Component Spray Coating for Polymer Solar Cells," *ACS Nano*, vol. 4, no. 8, pp. 4744–4752, Aug. 2010.

[23]   G. Susanna, L. Salamandra, T. M. Brown, A. Di Carlo, F. Brunetti, and A. Reale, "Airbrush spray-coating of polymer bulk-heterojunction solar cells," *Sol. Energy Mater. Sol. Cells*, vol. 95, no. 7, pp. 1775–1778, Jul. 2011.

[24]   J.-W. Kang *et al.*, "Fully spray-coated inverted organic solar cells," *Sol. Energy Mater. Sol. Cells*, vol. 103, pp. 76–79, Aug. 2012.

[25]   M. Acharya and H. C. Foley, "Spray-coating of nanoporous carbon membranes for air separation," *J. Memb. Sci.*, vol. 161, no. 1–2, pp. 1–5, Aug. 1999.

[26]   D. Y. Choi, H. W. Kang, H. J. Sung, and S. S. Kim, "Annealing-free, flexible silver nanowire–polymer composite electrodes via a continuous two-step spray-coating method," *Nanoscale*, vol. 5, no. 3, pp. 977–983, 2013.

[27]   A. Goldschmidt and H.-J. Streitberger, *Basics of Coating Technology*. Hannover: Vincentz Network, 2003.

[28]   D. A. Pardo, G. E. Jabbour, and N. Peyghambarian, "Application of Screen Printing in the Fabrication of Organic Light-Emitting Devices," *Adv. Mater.*, vol. 12, no. 17, pp. 1249–1252, Sep. 2000.

[29]   F. C. Krebs *et al.*, "A complete process for production of flexible large area polymer solar cells entirely using screen printing—First public demonstration," *Sol. Energy Mater. Sol. Cells*, vol. 93, no. 4, pp. 422–441, Apr. 2009.

[30]   K. C. Honeychurch and J. P. Hart, "Screen-printed electrochemical sensors for monitoring metal pollutants," *TrAC Trends Anal. Chem.*, vol. 22, no. 7, pp. 456–469, Jul. 2003.

[31]   M. Albareda-Sirvent, A. Merkoçi, and S. Alegret, "Configurations used in the design of screen-printed enzymatic biosensors. A review," *Sensors Actuators B Chem.*, vol. 69, no. 1–2, pp. 153–163, Sep. 2000.

[32]   R. Nagata, K. Yokoyama, S. A. Clark, and I. Karube, "A glucose sensor fabricated by the screen printing technique," *Biosens. Bioelectron.*, vol. 10, no. 3–4, pp. 261–267, Jan. 1995.

[33]   M. L. Scarpello, I. Kazani, C. Hertleer, H. Rogier, and D. Vande Ginste, "Stability and Efficiency of Screen-Printed Wearable and Washable Antennas," *IEEE Antennas Wirel. Propag. Lett.*, vol. 11, pp. 838–841, 2012.

[34]   H. Kipphan, *Handbook of print media: technologies and production methods*. Springer Science & Business Media, 2001.

[35]   J. Izdebska, S. Thomas, D. Novaković, N. Kašiković, G. Vladić, and M. Pál, "Screen Printing," *Print. Polym.*, pp. 247–261, Jan. 2016.

[36]   S. T. Ingram, *Screen printing primer*. Graphic Arts Technical Fndtn, 1998.

[37]   I. M. Hutchings and G. (Graham D. Martin, Eds., *Inkjet technology for digital fabrication*. Chichester, West Sussex, U.K: Wiley, 2013.

[38]   G. D. Martin and I. M. Hutchings, "Fundamentals of Inkjet Technology," *Inkjet Technology for Digital Fabrication*. pp. 21–44, 30-May-2014.

[39]   C. W. Hansell, "Jet Sprayer Actuated by Supersonic Waves," 2,512,743, 1950.

[40]   H. Wijshoff, "The dynamics of the piezo inkjet printhead operation," *Phys. Rep.*, vol. 491, no. 4, pp. 77–177, 2010.

[41]   S. I. Zoltan, "Pulsed droplet ejecting system." Google Patents, 1972.

[42]   E. L. Kyser and S. B. Sears, "Method and apparatus for recording with writing fluids and drop projection means therefor." Google Patents, 1976.

[43]   N. Shirakawa, K. Kajihara, Y. Kashiwagi, and K. Murata, "Fine-pitch copper wiring formed in a platingless process using ultra-fine inkjet and oxygen pump," in *2015 International Conference on Electronics Packaging and iMAPS All Asia Conference (ICEP-IAAC)*, 2015, pp. 373–376.

[44]   B. Khorramdel, M. M. Laurila, and M. Mäntysalo, "Metallization of high density TSVs using super inkjet technology," in *2015 IEEE 65th Electronic Components and Technology Conference (ECTC)*, 2015, pp. 41–45.

[45]   M. M. Laurila, B. Khorramdel, and M. Mäntysalo, "Combination of E-Jet and Inkjet Printing for Additive Fabrication of Multilayer High-Density RDL of Silicon Interposer," *IEEE Transactions on Electron Devices*, vol. 64, no. 3. pp. 1217–1224, 2017.

[46]   M. Laurila, A. Soltani, and M. Mäntysalo, "Inkjet printed single layer high-density circuitry for a MEMS device," in *2015 IEEE 65th Electronic Components and Technology Conference (ECTC)*, 2015, pp. 968–972.

[47]   B. Khorramdel *et al.*, "Inkjet printing technology for increasing the I/O density of 3D TSV interposers," *Microsystems Nanoeng.*, vol. 3, no. 1, p. 17002, 2017.

[48]   R. Rennie and J. Law, "Newtonian fluid." Oxford University Press, 2016.

[49]   R. P. Chhabra and J. F. Richardson, "Chapter 1 - Non-Newtonian Fluid Behaviour," R. P. Chhabra and J. F. B. T.-N.-N. F. and A. R. (Second E. Richardson, Eds. Oxford: Butterworth-Heinemann, 2008, pp. 1–55.

[50]   H.-W. Lin, C.-P. Chang, W.-H. Hwu, and M.-D. Ger, "The rheological behaviors of screen-printing pastes," *J. Mater. Process. Technol.*, vol. 197, no. 1, pp. 284–291, 2008.

[51]   S. Yao and Y. Zhu, "Nanomaterial-Enabled Stretchable Conductors: Strategies, Materials and Devices," *Adv. Mater.*, vol. 27, no. 9, pp. 1480–1511, Mar. 2015.

[52]   Y. Zhang *et al.*, "Experimental and Theoretical Studies of Serpentine Microstructures Bonded To Prestrained Elastomers for Stretchable Electronics," *Adv. Funct. Mater.*, vol. 24, no. 14, pp. 2028–2037, Apr. 2014.

[53]   W.-H. Yeo *et al.*, "Multifunctional Epidermal Electronics Printed Directly Onto the Skin," *Adv. Mater.*, vol. 25, no. 20, pp. 2773–2778, May 2013.

[54]   J. Kim *et al.*, "Epidermal Electronics with Advanced Capabilities in Near-Field Communication," *Small*, vol. 11, no. 8, pp. 906–912, Feb. 2015.

[55]   R. C. Webb *et al.*, "Ultrathin conformal devices for precise and continuous thermal characterization of human skin," *Nat Mater*, vol. 12, no. 10, pp. 938–944, Oct. 2013.

[56] T. Takahashi, K. Takei, A. G. Gillies, R. S. Fearing, and A. Javey, "Carbon Nanotube Active-Matrix Backplanes for Conformal Electronics and Sensors," *Nano Lett.*, vol. 11, no. 12, pp. 5408–5413, Dec. 2011.

[57] A. J. Bandodkar, R. Nuñez-Flores, W. Jia, and J. Wang, "All-Printed Stretchable Electrochemical Devices," *Adv. Mater.*, vol. 27, no. 19, pp. 3060–3065, May 2015.

[58] K.-Y. Chun *et al.*, "Highly conductive, printable and stretchable composite films of carbon nanotubes and silver.," *Nat. Nanotechnol.*, vol. 5, no. 12, pp. 853–857, Dec. 2010.

[59] C. F. Guo, T. Sun, Q. Liu, Z. Suo, and Z. Ren, "Highly stretchable and transparent nanomesh electrodes made by grain boundary lithography," *Nat. Commun.*, vol. 5, no. 1, p. 3121, 2014.

[60] W. Wu, "Stretchable electronics: functional materials, fabrication strategies and applications," *Sci. Technol. Adv. Mater.*, vol. 20, no. 1, pp. 187–224, Dec. 2019.

[61] E. Song and J.-W. Choi, "Inkjet Printing of Conducting Polymer Nanomaterials," *Nanomaterials for 2D and 3D Printing*. pp. 245–264, 10-Apr-2017.

[62] I. M. Hutchings and G. D. Martin, "Introduction to Inkjet Printing for Manufacturing," *Inkjet Technology for Digital Fabrication*. pp. 1–20, 30-May-2014.

[63] E. Hrehorova *et al.*, "Gravure Printing of Conductive Inks on Glass Substrates for Applications in Printed Electronics," *J. Disp. Technol.*, vol. 7, no. 6, pp. 318–324, Jun. 2011.

[64] J. S. Moon *et al.*, "Transparent conductive film based on carbon nanotubes and PEDOT composites," *Diam. Relat. Mater.*, vol. 14, no. 11, pp. 1882–1887, 2005.

[65] S. Merilampi, T. Laine-Ma, and P. Ruuskanen, "The characterization of electrically conductive silver ink patterns on flexible substrates," *Microelectron. Reliab.*, vol. 49, no. 7, pp. 782–790, 2009.

[66] F. Torrisi *et al.*, "Inkjet-Printed Graphene Electronics," *ACS Nano*, vol. 6, no. 4, pp. 2992–3006, Apr. 2012.

[67] S. Timpanaro, M. Kemerink, F. J. Touwslager, M. M. De Kok, and S. Schrader, "Morphology and conductivity of PEDOT/PSS films studied by scanning–tunneling microscopy," *Chem. Phys. Lett.*, vol. 394, no. 4, pp. 339–343, 2004.

[68] E. Song, R. P. Tortorich, T. H. da Costa, and J.-W. Choi, "Inkjet printing of conductive polymer nanowire network on flexible substrates and its application in chemical sensing," *Microelectron. Eng.*, vol. 145, pp. 143–148, 2015.

[69] S. Magdassi, *The chemistry of inkjet inks*. 2009.

[70] A. Frohn, *Dynamics of Droplets*. 2000.

[71] Y. Yuan and T. R. Lee, *Surface Science Techniques*. Berlin, Heidelberg: Springer Berlin Heidelberg, 2013.

[72] T. Young, "Contact angle," *Trans. R. Soc. L.*, vol. 95, p. 65, 1805.

[73] S. Chandra and C. T. Avedisian, "On the collision of a droplet with a solid surface," *Proc. R. Soc. London. Ser. A Math. Phys. Sci.*, vol. 432, no. 1884, pp. 13–41, Jan. 1991.

[74] M. Kuang and Y. Song, "Inkjet Printing of Photonic Crystals," *Nanomaterials for 2D and 3D Printing*. pp. 183–211, 10-Apr-2017.

[75] M. O. H. Cioffi, H. J. C. Voorwald, and R. P. Mota, "Surface energy increase of oxygen-plasma-treated PET," *Mater. Charact.*, vol. 50, no. 2–3, pp. 209–215, Mar. 2003.

[76] W. C. Bigelow, D. L. Pickett, and W. A. Zisman, "Oleophobic monolayers: I. Films adsorbed from solution in non-polar liquids," *J. Colloid Sci.*, vol. 1, no. 6, pp. 513–538, Dec. 1946.

[77] K. Efimenko, W. E. Wallace, and J. Genzer, "Surface modification of Sylgard-184 poly(dimethyl siloxane) networks by ultraviolet and ultraviolet/ozone treatment.," *J. Colloid Interface Sci.*, vol. 254, no. 2, pp. 306–315, Oct. 2002.

[78] D. Soltman and V. Subramanian, "Inkjet-Printed Line Morphologies and Temperature Control of the Coffee Ring Effect," *Langmuir*, vol. 24, no. 5, pp. 2224–2231, Mar. 2008.

[79] N. M. E. P. S. P. Jones Frank N., "6.1.1 Surface Mechanical Effects on Adhesion," *Organic Coatings - Science and Technology (4th Edition)*. John Wiley & Sons, 2017.

[80] S. Y. Buhmann, "Introduction: Dispersion Forces," in *Dispersion Forces I: Macroscopic Quantum Electrodynamics and Ground-State Casimir, Casimir--Polder and van der Waals Forces*, Berlin, Heidelberg: Springer Berlin Heidelberg, 2012, pp. 1–43.

[81] M. K. Chaudhury, A. V Pocius, and D. A. Dillard, *Adhesion Science and Engineering : Surfaces, Chemistry and Applications*. Amsterdam, NETHERLANDS, THE: Elsevier Science & Technology, 2002.

[82] I. Reinhold, "Inkjet Printing of Functional Materials and Post-Processing," *Nanomaterials for 2D and 3D Printing*. pp. 27–49, 10-Apr-2017.

[83] K. M. Gupta, A. Tiwari, and N. Gupta, *Advanced Electrical and Electronics Materials : Processes and Applications*. Somerset, UNITED STATES: John Wiley & Sons, Incorporated, 2015.

[84] K. Suganuma, "Substrate and Barrier Film BT - Introduction to Printed Electronics," K. Suganuma, Ed. New York, NY: Springer New York, 2014, pp. 87–94.

[85] P. Schmitz and S. Janocha, "46.2.2.2 Extrusion," *Ullmann's Polymers and Plastics - Products and Processes, 4 Volume Set*. John Wiley & Sons, 2016.

[86] S. P. Lacour, "Stretchable Thin-Film Electronics," *Stretchable Electronics*. pp. 81–109, 28-Dec-2012.

[87] K. Suganuma, "Printing Technology BT - Introduction to Printed Electronics," K. Suganuma, Ed. New York, NY: Springer New York, 2014, pp. 23–48.

[88] J. C. Lötters, W. Olthuis, P. H. Veltink, and P. Bergveld, "The mechanical properties of the rubber elastic polymer polydimethylsiloxane for sensor applications," *J. Micromechanics Microengineering*, vol. 7, no. 3, pp. 145–147, Sep. 1997.

[89] D. Bashford, "Polyvinylidene Fluoride (PVDF) BT - Thermoplastics: Directory and Databook," D. Bashford, Ed. Dordrecht: Springer Netherlands, 1997, pp. 243–246.

[90] J. A. Chilton, "Ferroelectric Polymers BT - Plastics for Electronics," M. Goosey, Ed. Dordrecht: Springer Netherlands, 1999, pp. 243–291.

[91] N. Bosq, N. Guigo, J. Persello, and N. Sbirrazzuoli, "Melt and glass crystallization of PDMS and PDMS silica nanocomposites," *Phys. Chem. Chem. Phys.*, vol. 16, no. 17, pp. 7830–7840, 2014.

[92] D.-H. Kim *et al.*, "Dissolvable films of silk fibroin for ultrathin conformal bio-integrated electronics," *Nat. Mater.*, vol. 9, no. 6, pp. 1–7, 2010.

[93] B. Zhu *et al.*, "Silk Fibroin for Flexible Electronic Devices," *Adv. Mater.*, vol. 28, no. 22, pp. 4250–4265, Jun. 2016.

[94] J. W. Kim *et al.*, "Paper-Like, Thin, Foldable, and Self-Healable Electronics Based on PVA/CNC Nanocomposite Film," *Adv. Funct. Mater.*, vol. 29, no. 50, pp. 1–14, 2019.

[95] X. Wu *et al.*, "Thermally stable, biocompatible, and flexible organic field effect transistors and their application in temperature sensing arrays for artificial skin," *Adv. Funct. Mater.*, vol. 25, no. 14, pp. 2138–2146, 2015.

[96] A. Miyamoto *et al.*, "Inflammation-free, gas-permeable, lightweight, stretchable on-skin electronics with nanomeshes," *Nat. Nanotechnol.*, vol. 12, no. 9, pp. 907–913, 2017.

[97] L. Seminara, M. Capurro, P. Cirillo, G. Cannata, and M. Valle, "Electromechanical characterization of piezoelectric PVDF polymer films for tactile sensors in robotics applications," *Sensors Actuators A Phys.*, vol. 169, no. 1, pp. 49–58, Sep. 2011.

[98] Y. R. Wang, J. M. Zheng, G. Y. Ren, P. H. Zhang, and C. Xu, "A flexible piezoelectric force sensor based on PVDF fabrics," *Smart Mater. Struct.*, vol. 20, no. 4, p. 45009, 2011.

[99] A. V. Shirinov and W. K. Schomburg, "Pressure sensor from a PVDF film," *Sensors Actuators A Phys.*, vol. 142, no. 1, pp. 48–55, Mar. 2008.

[100] B. Gusarov *et al.*, "Thermal energy harvesting by piezoelectric PVDF polymer coupled with shape memory alloy," *Sensors Actuators A Phys.*, vol. 243, pp. 175–181, Jun. 2016.

[101] C. Sun, J. Shi, D. J. Bayerl, and X. Wang, "PVDF microbelts for harvesting energy from respiration," *Energy Environ. Sci.*, vol. 4, no. 11, pp. 4508–4512, 2011.

[102] V. Mittal, *Synthesis Techniques for Polymer Nanocomposites*. Weinheim, GERMANY: John Wiley & Sons, Incorporated, 2015.

[103] L. McKeen and L. McKeen, "Polyimides," *Eff. Steriliz. Plast. Elastomers*, pp. 169–182, Jan. 2012.

[104] J. Suikkola *et al.*, "Screen-Printing Fabrication and Characterization of Stretchable Electronics," *Sci. Rep.*, vol. 6, p. 25784, May 2016.

[105] X. Li and K. W. C. Lai, "Highly Flexible and Stretchable Structure Based on Au/Graphene Film and Polyurethane Yarn," in *2019 IEEE 19th International Conference on Nanotechnology (IEEE-NANO)*, 2019, pp. 117–120.

[106] Y. Zhang, Y. Huang, P. Liu, C. Liu, X. Guo, and Y. Zhang, "Highly stretchable strain sensor with wide linear region via hydrogen bond-assisted dual-mode cooperative conductive network for gait detection," *Compos. Sci. Technol.*, vol. 191, p. 108070, May 2020.

[107] C. Prisacariu, E. Scortanu, and S. Coseri, *Polyurethane Elastomers : From Morphology to Mechanical Aspects*. Vienna, AUSTRIA: Springer, 2011.

[108] K. Watanabe, Y. Eto, S. Takano, S. Nakamori, H. Shibai, and S. Yamanaka, "A new bacterial cellulose substrate for mammalian cell culture," *Cytotechnology*, vol. 13, no. 2, pp. 107–114, 1993.

[109] R. Portela, C. R. Leal, P. L. Almeida, and R. G. Sobral, "Bacterial cellulose: a versatile biopolymer for wound dressing applications," *Microb. Biotechnol.*, vol. 12, no. 4, pp. 586–610, Jul. 2019.

[110] H. Qi, "Nanocellulose-Based Functional Materials," in *Novel Functional Materials Based on Cellulose*, Cham: Springer International Publishing, 2017, pp. 69–87.

[111] H. M. C. Azeredo, H. Barud, C. S. Farinas, V. M. Vasconcellos, and A. M. Claro, "Bacterial Cellulose as a Raw Material for Food and Food Packaging Applications," *Front. Sustain. Food Syst.*, vol. 3, p. 7, 2019.

[112] D. Miorandi, S. Sicari, F. De Pellegrini, and I. Chlamtac, "Internet of things: Vision, applications and research challenges," *Ad Hoc Networks*, vol. 10, no. 7, pp. 1497–1516, Sep. 2012.

[113] R. C. Webb *et al.*, "Thermal Transport Characteristics of Human Skin Measured In Vivo Using Ultrathin Conformal Arrays of Thermal Sensors and Actuators," *PLoS One*, vol. 10, no. 2, p. e0118131, Feb. 2015.

[114] T. Vuorinen, J. Niittynen, T. Kankkunen, T. Lammi, and M. Mäntysalo, "Inkjet-printed push-buttons for epidermal electronics." Verlag für Wissenschaft und Bildung VWB, pp. 67-71 BT-Printing Future Days 2015, 2015.

[115] D.-J. Kim, H.-I. Shin, E.-H. Ko, K.-H. Kim, T.-W. Kim, and H.-K. Kim, "Roll-to-roll slot-die coating of 400 mm wide, flexible, transparent Ag nanowire films for flexible touch screen panels," *Sci. Rep.*, vol. 6, no. 1, p. 34322, 2016.

[116] J. Wang, M. Liang, Y. Fang, T. Qiu, J. Zhang, and L. Zhi, "Rod-Coating: Towards Large-Area Fabrication of Uniform Reduced Graphene Oxide Films for Flexible Touch Screens," *Adv. Mater.*, vol. 24, no. 21, pp. 2874–2878, Jun. 2012.

[117] G. A. Roth *et al.*, "Demographic and Epidemiologic Drivers of Global Cardiovascular Mortality," *N. Engl. J. Med.*, vol. 372, no. 14, pp. 1333–1341, Apr. 2015.

[118] W. H. O. (WHO), "World Health Statistics 2018: Monitoring health for the SDGs, sustainable development goals," Geneva, 2018.

[119] D.-H. Kim *et al.*, "Epidermal Electronics," *Science (80-.).*, vol. 333, no. 6044, pp. 838 LP – 843, Aug. 2011.

[120] E. Fung *et al.*, "Electrocardiographic patch devices and contemporary wireless cardiac monitoring," *Front. Physiol.*, vol. 6, no. MAY, 2015.

[121] P. Guzik and M. Malik, "ECG by mobile technologies," *J. Electrocardiol.*, vol. 49, no. 6, pp. 894–901, Nov. 2016.

[122] G. E. Dower, A. Yakush, S. B. Nazzal, R. V Jutzy, and C. E. Ruiz, "Deriving the 12-lead electrocardiogram from four (EASI) electrodes.," *J. Electrocardiol.*, vol. 21 Suppl, pp. S182-7, 1988.

[123] E. Atkins, "Pathogenesis of Fever," *Physiol. Rev.*, vol. 40, no. 3, pp. 580–646, Jul. 1960.

[124] J. I. Priego Quesada, F. P. Carpes, R. R. Bini, R. Salvador Palmer, P. Pérez-Soriano, and R. M. Cibrián Ortiz de Anda, "Relationship between skin temperature and muscle activation during incremental cycle exercise," *J. Therm. Biol.*, vol. 48, pp. 28–35, Feb. 2015.

[125] M. N. Sawka, S. N. Cheuvront, and R. W. Kenefick, "High skin temperature and hypohydration impair aerobic performance," *Exp. Physiol.*, vol. 97, no. 3, pp. 327–332, Mar. 2012.

[126] V. J. Houghton, V. M. Bower, and D. C. Chant, "Is an increase in skin temperature predictive of neuropathic foot ulceration in people with diabetes? A systematic review and meta-analysis," *J. Foot Ankle Res.*, vol. 6, no. 1, p. 31, Aug. 2013.

[127] G. Addor *et al.*, "A comparative study of reactive hyperemia in human forearm skin and muscle.," *Physiol. Res.*, vol. 57, no. 5, pp. 685–692, 2008.

[128] W. Honda, S. Harada, T. Arie, S. Akita, and K. Takei, "Wearable, Human-Interactive, Health-Monitoring, Wireless Devices Fabricated by Macroscale Printing Techniques," *Adv. Funct. Mater.*, vol. 24, no. 22, pp. 3299–3304, Jun. 2014.

[129] C. Bali, A. Brandlmaier, A. Ganster, O. Raab, J. Zapf, and A. Hübler, "Fully Inkjet-Printed Flexible Temperature Sensors Based on Carbon and PEDOT:PSS1," *Mater. Today Proc.*, vol. 3, no. 3, pp. 739–745, 2016.

[130] S. Y. Hong *et al.*, "Stretchable Active Matrix Temperature Sensor Array of Polyaniline Nanofibers for Electronic Skin.," *Adv. Mater.*, vol. 28, no. 5, pp. 930–5, Feb. 2016.

[131] Y. Chen, B. Lu, Y. Chen, and X. Feng, "Breathable and Stretchable Temperature Sensors Inspired by Skin," *Sci. Rep.*, vol. 5, p. 11505, Jun. 2015.

[132] Y. Yamamoto *et al.*, "Efficient Skin Temperature Sensor and Stable Gel-Less Sticky ECG Sensor for a Wearable Flexible Healthcare Patch," *Adv. Healthc. Mater.*, vol. 6, no. 17, 2017.

[133] G. Liu *et al.*, "A Flexible Temperature Sensor Based on Reduced Graphene Oxide for Robot Skin Used in Internet of Things," *Sensors*, vol. 18, no. 5, 2018.

PUBLICATIONS

PUBLICATION
I

Printable, Transparent, and Flexible Touch Panels Working in Sunlight and Moist Environments

Vuorinen T., Zakrzewski M., Rajala S., Lupo D., Vanhala J., Palovuori K., and Tuukkanen S.

FULL PAPER

Printable, Transparent, and Flexible Touch Panels Working in Sunlight and Moist Environments

*Tiina Vuorinen, Mari Zakrzewski, Satu Rajala, Donald Lupo, Jukka Vanhala,
Karri Palovuori, and Sampo Tuukkanen**

The ongoing revolution of touch-based user interfaces sets new requirements
for touch panel technologies, including the need to operate in a wide range
of environments. Such touch panels need to endure moisture and sunlight.
Moreover, they often need to be curved or flexible. Thus, there is a need for
new technologies suitable, for example, for home appliances used in the
kitchen or the bathroom, automotive applications, and e-paper. In this work,
the development of transparent and flexible touch panels for moist environ-
ments is reported. A piezoelectric polymer, poly(vinylidene difluoride) (PVDF),
is used as a functional substrate material. Transparent electrodes are fabri-
cated on both sides of a PVDF film using a graphene-based ink and spray
coating. The excellent performance of the touch panels is demonstrated in
moist and underwater conditions. Also, the transparent device shows very
small pyroelectric response to radiative heating in comparison to a non-trans-
parent device. Solution processable electrode materials in combination with
functional substrates allow the low-cost and high-throughput manufacturing
of touch panels using printing technologies.

1. Introduction

During recent years the user interfaces of electronic devices
have undergone a revolution, changing from old-fashioned
button-type controls towards embedded touch panels and touch
screens. It is expected that transparent control panels will
spread from mobile devices to be embedded as a part of built
environment. This raises major challenges to touch panel tech-
nology with requirements like functionality in moist or under-
water environment, integration into curved surfaces, flexibility,
temperature stability, and mechanical durability.

T. Vuorinen, M. Zakrzewski, Prof. D. Lupo,
Prof. J. Vanhala, Prof. K. Palovuori, Dr. S. Tuukkanen[+]
Tampere University of Technology (TUT)
Department of Electronics
Korkeakoulunkatu 3 P.O. Box 692, FI-33101
Tampere, Finland
E-mail: sampo.tuukkanen@tut.fi
Dr. S. Rajala
Tampere University of Technology (TUT)
Department of Automation Science and Engineering
Korkeakoulunkatu 3 P.O. Box 692, FI-33101, Tampere, Finland
[+]Present address: Aalto University, School of Chemical Technology,
Department of Materials Science and Engineering, P.O. BOX 16200,
00076 Aalto, Espoo, Finland

Printing and other solution processing
technologies have raised interest in the
electronic industry, and the push towards
organic and printed electronic systems is
strong at the moment.[1] The most inter-
esting perspective of the printing is ena-
bling of high throughput manufacturing
of electronic devices. Furthermore, the use of
solution processable organic and molecular
materials in the fabrication of electronic
devices is becoming popular due to their
potential ecological benefits, such as recycla-
bility or decomposability.[2] Even if organic
electronics cannot at present compete in
performance with silicon technology, it has
great potential to be utilized in large-area
applications and disposable low-end prod-
ucts.[1] Using small molecules, polymers,
or carbon based nanomaterials, instead of
metals and solid-state semiconductors, gives
rise to transparent electronic circuits, which
is a prerequisite for touch panel technology.

The use of conducting polymers, such as poly(3, 4-ethylened
ioxythiophene):poly(styrenesulfonate) (PEDOT:PSS), or carbon
based nanomaterials, such as graphene and carbon nanotubes
(CNT), enable fabrication of flexible or stretchable electrodes for
sensor applications.[3–5] These materials also have their limita-
tions. Although a single CNT can carry a few mA current,[6] con-
tact resistances between crossing tubes limit the overall conduc-
tivity of a randomly oriented CNT network.[7] Nevertheless, highly
conducting CNT networks have been recently demonstrated in
supercapacitors,[8–12] which are promising future energy storage
devices. While the degradation of conductivity of PEDOT:PSS
under ambient conditions has conventionally been a challenge,[13]
highly stable formulations have been recently obtained.[14]

Nowadays, there are several competing touch panel tech-
nologies available, but they all have some limitations such
as diminished functionality in moist and wet environment.
Water-proof touch panels are however required for example
in outdoor interactive panels and automotive touch panels as
well as control panels in swimming pools or shower walls and
mirrors. Capacitive, resistive, and optical sensing are the three
major technologies used in multi-touch sensing applications.[15]
The drawback with optical sensing methods is that they all
are highly affected by the surrounding lighting and cannot be
used with bended surfaces. A resistive touch panel consists
of two conductive sheets (coated for example with indium-tin-
oxide) and a layer of dot spacers in between. Pressing the panel

Materials
Views
www.MaterialsViews.com

ADVANCED
FUNCTIONAL
MATERIALS
www.afm-journal.de

causes the conductive top sheet to physically yield and contact the bottom layer.[16–18] The dot spacers prevent the contact of the top and the bottom sheets when the panel is not pressed. Thus, water droplets or sunlight do not cause artefacts in resistive panels. However, when immersed in water, the hydrostatic pressure yields the top sheet similarly as touch. With high enough hydrostatic pressure, this saturates the panel. For example, the hydrostatic pressure in 1 m depth corresponds to a medium touch pressure (1 N cm^{-2}). Hence, resistive touch panels face a trade-off between the sensitivity and underwater functionality. Capacitive sensing can be divided into two methods: surface capacitive and projected capacitive sensing. In projected capacitive touch sensing, the capacitance at each addressable electrode is measured.[19] A finger or a stylus close by disturbs the electromagnetic field and alters the capacitance. A touch on the surface can be measured from a change in the capacitance.[20–23] The major disadvantage of capacitive touch technology is the disturbance in moist environments. Normally, neither surface nor projected capacitive method is capable of functioning under water or with liquid droplets on the panel. Recently, examples of underwater projected capacitive sensing have been presented, however, with the expense of increased false touch rate.[24,25] Further drawbacks are the lack of pressure sensitivity, poor touch time resolution to the exact touch moment and dependence on the dielectric properties of the touching instrument. In practical applications, this means false detection with fast touch typing if the user is resting fingers on keys without intention to press the key and inability to detect fingers with gloves on.

One promising technology for touch devices is piezoelectric sensing.[26] The advantage of piezoelectric polymer films, such as poly(vinylidene difluoride) (PVDF), is that they are thin, flexible, lightweight, and they can be integrated into various shaped surfaces such as pillars or cylinders. The PVDF film can be easily sealed hermetically and thus, it can be used in several sensing applications due to its versatile properties. For instance, PVDF has a wide frequency range (from 0.001 Hz to 10^8 Hz) and a vast dynamic range (from 10^{-8} to 10^6 psi).[27] In addition, the PVDF material is sensitive to pressure changes, not to a static pressure. For example, hydrostatic pressure does not saturate a piezoelectric touch panel. A touch panel technology based on printable piezoelectric sensors has recently been demonstrated.[28–30] However, flexible, transparent, and water-proof piezoelectric touch panels have not been reported to date. Piezoelectric polymer films are interesting also for physiological measurements[3,4,31,32] and energy harvesting application.[33–37] In addition, piezoelectric polymer films have previously been used to manufacture flexible and transparent loudspeakers.[38,39]

This paper reports the successful implementation of a transparent and flexible piezoelectric touch panel technology. Unlike most competing technologies, these touch panels can also be utilized in moist environments due to the sensitivity to applied force instead of the capacitance change. In this paper, we demonstrate underwater functionality for the first time. In addition to the advantages of piezoelectric sensing over the existing technologies, the use of a piezoelectric polymer film as a functional substrate material enables high throughput manufacturing using roll-to-roll printing techniques. Transparent electrodes are made here from a graphene-based ink, which gives sufficient conductivity for this type of application.

2. Results and Discussion

2.1. Samples and Electrode Properties

The electrodes for piezoelectric film-based touch panels were fabricated from three different nanostructural carbon inks. One of the inks contained a CNT/xylan nanocomposite, and the two others were composites of graphene and a conducting polymer. Electron-beam evaporated copper electrodes were used as reference samples. Photos of fabricated samples are shown in **Figure 1**. The electrode deposition was done on both sides of the PVDF film to accomplish the triple-layered structure, in which four arrow-shaped keys formed the top layer on the PVDF, and one large square pattern formed a ground plane on the opposite side of the film (see Figure 1(a-c)). Two different solution-processing methods, doctor blading and spray-coating, were used for electrode deposition, and the patterning was done using mechanical masks. The CNT and the graphene screen inks were spread with a doctor blade across the mechanical mask, and the graphene inkjet ink was spray-coated with an airbrush (Silverline). For the reference sample 100 nm thick copper electrodes were fabricated on PVDF film using vacuum evaporation and a mechanical mask.

The measured sheet resistances for different electrode materials are listed in **Table 1**. The mean and the standard deviation from 25 repetitive measurements per each sample are presented i.e., the measurement was repeated five times for each key and the large ground plane.

The piezoelectric touch panels were laminated with a pouch-laminator (Fellowes, Inc.) to provide a waterproof enclosure and some mechanical support. To ensure the waterproof enclosure during water immersion tests, a water absorption test was executed according to the European standard EN ISO 62:2008[40] to measure how much the lamination covering the panels would absorb water in 24 h. The water absorbance measurements showed only a 0.37 wt% change in average, which indicates that the lamination material was suitable for water immersion tests.

The transparency and the flexibility of the thin graphene sample S5 are seen in Figure 1e and 1f. The photonic transmission was measured in the 420–650 nm range following the standard MIL-DTL-62420. The transparency of the arrow-shaped keys in the sample S5 was 64.7%. The transparency can be considered good because the transparency of the sole lamination film was 74.1% and the transparency of the lamination film and the PVDF substrate together was 69.6%. Thus, most of the optical losses are resulting from the interference and reflections in the lamination films.

2.2. Sensor Sensitivity Measurements

Table 1 summarizes the measured sensor sensitivities for each sensor with solution-processed electrodes (S1–S3, S5). The sensor sensitivity is presented as the mean ± standard deviation of eight repetitive measurements per each sensor type.

**ADVANCED
FUNCTIONAL
MATERIALS**

www.afm-journal.de

Materials
Views

www.MaterialsViews.com
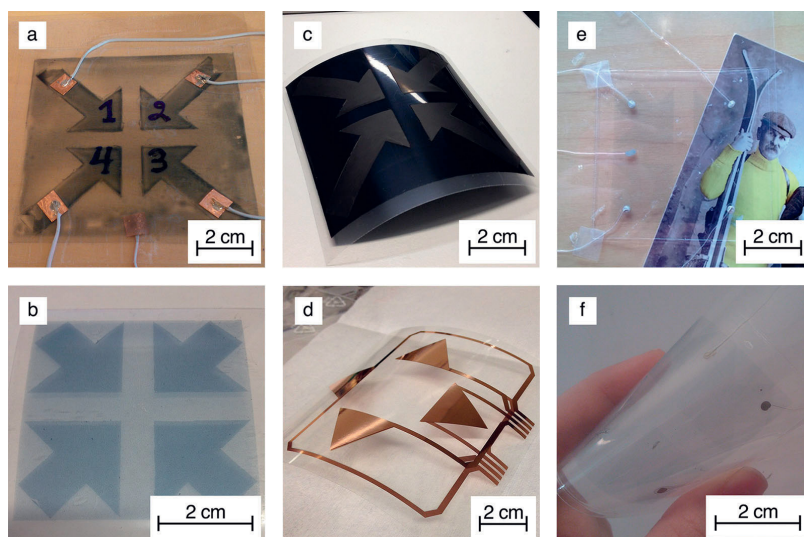
Figure 1. Photos of the samples a) S1, b) S2, c) S3, d) S4, and e,f) S5. The high transparency (e) and bendability (f) of the sample S5 is illustrated as placed above a postcard and when bent.

Only one key of each sensor type is measured. As presented in Table 1, the electrode material affects the sensitivity. On the other hand, also the lamination may affect by producing additional stresses to the PVDF material.

The touch sensor sensitivities were also measured using three different forces (approximately 0.3 N, 1.3 N, and 3.4 N) to find out their dependence on the touch force. The forces correspond to low, medium and high forces used with touch panels (evaluated with a balance). The results are shown in **Figure 2**. It was found that the amount of generated charged increased very linearly as a function of applied force. Hence, the sensitivities of the sensors are constant for various force regimes. Based on the sensitivity measurements, repeatability was good and fatigue effect was not observed.

2.3. Panel Operation in Dry and Moist Environments

The response of the touch panels were measured using the setup described in **Figure 3** consisting of a charge amplifier,

Table 1. The measured sheet resistances and sensitivities.

Sample name	Electrode material	Sheet resistance [Ω sq^{-1}]	Sensor sensitivity [pC N^{-1}]
S1	Graphene screen ink	620 ± 10	44.6 ± 4.1
S2	Graphene inkjet ink, thick	76 ± 8	29.7 ± 5.2
S3	CNT/xylan ink	68 ± 8	26.4 ± 2.9
S4	Copper	1.0 ± 0.2	–
S5	Graphene inkjet ink, thin	1400 ± 20	34.9 ± 5.8

and an analog-to-digital converter (ADC). The temperature of the touch panel was measured simultaneously.

In addition to pressing the panel with a finger, a custom-made stylus was used in water immersion tests to rule out the pyroelectric phenomena caused by a human finger maintaining the body temperature. The stylus consisted of a metallic weight formed into a cylinder with a rubber tip on top of the cylinder mimicking a real fingertip.

To demonstrate that the panel works in a moist environment and underwater, several tests were conducted in different measurement configurations both in a laboratory environment and by immersing them in a sink filled with water. **Figure 4** shows the response signals obtained in the shower, in dry ambient air, and in underwater conditions. It can be noticed from
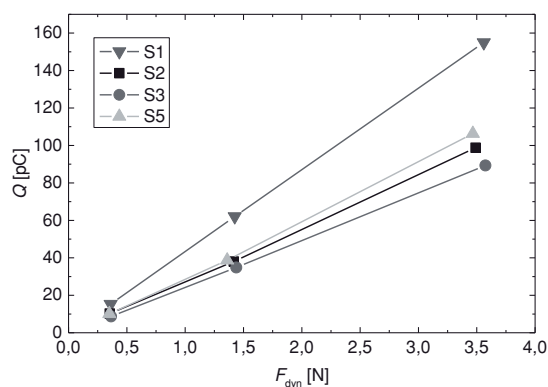
Figure 2. Linearity of the touch sensors S1, S2, S3, and S5. The charge developed by the sensor [pC] is presented as a function of the dynamic excitation force [N] applied to the sensor.

Materials
Views
www.MaterialsViews.com

ADVANCED
FUNCTIONAL
MATERIALS
www.afm-journal.de

FULL PAPER
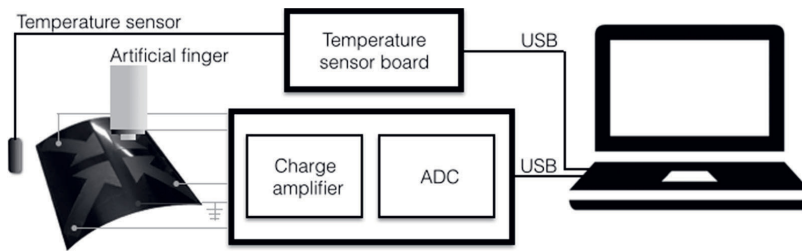
Figure 3. The sensor response measurement setup.

Figure 4 that there is no cross-talk effect between two adjacent keys. However, when the panels were not fixed to the rigid surface during the operation, considerable cross-talk between adjacent keys was observed because of the bending of the PVDF film.

2.4. Pyroelectric and Piezoelectric Responses

There are two simultaneous effects, pyroelectric and piezoelectric, which define the overall touch response of piezoelectric panels.[30] When a key is pressed, the two responses are superimposed in the resulting signal: mechanical pressing causes a piezoelectric effect, and temperature change causes a pyroelectric effect. These effects happen simultaneously, making them hard to separate. The pyroelectric response signal is proportional to the temperature difference between the finger/stylus and the touch panel, whereas the piezoelectric response is proportional to the applied force. In many applications, the timescales for mechanically induced deformations are different than those associated with thermal processes.[27] Heat transfer mechanisms are typically slower. Therefore, the resulting pyroelectric effect takes place at lower frequencies than the piezoelectric effect and thus, the mechanical and
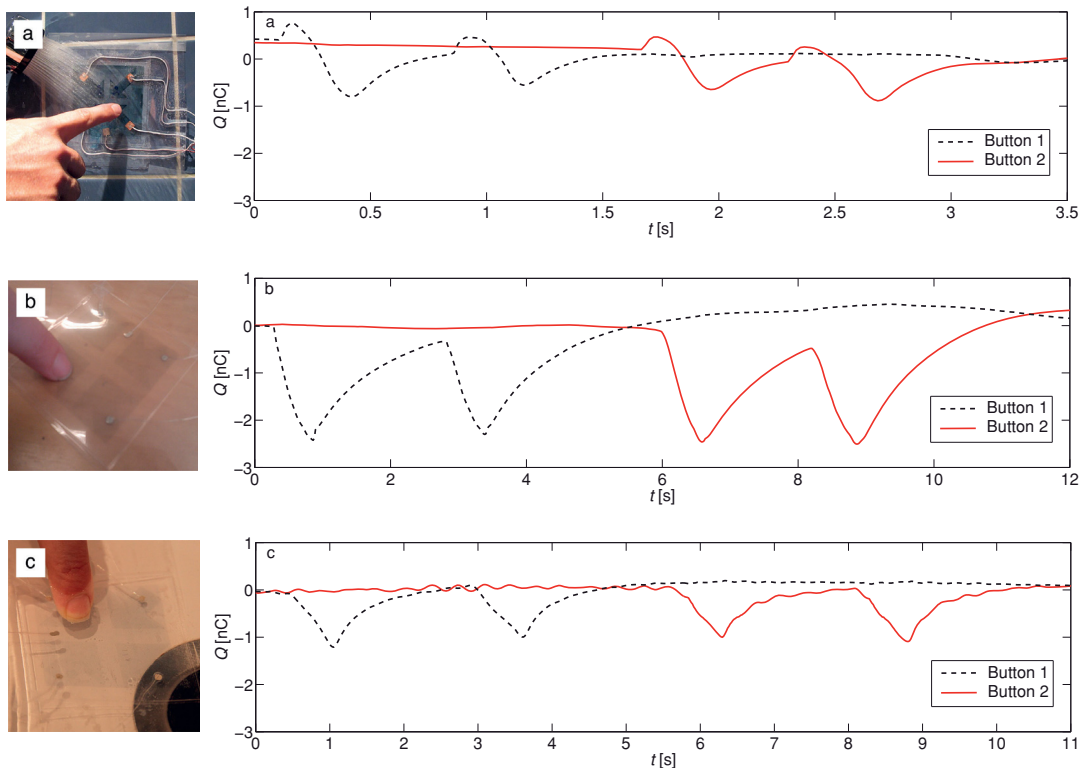
Figure 4. The response from a) the shower tests with sample S1 and from b,c) the immersion tests before and during the immersion with sample S5.

**ADVANCED
FUNCTIONAL
MATERIALS**

www.afm-journal.de

*Materials
Views*

www.MaterialsViews.com

Figure 5. Positive and negative pyroelectric response curves from sample S5 obtained at two temperatures, a,b) at 20 °C and c,d) 50 °C, and touching either with a,c) stylus and b,d) finger. Each key is pressed twice.

thermal signals can be separated by frequency filtering.[27,41] This, however, is an application specific issue. The phenomena of simultaneous piezo- and pyroelectric effects are demonstrated in **Figure 5**, where the response curves from sample S5 immersed in 20 °C and at 50 °C water are plotted in the cases of pressing with finger and stylus. When the temperature of the finger/stylus was higher than the temperature of the touch panel, the m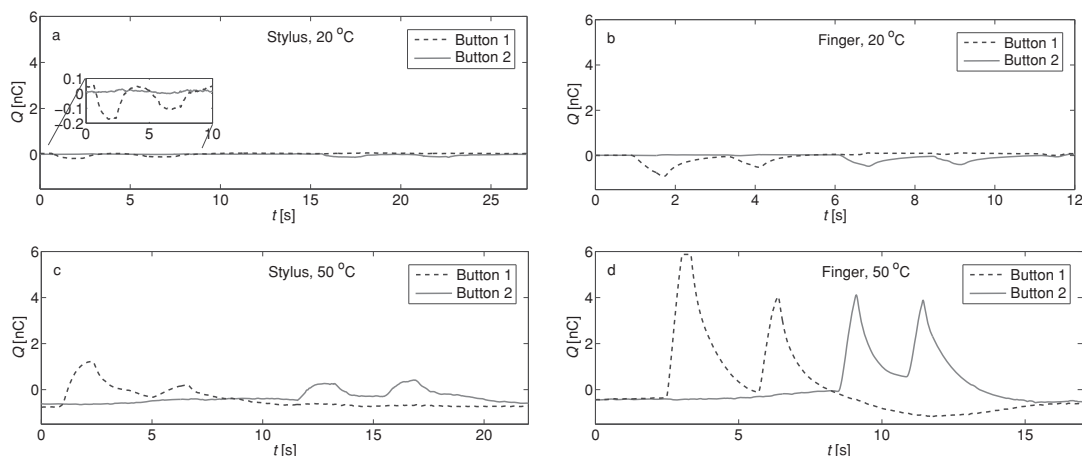easured change is negative (see Figure 5a,b); and when the temperature of the touch panel exceeded the temperature of the finger/stylus, the observed signal direction is positive (see Figure 5c,d). Each graph in Figure 5a-d presents the response signals from two adjacent keys and each key is pressed twice either with a finger or stylus.

2.5. The Operation in Sunlight

In real life applications, when the touch panel is exposed to the sunlight, the absorption of heat results to a pyroelectric response signal. The touch panels were tested during a sunlight exposure, and the resulting signal responses are shown in **Figure 6**a for samples S3 (CNT/xylan) and S5 (Graphene, thin). To compare the pyroelectric and piezoelectric responses, the magnitude of the response of pressing keys with a stylus is shown in Figure 6b with an equal scale. In Figure 6a, a large pyroelectric response is seen in the sample S3. In fact, the response is so large that it saturates the ADC. This is solely a pyroelectric effect as no touch or pressure change was involved. The response in graphene (S5), on the other hand, is on the same order of magnitude as the pressure response. However, the pyroelectric response is much slower and thus it may be possible to separate the effects based on response speed. The result is expected: the more transparent the panel is, the less it will be warmed in the sunlight, and the smaller pyroelectric response is seen in the signal. The insensitivity to sunlight is a highly desirable effect in touch panels, especially in outdoor applications.

In comparison, Rendl et al. proposed the use of an additional foil which acts as a temperature absorbing layer to reduce the pyroelectric response.[30] However, such absorbing layer plate is not transparent, which is the key characteristic of our proposed touch panel technology. Furthermore, the absorbing layer decreases the effect only about 60% which is not enough in practical applications.

2.6. The Temperature Dependency of the Response

The charge generated by the sensor versus temperature graphs obtained from the water immersion experiment are presented in **Figure 7**. The first and last data points at 30 °C room air (marked with "*x*") are measured before and after the immersion, respectively. The solid square markers represent keystrokes done underwater with the stylus, and the open sphere markers represent the keystrokes done with a finger. As
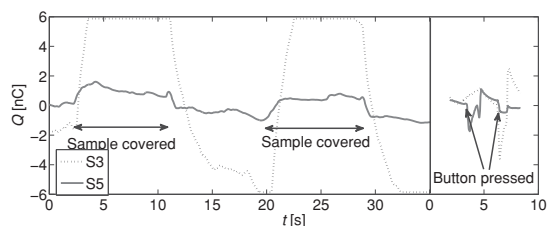
Figure 6. Sunlight exposure test results from the samples S3 and S5. a) The response signal in sunlight vs in the dark (sample covered). b) The response while pressed with the stylus in sunlight. The transparent graphene sample S5 shows much smaller pyroelectric response (less radiative heating) than the non-transparent CNT sample S3, whereas the magnitude of the pressure response is on the same order of magnitude in both samples. Also, the effect of the pressure response is much faster than that of the light exposure. Note that the scale is the same in both the figures.

Materials
Views
www.MaterialsViews.com

ADVANCED
FUNCTIONAL
MATERIALS
www.afm-journal.de

FULL PAPER
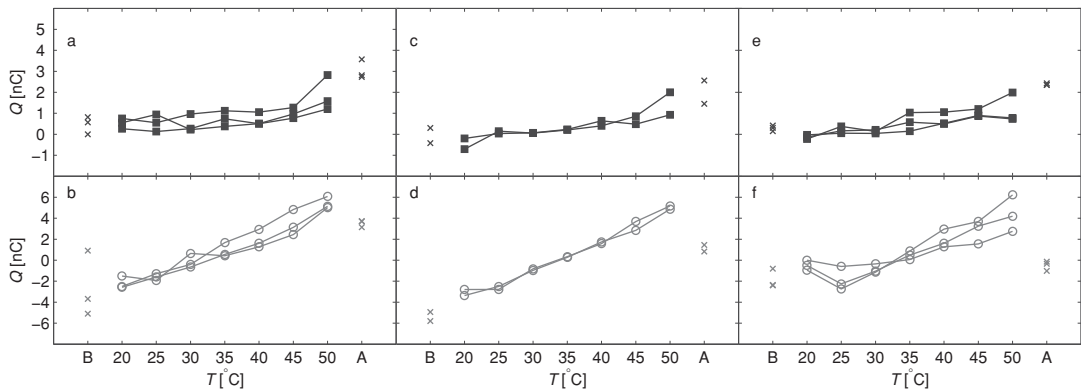
Figure 7. Measured response amplitudes in underwater conditions for samples a,b) S2, c,d) S4, and e,f) S5 when pressing sequence is done by the stylus (squares) and by the finger (circles). A-axis tick labels B and A stands for "before" and "after" the immersion test, respectively.

observed from the curves, the response signals are linearly dependent on the water temperature.

A highly temperature-dependent response was observed in the case of finger touch because of the larger role of pyroelectric effect. However, in the case of stylus touch, the temperature-dependency is less significant. It is important to notice from Figure 7 that a stylus touch does not heat (or cool) the panel electrode as much as a finger touch. This indicates that the piezo-electric effect plays a bigger role when the panel is not heated (or cooled) by the finger. In all cases, the response to touch was largest when the water temperature was furthest away from the stylus/ finger temperature.

3. Conclusion

In this paper, it has been demonstrated how flexible and transparent touch panel electrodes can be manufactured from a solution processable graphene-based ink, using a spray coating method, onto a PVDF film. Other solution pro-cessable electrode materials and e-beam evaporated copper electrodes were used for comparison. Transparent and flex-ible panels can be integrated, e.g., on curved, rigid surfaces and thus, they offer more possibilities for design issues. The results showed that touch panels were functional both in moist environment and underwater. In the water immer-sion tests, the overall response of the touch panel was the summed response from the piezo- and pyroelectric effects. It was observed that a finger touch response showed a higher temperature-dependence than a stylus touch response, because of the larger role of pyroelectric effect. In the sun exposure test, the sunlight had a much smaller impact on the transparent graphene-based electrodes than on the black CNT-based electrodes. These results show that piezoelectric PVDF touch panels with graphene-based solution processed electrodes are convenient, for example, for outdoor applica-tions, because water and sunlight would not disrupt their functionality.

4. Experimental Section

Materials: A CNT/xylan nanocomposite ink, which was still in development phase, was obtained from Morphona Ltd.[9,10] and graphene/conductive polymer composite inks were purchased from Innophene. Graphene inks were PHENE+ I3015 formulated for inkjet printing, and PHENE+ P3014 formulated for screen printing. The CNT ink has a 3.5 wt% solid content that includes 2.5 wt% of CNT and 1 wt% of xylan. The Innophene inkjet ink consists of 1–5 wt% polymer and 1–5 wt% graphene and it also includes organic solvents such as diethylene glycol and ethanol. The ingredients of the Innophene screen printing ink were 1.0–5.0 wt% polymer, less than 1.0 wt% graphene, and solvents such as diethylene glycol, ethanol, and propylene glycol. A silver flake ink[3] and a copper adhesive tape were used to attach wires to the panel. The silver flake ink (Acheson Electrodag from Henkel) had solid content of 72 wt% containing n-propylacetate as the solvent. A piezoelectric 110-μm-thick PVDF film (purchased from Measurement Specialities Inc.) was used as the functional substrate material for all the fabricated touch panels. PVDF is a semicrystalline polymer having a solid and homogenous structure. The change in film thickness due to an external force compressing the film generates a charge and thus, a voltage to appear at the electrodes. This phenomenon is known as the direct piezoelectric effect. The PVDF material is not suitable for static measurements and only the change of an external pressure can be measured. The piezoelectric coefficients provided by the manufacturer are $d_{33} = -33 \times 10^{-12}$ C N^{-1} (compression) and $d_{31} = 23 \times 10^{-12}$ C N^{-1} (stretching).[27] These coefficients can be also expressed in the units (m m^{-1}) (V m^{-1})$^{-1}$ corresponding to a deformation per electric field strength. The Young's Modulus of $2-4 \times 10^9$ N m^{-2} was reported by the manufacturer.[27] The piezoelectric coefficients of the PVDF material tend to increase with temperature; the temperature dependence is reported e.g., in references.[27,42] The PVDF material is also pyroelectric: as the film is heated, the dipoles within the film exhibit random motion by thermal agitation, causing a reduction in the average polarization of the film and thus generating a charge build up on the film surfaces. The amount of electrical charge produced per degree of temperature increase is described by the pyroelectric charge coefficient ($p = 30 \times 10^{-6}$ C m^{-2} K^{-1}).[27]

Manufacturing Methods: A laser cut stencil (purchased from Easy-Cad Oy) was used as a mechanical mask for copper evaporation. Masks used to define ink patterns were fabricated from 125-μm-thick poly(ethylene terephthalate) (PET) film (Melinex ST506 from Dupont), and cut-out holes were made by carving them with a craft knife. The arrow shaped keys were chosen to simulate a remote control device for tuning of

volume and channel in a media player. Temporary bonding adhesive (Zig 2-Way Glue) was used to secure PET masks in place during coating. The adhesive also prevented the ink from leaking underneath the mask. During the spray-coating, the sample was placed on top of a 60 °C hot plate so that the hot plate would dry the ink just enough to ensure even layer formation. Without the hot plate, the ink aerosol would agglomerate and form large individual drops on the surface of the PVDF. After each electrode deposition, samples S2 and S5 (Graphene, inkjet) were dried in a convection oven; the thicker panel for 15 min at 65 °C and the thinner panel for 8 min at 65 °C. Since the electrodes were deposited on both sides of the PVDF substrate, each panel underwent two oven treatments. After the ink deposition, the manually doctor-bladed sample S3 (CNT) was left to dry at room temperature and sample S1 (Graphene, screen) was dried in a convection oven for 10 min at 60 °C. The wiring for the piezoelectric touch panels was made by attaching a wire with silver ink to each of the keys and one to the square pattern. In the thicker graphene panel, insulated single-strand wires were used. However, in the thinner graphene panel, individual wire strands from an insulated wire bundle were used to maximize the transparency of the touch panel.

Sheet Resistance Measurement: A multimeter (Keithley 3435 100 W SourceMeter) and an in-house four-point probe were used in sheet resistance measurements.[3] The four-point probe has four spring probes, two current-carrying and two voltage-sensing, placed in line with equal spacing ($s = 3$ mm). Finally, the corrected sheet resistance was calculated using equation $R_S = G \times (\pi/\ln2) \times (V/I)$, where I is the applied current between the two outermost probes, V the measured voltage between two innermost probes and G an additional geometric correction factor which is determined by sample dimensions and the probe spacing.[43] The geometric factors for arrow patterns were $G = 0.635$.

Water Absorption Measurement: The procedure for determining the water absorption was done by cutting six 6.1 cm × 6.1 cm pieces out of a single, previously heat laminated, lamination pouch (composed of two 125 µm thick sheets). Samples were dried in a convection oven at 50 °C for 24 h, and after cooling back to room temperature, they were immersed in distilled water for 24 h. To determine the percentage change on mass, indicating to the amount of water absorbed, each sample was weighed before and after the water immersion.[40]

Optical Transparency Measurement: The transparency measurement was conducted based on the principles of the standard MIL-DTL-62420. The photonic transmission at wavelength range 420–650 nm was measured using an Ocean Optics spectrometer. The incident light is produced by halogen lamp D65. The light is transferred to the sample through an optical fiber and collected again by a second fiber transferring the light to the photodetector.

Sensitivity Measurements: The sensor sensitivity measurement setup is previously reported.[3,31] Briefly, the Brüel & Kjaer Mini-Shaker Type 4810 was used in the sensitivity measurements to provide a dynamic excitation force. A sinusoidal input for the shaker was provided with a Tektronix AFG3101 function generator. A pretension, which produces static force of about 3 N, was used to keep the sensor in place. A commercial high sensitivity dynamic force sensor (PCB Piezotronics, model number 209C02) and a load cell (Measurement Specialties Inc., model number ELFS-T3E-20L) were used as reference sensors for the dynamic excitation and static forces. The charge developed by the sensor was measured with a custom-made combination of a charge amplifier and a 16-bit AD-converter. The sensor key element was excited a 10 s period with a dynamic, sinusoidal 2 Hz input signal of 1000 mV (peak to peak), resulting in approximate force of 1.3 N. The four excitations were done by applying the force in the middle of the sensor. The excitations were repeated on both sides of the sensor, resulting in a total of eight excitations per sensor key element.

Sensor Response Measurement Setup: Sensor signals need to be amplified before digitizing. A charge amplifier with the amplification of 0.210 V $(nC)^{-1}$ was used. The conversion was done with a 16-bits analog-to-digital converter (ADC) (model ADS8344 from Texas Instruments). A sampling frequency of 57 Hz was used. With this set up, we were able to measure charges between –6 nC and 6 nC. The water temperature was measured simultaneously during the response measurement with a temperature sensor (model 18B20 from Dallas), which was attached to the glass plate next to the samples with a double-sided adhesive tape. A schematic of the sensor response measurement setup is shown in Figure 3.

Sunlight Exposure Test: For the sunlight exposure test, the thin graphene sample S5 and the CNT sample S3 were attached side-by-side to the same transparent plastic plate with double-sided tape. This ensured that environmental changes happened simultaneously to both samples. The plate was positioned next to an open door and turned towards the sun. The ambient air temperature was 19 °C in the beginning of the measurement. Then, a metal plate was positioned to block the sun exposure to the samples.

Moist Environment Tests: In the shower tests, the sample S1 was attached to the wall using PET film and temporary bonding adhesive. Tests were performed under a spray of water in a shower. The functionality tests for samples S2–S5 were performed in both laboratory environment and by immersing them in a sink filled with tap water. The samples were immersed in the depth of approximately 3.5 cm in stationary water. The sequence of pressing test consisted of two keystrokes per key with both a finger and a stylus. From the response curves, a maximum deviation (either positive or negative) from the signal base level is interpreted as a response value. In the water immersion tests the first test sequence was performed on a table before the immersion. The next six sequences were performed underwater, and between each sequence, the water temperature was increased by 5 °C, starting from a temperature of 20 °C to the maximum temperature of 50 °C. After the immersion, the touch panel was lifted out from the sink, and the pressing sequence was executed for the last time after the panel had cooled down to approximately 30 °C.

Acknowledgements

[1] White Paper "*OE-A Roadmap for Organic and Printed Electronics*" 5th edition, Organic and Printed Electronics Association, Frankfurt **2013**.

[2] *Towards Green Electronics in Europe,* Strategic Research Agenda (SRA) for Organic and Large-Area Electronics (OLAE), **2009**.

[3] S. Tuukkanen, T. Julin, V. Rantanen, M. Zakrzewski, P. Moilanen, K. E. Lilja, S. Rajala, *Synth. Met.* **2012**, *162*, 1987.

[4] S. Tuukkanen, T. Julin, V. Rantanen, M. Zakrzewski, P. Moilanen, D. Lupo, *Jpn. J. Appl. Phys.* **2013**, *52*, 05DA06.

[5] S. Tuukkanen, M. Hoikkanen, M. Poikelispää, M. Honkanen, T. Vuorinen, M. Kakkonen, J. Vuorinen, D. Lupo, *Synth. Met.* **2014**, *191*, 28.

[6] S. Tuukkanen, S. Streiff, P. Chenevier, M. Pinault, H.-J. Jeong, S. Enouz-Vedrenne, C. S. Cojocaru, D. Pribat, J.-P. Bourgoin, *Appl. Phys. Lett.* **2009**, *95*, 113108.

[7] D. S. Hecht, R. B. Kaner, *MRS Bull.* **2011**, *36*, 749.

[8] S. Lehtimäki, M. Li, J. Salomaa, J. Pörhönen, A. Kalanti, S. Tuukkanen, P. Heljo, K. Halonen, D. Lupo, *Int. J. Elect. Power Energy Syst.* **2014**, *58*, 42.

[9] S. Lehtimäki, J. Pörhönen, S. Tuukkanen, P. Moilanen, J. Virtanen, D. Lupo, *Mater. Res. Soc. Symp. Proc.* **2014**, 1659.

[10] S. Lehtimäki, S. Tuukkanen, J. Pörhönen, P. Moilanen, J. Virtanen, M. Honkanen, D. Lupo, *Appl. Phys. A* **2014**, DOI: 10.1007/s00339-014-8547-4.

Materials
Views
www.MaterialsViews.com

ADVANCED
FUNCTIONAL
MATERIALS
www.afm-journal.de

FULL PAPER

[11] M. Kaempgen, C. K. Chan, J. Ma, Y. Cui, G. Gruner, *Nano Lett.* **2009**, *9*, 1872.

[12] C. Z. Meng, C. H. Liu, S. S. Fan, *Electrochem. Commun.* **2009**, *11*, 186.

[13] S. Kirchmeyer, K. Reuter, *J. Mater. Chem.* **2005**, *15*, 2077.

[14] A. Elschner, W. Lövenich. *MRS Bull.* **2011**, *36*, 794.

[15] M. Frisch, J. Heydekorn, R. Dachselt, *ITS '09 Proc. ACM Int. Conf. Interactive Tabletops Surf,* ACM, New York, **2009**, 149.

[16] F. N. Eventoff, *U.S. Patent No. 4313227*, **1979**.

[17] I. Rosenberg, K. Perlin, *ACM Trans. Graph.* **2009**, *28*, 65.

[18] E. Choi, J. Kim, S. Chun, A. Kim, K. Lee, M. Jeong, C. Lim, T. Isoshima, M. Hara, S.-B. Lee, *J. Nanosci. Nanotechnol.* **2011**, *11*, 5845.

[19] *Touch technology brief, Projected capacitive technology,* 3M, **2013**.

[20] P. Dietz, L. Darren, *UIST '01 Proc. 14th Annu. ACM Symp. User Interface Software Technol.*, Mitsubishi Electric Research Laboratories, Inc., Cambridge, MA **2001**, 219.

[21] S. P. Jobs, *U.S. Patent No. 7479949B2*, **2009**.

[22] W. Westerman, *Hand Tracking, Finger Identification and Chordic Manipulation on a Multi- Touch Surface* PhD thesis, University of Delaware **1999**.

[23] K. Kim, K. Shin, J.-H. Han, K.-R. Lee, W.-H. Kim, K.-B. Park, B.-K. Ju, J. J. Pak, *Electron. Lett.* **2011**, *47*, 118.

[24] NXP Semiconductors, AN11122, *Water and condensation safe touch sensing with the NXP capacitive touch sensors*, Application note, **2014**.

[25] T. Gary, *Projected Capacitive Touch Panels Designed for Marine Applications* Ocular, **2013**.

[26] G. M. Krishna, K. Rajanna, *IEEE Sensors J.* **2004**, *4*, 691.

[27] *Measurement Specialties Inc., Piezo film sensors, Technical manual.* Available online at: http://www.meas-spec.com (accessed: 7 January 2014).

[28] M. Zirkl, G. Scheipl, B. Stadlober, A. Haase, L. Kuna, J. Magnien, G. Jakopic, J. R. Krenn, A Sawatdee, P. Bodö, P. Andersson, *Procedia Eng.* **2010**, *5*, 725.

[29] M. Zirkl, A Sawatdee, U. Helbig, M. Krause, G. Scheipl, E. Kraker, P. A. Ersman, D. Nilsson, D. Platt, P. Bodö, S. Bauer, G. Domann, B. Stadlober, *Adv. Mater.* **2011**, *23*, 2069.

[30] C. Rendl, P. Greindl, M. Haller, M. Zirkl, B. Stadlober, P. Hartmann, *UIST '12 Proc. 25th Annu. ACM Symp. User Interface Software Technol.* **2012**, *509*.

[31] S. Rajala, J. Lekkala. *IEEE Sensors J.* **2012**, *12*, 439.

[32] S. Kärki, J. Lekkala, H. Kuokkanen, J. Halttunen, *Sens. Actuators A Phys.* **2009**, *154*, 57.

[33] J. Pörhönen, S. Rajala, S. Lehtimäki, S. Tuukkanen, unpublished.

[34] S. P. Beeby, M. J. Tudor, N. M. White. *Meas. Sci. Technol.* **2006**, *17*, R175.

[35] H. S. Kim, J.-H. Kim, J. Kim. *Int. J. Precision Eng. Manufact.* **2011**, *12*, 1129.

[36] J. G. Rocha, L. M. Gonçalves, P. F. Rocha, M. P. Silva, S. Lanceros-Méndez, *IEEE Trans. Ind. Electron.* **2010**, *57*, 813.

[37] A. Khaligh, P. Zeng, C. Zheng, *IEEE Trans. Ind. Electron.* **2010**, *57*, 850.

[38] S. C. Xu, B. Y. Man, S. Z. Jiang, C. S. Chen, C. Yang, M. Liu, X. G. Gao, Z. C. Sun, C. Zhang, *Appl. Phys. Lett.* **2013**, *102*, 151902.

[39] K. Y. Shin, J. Y. Hong, J. Jang, *Chem Commun.* **2011**, *47*, 8527.

[40] *Plastics – Determination of water absorption,* European standard ISO 62:2008.

[41] L. Persano, C. Dagdeviren, Y. Su, Y. Zhang, S. Girardo, D. Pisignano, Y. Huang, J. A. Rogers, *Nat. Commun.* **2013**, *4*, 1633.

[42] A. Vinogradov, Piezoelectricity in polymers, *Encyclopedia of Smart Materials*John Wiley & Sons, New York **2000**.

[43] H. Topsoe, *Geometric correction factors in four point resistivity measurement, Bull.* Four-Point-Probes. Powered by Bridge Technology **1968**, 472–13 Available online at: http://www.fourpointprobes.com/haldor.html (accessed: 11 February 2014).

PUBLICATION
II

Printed, Skin-Mounted Hybrid System for ECG measurements

Vuorinen T., Vehkaoja A., Jeyhani V., Noponen K., Onubeze A., Kankkunen T., Puuronen A. K., Nurmentaus S., Preejith P. S., Joseph J., Seppänen T., Sivaprakasam M., and Mäntysalo M.

Printed, Skin-Mounted Hybrid System for ECG Measurements

Tiina Vuorinen[1*], Antti Vehkaoja[1], Vala Jeyhani[1], Kai Noponen[2], Augustine Onubeze[3], Timo Kankkunen[1], Anna-Kaisa Puuronen[3], Sampo Nurmentaus[3], Preejith S. P. [4], Jayaraj Joseph[4], Tapio Seppänen[2], Mohanasankar Sivaprakasam[4], Matti Mäntysalo[1]

[1]Tampere University of Technology, Finland
[2]University of Oulu, Finland
[3]Metropolia, Finland
[4]HTIC, IIT Madras, India
*Tampere University of Technology, Department of Electronics and Communications Engineering,
Korkeakoulunkatu 3, 33720, Tampere, Finland
Corresponding author: tiina.vuorinen@tut.fi

Abstract

In this paper we report a design and fabrication process for a screen printed, skin-mounted hybrid system for electrocardiogram (ECG) measurements. The system consists of printed electrodes on a stretchable bandage substrate designed to be attached to the chest, an electronics module, and a data receiving device. The electronics unit is reversibly attached to the single-use electrode bandage to measure the ECG data. The ECG data is then transmitted to a mobile device via Bluetooth Low Energy and the mobile device then displays the data graphically and sends it further a cloud for storing and further analysis. The attained quality of the measured ECG signals is fully satisfactory to compute important cardiac parameters and after preprocessing the signal could be used for more profound analysis of ECG wave shapes.

Introduction

Vital sign monitoring is evolving from stationary, wire-connected monitoring to a mobile monitoring with wireless sensor systems. Monitoring systems are shrinking in physical size and weight, and the monitoring electronics are brought closer to the patient, as is already done with wearable measurement devices. Several physiological parameters can be measured without penetrating the most outer layer of the human body, the skin. Consequently, unobtrusive body monitoring, where the monitoring is done with skin-mounted devices, is a fast growing research field.

Continuous vital sign monitoring might tremendously benefit several patient groups. For example, cardiac patients may experience unpleasant sensations from the heart outside the hospital environment, and it might be crucial to be able to verify the degree of criticalness immediately when the symptoms arise. To improve the skin/sensor interface and wearability of the devices (comfort and ease of application) in these tracking situations, the development is transitioning from rigid and planar electronic systems towards more adaptable, skin-mounted electronics [1,2].

Skin-mounted electronics or epidermal electronics refers to electronic systems that have several beneficial properties, such as elasticity, thin structure and lightweight, to be mounted on the bodies' epidermis (outer layer of the skin) [3]. Skin mounted electronic systems can provide new kinds of medical applications to measure vital signs non-invasively or even offer drug delivery mechanisms through the skin [4]. To reduce costs and waste material related to manufacturing of epidermal electronics, additive screen printing can be utilized in place of multiphase subtractive lithographic techniques.

Here we report a system level description, fabrication process and electrical characterization results for a printed, skin-mounted hybrid system for electrocardiogram (ECG) measurements. Both the conductors and the electrodes on a bandage substrate were fabricated using stretchable silver/silver chloride ink and screen printing. Stretchable silver ink was deposited on top of a 50-μm-thick polyurethane film, which was then heat laminated with transparent adhesive film to provide the adhesive layer for the system. The manufacturing process together with the stretchable substrate and ink enable cost-efficient fabrication for stretchable hybrid systems.

The resulted skin-mounted system is designed for measuring the ECG using a small area electrode configuration called EAS, that is a subset of an EASI lead system introduced by Dower et al [5]. In EAS lead configuration three electrodes are located at the lower part of the sternum (electrode E), at the standard ECG V5 (electrode A) and at manubrium (electrode S). Using this small area electrode configuration makes it possible to integrate a rigid ECG measurement module with the stretchable bandage type of a substrate, and because of this, it can be used also in ambulatory situations.

ECG measurements were conducted while the test person was sitting, lying down and when the person was walking. The quality of the measured ECG signals is fully satisfactory to compute heart rate and many other important cardiac parameters. After proper preprocessing, the measured signals also offer potential for morphology analysis of ECG wave shapes.

EAS lead system

For maximal clinical impact, an electrode setup considered for ambulatory ECG monitoring requires careful balancing between patient comfort and both accuracy and completeness of the measurement setup. In vastly under-diagnosed atrial fibrillation monitoring, for example, non-invasive ambulatory electrocardiographic patch devices have been claimed superior to conventional

Holter monitors chiefly due to unobtrusive and user-friendly designs that have led to longer study periods and higher study completion rates [6]. Typically, these sorts of patch devices are measuring a single bipolar lead with a short intra-electrode distance (IED) [6], and thus are dependent on the careful placement of the device, as the prominence of atrial and/or ventricular activity in such a lead is highly dependent on the positioning of the device [7-9]. Nevertheless, the benefits of bandage type devices – including ease of use, little intrusion to daily activities, staying hygienic and resistant to water – are significant in the user's point of view to the extent of overweighting the shortcomings and having better clinical yield [6].

We consider that many of the said beneficial aspects can be translated into multichannel realm in the proposed printed and stretchable skin-mounted system that essentially bridges the gap between traditional Holter monitors and recent patch type devices. For arrhythmia monitoring purposes, we expect that a multi-channel device could offer potential for more accurate localization of the problems, better analysis of conduction disorders, and better power especially in differential diagnosis. Due to moderately longer IED and multiple channels, the system as a whole can be less susceptible to variations in the electrode placement in the sense of diagnostic power, and offer much more potential for e.g. ischemic event detection. Ambulatory ischemic event monitoring from ECG has been shown capable of identifying high risk patient subsets, and evidence exists for improved outcomes after detection and treatment of asymptomatic ischemia [10]. What is more, monitoring of ST-segment changes can be used to monitor the response to treatment in acute MI (AMI) patients [10].

Any lead system is faced with the de-facto main diagnostic tool status that the standard 12-lead system has, as the vast body of scientific literature includes decades of work on the standard 12-lead system, its modifications and individual leads. In line with this fact, the EAS electrode setup is a subset of an extensively studied EASI lead system introduced by Dower et al [5]. Typically, the full EASI setup is used in derived lead systems which synthesize the standard 12-lead ECG channels from the measured EASI leads to conform to its aforementioned de-facto status. Moreover, the EASI-synthesized standard leads have been shown in e.g. [11-14] to offer similar diagnostic quality compared to the standard lead system, and also to have similar potential in the synthesis of leads optimized for coronary artery specific acute myocardial ischemia detection [15], for instance. Compared to the full EASI system, the reduced EAS setup is expected to retain a significant part of the diagnostic information and have potential for lead reconstruction as research exists on the individual bipolar leads (ES, AS, and AE) of the EAS system. It should be noted that only two of these are independent, and any one of them can be expressed as a linear combination of the two other leads.

The ES lead – also known as the Barker lead [16] and the vertical sternal lead – is very close to the CM2 (CM-V2) lead often used in Holter devices the difference being

in the location of the E electrode that is placed right to the standard V2 position instead of the lower part of sternum. According to [17], the ES lead exhibits larger P-wave area than the Lewis [18] lead and many non-standard bipolar leads used in Holter monitoring. A study [19] on a modification of the Lewis lead showed that in the ES lead the atrial signal amplitudes are at a similar level to the modified Lewis lead specifically developed for atrial monitoring. It should be noted that the modified Lewis lead differs from the ES lead only in the placement of the E electrode, as in the former it is placed at the fifth intercostal space to right of the xiphoid process. Additionally, the study showed that the ES lead has a similar susceptibility to baseline wander, a slightly increased susceptibility to electromyographic (EMG) noise, and higher ventricular activity amplitudes compared to the modified Lewis lead. Another recent atrial lead study [20] concluded that whilst their proposed "P-lead" provides the best P-wave signal strength, the modified Lewis lead and ES lead have an improved RMS-ratio of P-wave to the QRS-complex and T-wave. Their P-lead is measured bipolarly between electrodes at sternal clavicular junction and the midpoint of the left costal margin in-line with the seventh intercostal space. Therefore, the ES lead presents a midway compromise between the strength of the atrial activity, and the ratio of that with respect to the strength of the ventricular activity. Additional benefits include the central location of the E and S electrodes at easily identified anatomical sites on the chest separated from moving body parts and large muscle groups.

The AS lead, also known as the CM5, CM-V5 or "bipolar V5" lead, is routinely used in Holter monitoring, exercise testing and operation theaters. The AHA Exercise Standards for Testing and Training [21] recommend it as a useful lead not present in the standard lead set. It has been shown to provide high sensitivity for the detection of exercise-induced ischemia, and recommended as the most useful first lead in an ambulatory system with bipolar leads [22, 23]. It should be noted, however, that the ST level in AS lead has been found sensitive to infarcts in lateral aspects whereas septal and inferior infarcts can be partly missed, and a transthoracic lead can perform better [23, 24]. For practical purposes, however, adhesive electrodes placed on the back are not very user-friendly in ambulatory monitoring and can present signal quality challenges also in bedside monitoring while lying on the electrode. Together, the EAS combination of ES and AS leads should provide good potential for myocardial ischemia analysis since the leads CM2 (close to ES) and AS have been shown to overall have high diagnostic yield in the detection of ischemic ST segment changes [25].

Methods

The monitoring system

The skin-mounted ECG monitoring system consists of four printed electrodes and printed conductors which are

then connected to a measurement electronics module. The data is transmitted via Bluetooth Low Energy to a mobile gadget and a cloud service. Finally, medical personnel can go through the data and give the feedback to the patient. The overall system level description can be seen in **Figure 1**.
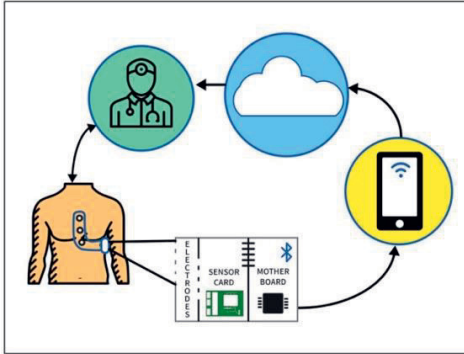
Figure 1. System level description of the ECG monitoring device, data transmission and services.

ECG measurement electronics module

The electronics module consists of two units, a digital unit and an analog unit. The digital unit houses the processing, power and wireless connectivity modules of the device. A cortex ARM M4F microcontroller TZ1001 clocked at 48 MHz from Toshiba Semiconductors is used in the design. The microcontroller also incorporates a Bluetooth Low Energy version 4.0 radio for wireless connectivity. A power management chip (PMIC), TPS65720 from Texas Instruments provides stable 3.3 V and 1.8 V regulated supplies. These supplies are made available in the half-moon edge connector for supplying power to the analog unit. In addition, the PMIC also houses a Li-Po battery charger, with the maximum charge current set to 100 mA. An external reset monitor, TCM810 from Texas Instruments, makes sure that the battery voltage does not fall below 3 V, by shutting off the battery line to the PMIC, in case battery voltage drops below the threshold. A 3 V voltage reference chip REF3330AID delivers a stable reference voltage for the ADCs. Three sets of half-moon edge connectors are provided around the motherboard to provide the necessary analog, digital and power lines to the sensor board. This includes ADC lines, JTAG programming lines, serial communication lines, GPIOs and 3.3 V & 1.8 V power lines. The micro-controller has a four channel 12-bit SAR ADC and a three channel 24-bit Sigma-Delta ADC. The 12-bit ADC can be configured in both differential and single ended modes. The 12-bit ADC configured in single-ended mode is used in the device. A basic block diagram representation of the digital unit is shown in **Figure 2**.

TZ1001 also includes a 3D accelerometer, which can be used to estimate the posture and state of motion of the person being monitored.
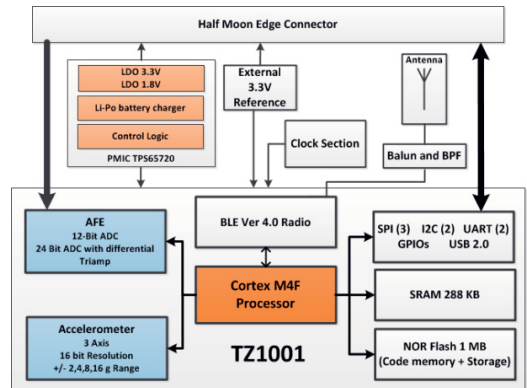
Figure 2. A basic block diagram representation of the digital unit.

The signal conditioning in three ECG channels is realized with identical single stage amplifier connections using INA333 instrumentation amplifier. The inverting inputs of each amplifier are connected to a common reference electrode. An RC high-pass filter in front of the amplifier takes care that high enough gain (i.e.123 in our case) can be set without a risk of saturating the amplifier by a possible DC-offset produced in the electrodes. The analog high-pass and low-pass cut-off frequencies have been set to 0.28 and 106 Hz, respectively. Electrical safety is ensured by limiting the patient auxiliary current in case of a single fault condition to 21 µA with the resistors in the amplifier input. The amplifier and other electronics of the device are protected against ESD with zener diodes. **Figure 3** shows the schematic of a single ECG amplifier section.
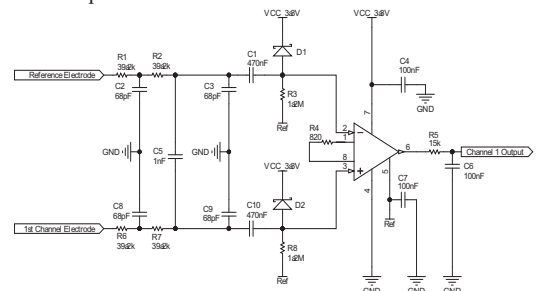
Figure 3. Schematic diagram of the amplifier connection of one ECG channel.

The input referred RMS quantization noise of the ADC alone is 1.7 µV, which is caused by the quantization step of 6.2 µV. The total RMS noise of the electronics (including quantization noise) was measured to be 3 µV when referred to the amplifier input.

The average current consumption of the entire electronics was measured to be 5.8 mA when transmitting the signals of the three ECG channels with 250 Hz sampling frequency. With the nominal battery capacity of

220 mAh, the estimated operation time of the ECG monitor approaches 38 hours.

Mobile app and cloud

In this section we briefly describe the Bluetooth communication between the ECG bandage and a mobile device, then we focus on how the data is stored and viewed on the mobile device and last we come to the cloud service and how the data is transferred and stored there.

The mobile application, developed for the Android platform, was designed to enable a mobile device to acquire ECG data from the ECG bandage via Bluetooth low energy (BLE), graphically display the ECG data, record the data, and send them to the cloud for storage and further analyses. To receive ECG data from the sensor patch, the mobile application first initiates and establishes a connection between the mobile device and the sensor patch and then registers for notification so that ECG data could be transferred from the sensor to the mobile device as notifications at some set intervals. Data transfer continues as long as both devices are connected. Here, the data transfer is done using a custom BLE service developed by Nordic Semiconductors, Nordic UART Service, which emulates UART/Serial port over BLE. This BLE service was used here because of the flexibility it offers for this research and development. Mobile application can read data from multiple sensors on each BLE connection and as well from multiple BLE connections simultaneously. This allows the application to act as a central unit for a complete body area network formed by multiple sensor devices that are each carrying out multiple measurements.

The mobile application decodes the ECG data packets received from the sensor patch to retrieve the ECG samples, and then displays them graphically using a commonly used open source Android charting library called AchartEngine. It also provides the user an option to locally record some of the data for up to ten minutes and storing them on the mobile device for later reference. The recorded data are stored in a json file, one separate file per record, together with some metadata needed for further processing and analyses like the recording time, the sequence numbers of the packets and the name or identification number of the sensor patch from which the data were received. The stored data could then be forwarded to the cloud via HTTP for storage, further processing and analyses. HTTP is used at this stage of development because security is not yet a concern. A secure protocol, HTTPS, would be used later in the development.

The cloud service is intended to store ECG data and other related data such as the time the data were acquired, patients' basic information related to the data, the identification numbers of the sensor patches, etc. It is also intended to perform some analysis on the ECG data and store the result to be viewed and interpreted by qualified medical practitioners.

The cloud service was implemented using Node.js on the server side and Angular.js at the client side. A NoSQL database, MongoDB, was used for the database implementation. The server and the client codes belong to a single application hosted on the Amazon Elastic Compute Cloud (EC2) and the database is hosted on MLab. The key interest here is to learn more about the suitability of these technologies for this task. In its current state, the cloud service only stores ECG data along with other related data and some patients' basic information. It also displays the stored ECG data graphically. The analysis feature and the GUI to view the results of the analysis are yet to be implemented. The analysis software will be running on a server of its own and will have an API that allows the storage cloud service to connect to it. During this research we will study the suitability and scalability of these technologies for use cases that store continuous measurement data.

Fabrication of electrodes

Silver electrodes and the circuitry were screen printed using TIC SCF-300 screen printer and CI-4040 stretchable Ag/AgCl ink (ECM). The silver ink contains 40 – 50 wt% silver powder and 5 – 15 wt% silver chloride powder diluted in a diethylene glycol ethyl ether acetate solvent. The printed pattern was defined by a polyester screen with a mesh count of 79 threads cm^{-1}, a mesh opening of 69 μm, and a stretching angle of 22.5°. Printing was done on a 50-μm-thick Platilon thermoplastic polymer substrate (Covestro). After printing, the silver pattern was annealed in a convection oven at 130 °C for 30 minutes.

The print, with polyurethane substrate, was heat laminated with Opsite Flexifix transparent polyurethane film. Opsite film has an acrylic adhesive layer underneath a polyurethane layer and this adhesive layer is used to attach the bandage to the skin. One additional polyurethane (50 μm Platilon) layer is laminated on top of the Opsite and print layers.
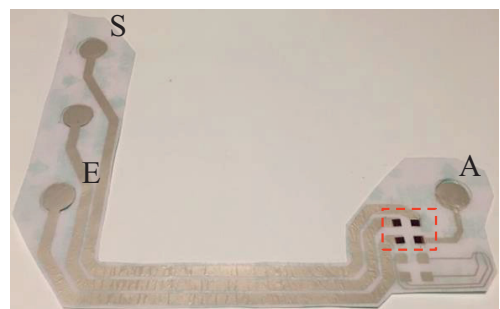
Figure 4. Printed electrodes laminated with an adhesive film. Connections for the electronics module are marked with a red dashed rectangle.

Figure 4 presents the printed electrodes without the electronics module. Anisotropic conductive tape (ACA) is used to attach the electronics to the bandage both electrically and mechanically. ACA provides electrical contacts from four electrodes via four 5 mm x 5 mm

contact areas (marked with a red dashed rectangle in **Figure 4**).

Copper tape was used to provide the electrical contact from the print on top of the bandage structure, so that the electronics module can be attached to the bandage. To improve the electrode skin interface a 0.89-mm-thick sensing gel circles were used between the skin and the electrodes.

Test measurements

Testing of the developed ECG monitoring system and the printed electrodes were done for one male volunteer who had no diagnosed heart related problems. Body hair was removed, skin was wiped with disinfectant and dead skin cells were scraped off with a rough sponge around the electrode areas prior to the measurements. **Figure 5** presents the monitoring system and the printed electrodes secured in place for the measurements.
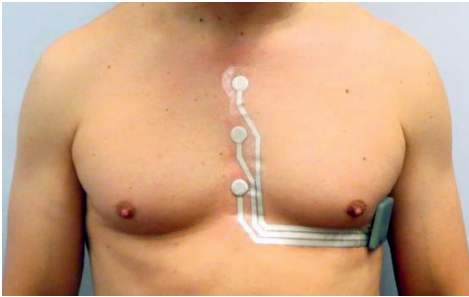
***Figure 5**. Monitoring system and printed electrode placement.*

The measurements were done in three conditions: while lying, while sitting and during walking. Each of the phases were 2 minutes long and consequently the overall measurement time was 6 minutes.

Results and Discussion

Figure 6 shows five second extracts of the ECG signal from the three measurement conditions. While the measurement device uses single-ended configuration and measures the potentials of E-, A-, and S-electrodes with respect to a common reference electrode located between the E- and S-electrodes, the signals are converted to A-E, A-S, and E-S measurement leads by adding or subtracting them. The raw ECG signals of the three leads are presented with a different color. The red line (top) is the A-E lead signal, the blue line (middle) is measured between the A-S electrodes and yellow (bottom) signal is from the E-S lead. The signal plots show excellent signal-to-noise ratio even without any preprocessing thus allowing for detailed analysis of ECG morphology.

Conclusions

This paper presented a printed, skin-mounted hybrid ECG measurement system for continuous ECG monitoring. The system consists of printed electrodes, which are printed onto stretchable substrate with stretchable Ag/AgCl ink, a rigid electronics module, and a mobile user interface device. The print is laminated onto an adhesive film which is used to attach the electrodes to the skin. The electronics module is secured in place on top of the electrode bandage using conductive tape. This enables the removing of the reusable electronics part while the printed bandage is being disposed. The data from the ECG device is transmitted wirelessly via Bluetooth Low Energy to a mobile device where the data is visualized and sent further to cloud.

The performance of the device was demonstrated with measurements where a male subject wore the ECG bandage and was lying down, sitting and walking for 2 minutes per activity. The resulting signal quality is sufficient for detailed ECG analysis.
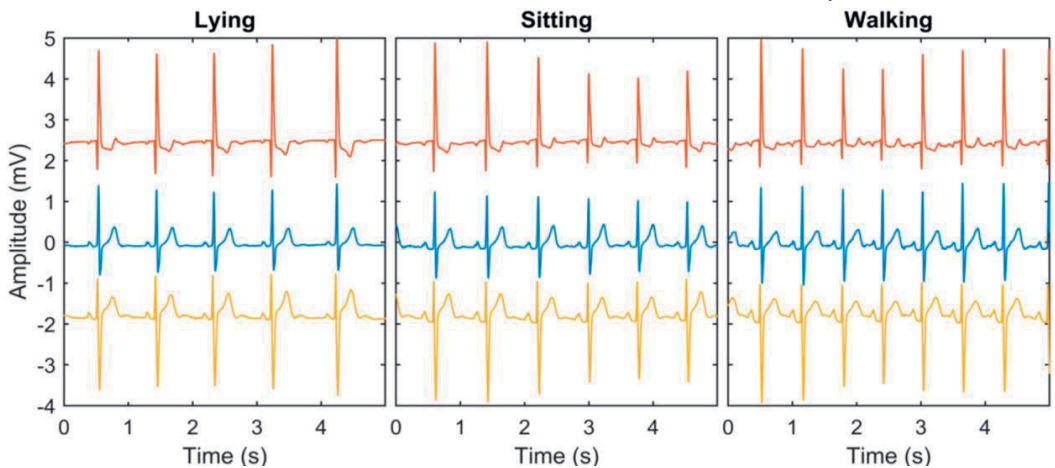
***Figure 6.** Recorded ECG signal when the subject was lying down for 2 minutes, sitting for 2 minutes and walking for 2 minutes. Red: A-E lead signal, blue: A-S lead signal and yellow: E-S lead signal.*

References

1. Sillanpää, H. et al. "Integration of inkjet and RF SoC technologies to fabricate wireless physiological monitoring system." *In Proc. of Electronic System and Technology Conference (ESTC)*, Helsinki, Finland, Sept. 16-18, (2014).

2. G. Yang et al. "Bio-Patch Design and Implementation Based on a Low-Power System-on-Chip and Paper-Based Inkjet Printing Technology." *IEEE Transactions on Information Technology in Biomedicine* Vol. 16 (2012), pp. 1043-1050.

3. Yeo, W. et al. "Multifunctional Epidermal Electronics Printed Directly Onto the Skin." *Advanced Materials,* Vol. 25, (2013), pp. 2773-2778.

4. Honda, W., Harada, S., Arie, T., Akita, S. & Takei, K. "Wearable, Human-Interactive, Health-Monitoring, Wireless Devices Fabricated by Macroscale Printing Techniques." *Advanced Functional Materials* Vol. 24, (2014), pp. 3299-3304.

5. Dower, G.E., et al., "Deriving the 12-lead electrocardiogram from four (EASI) electrodes." *Journal of Electrocardiology* 21 (1988), pp. S182-7.

6. Fung, E., et al. "Electrocardiographic Patch Devices and Contemporary Wireless Cardiac Monitoring." Frontiers in Physiology. Vol. 6, No. 149 (2005).

7. Nedios, S., et al. "Precordial electrode placement for optimal ECG monitoring: Implications for ambulatory monitor devices and event recorders." *Journal of Electrocardiology*, Vol. 47, No. 5 (2014), pp. 669-676.

8. Puurtinen, M., et al. "Best Electrode Locations for a Small Bipolar ECG Device: Signal Strength Analysis of Clinical Data." *Annals of Biomedical Engineering*, Vol. 37, No. 2 (2009), pp 331-336.

9. Ki Moo Lim, et al. "Patient-Specific Identification of Optimal Ubiquitous Electrocardiogram (U-ECG) Placement Using a Three-Dimensional Model of Cardiac Electrophysiology." *Biomedical Engineering, IEEE Transactions on*, vol. 60, No. 1 (2013), pp. 245-249.

10. Wimmer, N.J., et al. "The Clinical Significance of Continuous ECG (ambulatory ECG or Holter) Monitoring of the ST-Segment to Evaluate Ischemia: A Review." *Progress in cardiovascular diseases*, Vol. 56, No. 2 (2013), pp. 195–202.

11. Wehr, G., et al. "A vector-based, 5-electrode, 12-lead monitoring ECG (EASI) is equivalent to conventional 12-lead ECG for diagnosis of acute coronary syndromes." *J Electrocardiol,* Vol. 39, No. 1. (2006), pp. 22-8.

12. Martínez, J.P. et al., "Assessment of QT-measurement accuracy using the 12-lead electrocardiogram derived from EASI leads." *J Electrocardiol.*, Vol. 40, No. 2 (2007), pp. 172-9.

13. Chantad, D., et al. "Derived 12-lead electrocardiogram in the assessment of ST-segment deviation and cardiac rhythm." *J Electrocardiol.* Vol. 39, No. 1 (2006), pp. 7-12.

14. Horácek, B.M., et al. "Diagnostic accuracy of derived versus standard 12-lead electrocardiograms." *J Electrocardiol*, Vol. 33 (2000), pp. suppl:155-60.

15. Horácek, B.M., et al. "Optimal electrocardiographic leads for detecting acute myocardial ischemia." *J Electrocardiol.*, Vol. 34 (2001), pp. suppl:97-111.

16. Barker, P.S., et al. "Auricular paroxysmal tachycardia with auriculoventricular block." *Am Heart J*, Vol. 25 (1943), pp. 765–798.

17. Herzog, L.D. R., et al. "Evaluation of Electrocardiographic Leads for Detection of Atrial Activity (P Wave) in Ambulatory EGG Monitoring: A Pilot Study." *Pacing and Clinical Electrophysiology*, Vol. 15, No. 2 (1992), 131-134.

18. Lewis T. "Auricular fibrillation. In: Clinical Electrocardiography." 5th ed. London, UK: Shaw and Sons; 1931:92.

19. Petrėnas, A., et al. "A modified Lewis ECG lead system for ambulatory monitoring of atrial arrhythmias." *Journal of Electrocardiology*, Vol. 48, No. 2 (2015), pp. 157-163.

20. Kennedy, A., et al., "Detecting the Elusive P-Wave: A New ECG Lead to Improve the Recording of Atrial Activity." In Biomedical Engineering, IEEE Transactions on, Vol. 63, No. 2 (2016), pp. 243-249.

21. Fletcher, G. F. et al. "Exercise Standards for Testing and Training: A Scientific Statement From the American Heart Association." *Circulation,* Vol. 128 (2013), pp. 873-934.

22. Puurtinen, M., et al. "Value of leads V4R and CM5 in the detection of coronary artery disease during exercise electrocardiographic test." *Clinical Physiology and Functional Imaging*, Vol. 30, No. 4 (2010), pp. 308-312.

23. Quyyumi A.A., et al. "Value of the bipolar lead CM5 in electrocardiography." *Br Heart J*, Vol. 56 (1986), pp. 372–376.

24. Jespersen, C. M., et al. "Detection of myocardial ischaemia by transthoracic leads in ambulatory electrocardiographic monitoring." *Br Heart J*, Vol. 68 (1992), pp. 286-290.

25. Shandling, A.H., et al. "Efficacy of three-channel ambulatory electrocardiographic monitoring for the detection of myocardial ischemia." *Am Heart J,* Vol. 123, No. 2 (1992), pp. 310-6.

PUBLICATION
III

Validation of Printed, Skin-Mounted Multilead Electrode for ECG Measurements

Vuorinen T., Noponen K., Vehkaoja A., Onnia T., Laakso E., Leppänen S., Mansikkamäki K., Seppänen T., and Mäntysalo M.

Validation of Printed, Skin-Mounted Multilead Electrode for ECG Measurements

Tiina Vuorinen,* Kai Noponen, Antti Vehkaoja, Timo Onnia, Eeva Laakso, Susanna Leppänen, Kirsi Mansikkamäki, Tapio Seppänen, and Matti Mäntysalo

An electrocardiography (ECG) monitoring can be used to detect heart-related abnormalities by recording cardiac activity over a period of time. The conventional 12-lead ECG measurement system is the standard practice for the evaluation of the heart's electrical activity. However, a recent trend is to develop patch-type measurement devices for unobtrusive ECG monitoring by reducing device size and number of electrodes on the skin. This development aims to minimize the discomfort for the user from the wearable recording devices. A printed, bandage-type hybrid system for continuous ECG monitoring to allow as much comfort as possible while maintaining the signal quality required for medical evaluation is proposed. Movement artifacts in recorded ECG signals are a challenge in long-term monitoring while the patients are engaged in their everyday activities. The movement artifacts from the printed skin-conformable electrode are compared to commercial exercise stress-test ECG electrodes during different physical activities and stationary periods. The results show that the signal quality obtained with the multilead patch ECG electrode, manufactured with printing technologies, is comparable to electrodes currently used in healthcare.

1. Introduction

World Health Organization (WHO) estimates that 17.9 million persons died as a result of cardiovascular diseases in 2016 (31% of all global deaths).[1] New healthcare solutions are needed

to intervene this global issue. Wearable devices and telehealth are enabling a formation of a new segment among healthcare technologies. These medical devices could provide continuous monitoring of risk patients, early symptom detection, and reduced healthcare costs.[2] Continuous monitoring is required especially in cardiac healthcare because the cardiovascular disease symptoms may occur at any time of the day. For that reason, different monitoring systems have been developed to detect the cardiac events, and the occurred symptoms define the right monitoring type. Ambulatory electrocardiographic (Holter) monitoring is one option and it is the clinical standard of care for detecting cardiac events. A Holter monitor is a portable measurement device with wire-connected electrodes. Electrodes are attached to the patient's skin to record the low-level electrical potentials originating from the de- and repolarization of the cardiac muscle, during every heartbeat, and are transferred to the body surface by the volume conductor formed by the body tissues. This type of monitoring systems can provide useful information about the function of the heart from diagnostic and prognostic point of view. Nevertheless, they lack the comfort important for people who would benefit from wearing the monitoring devices for extended periods of time.[3,4]

Due to this, the transition from bulky, wire-connected devices to wearable patch type devices is a fast-developing research field.[5–7] This enables the development of totally new types of structures, called epidermal electronics. Epidermal electronics refers to stretchable electronic systems in which the mechanical properties of the device align with the human skin, and the whole system is so lightweight and thin that it integrates seamlessly with the epidermis.[8] Due to these properties stretchable electronic systems overcome the mechanical mismatch and are therefore more comfortable to use even for prolonged device wearing time.[4,9,10] Epidermal electronics provides novel structures for imperceptible measurements of skin movements and different biological signals such as temperature, skin hydration, microvascular blood flow, electromyography (EMG), and biochemical and cardiac signals.[4,11–17]

Several types of epidermal electronic systems have been developed to record ECG signals. Lee et al. have developed an ECG and heart rate logging wearable sensor referred as

T. Vuorinen, T. Onnia, Prof. M. Mäntysalo
Faculty of Information Technology and Communication Sciences
Tampere University
Tampere 33720, Finland
E-mail: tiina.vuorinen@tuni.fi

K. Noponen, Prof. T. Seppänen
Center for Machine Vision and Signal Analysis
University of Oulu
Oulu 90014, Finland

Prof. A. Vehkaoja
Faculty of Medicine and Health Technology
Tampere University
Tampere 33720, Finland

E. Laakso, S. Leppänen, K. Mansikkamäki
Biomedical Laboratory Science
Tampere University of Applied Sciences
Tampere 33520, Finland

(iD) The ORCID identification number(s) for the author(s) of this article can be found under https://doi.org/10.1002/admt.201900246.

**ADVANCED
SCIENCE NEWS**
www.advancedsciencenews.com

**ADVANCED
MATERIALS
TECHNOLOGIES**
www.advmattechnol.de
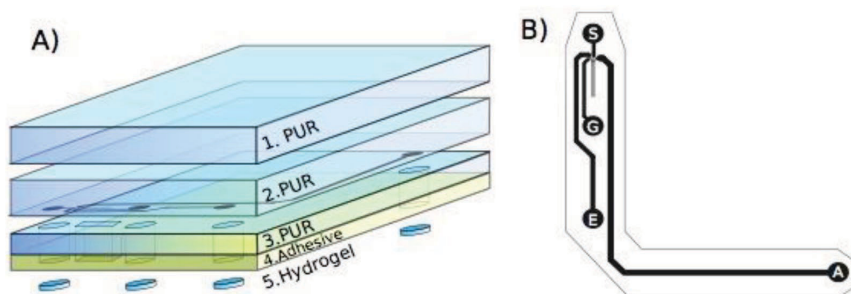
Figure 1. A) Multilayer bandage structure. The layer 1 is 50-µm-thick thermoplastic polyurethane (TPU) film, the layer 2 is 50-µm-thick polyurethane (TPU) with screen-printed silver conductors, the layer 3 is polyurethane film, and the layer 4 is an acrylic adhesive. Number 5 are hydrogel pieces. B) Illustration of the final bandage layout when it is cut out from the larger area substrate.

"WiSP." The device is low cost, lightweight (1.2 g and 58 mm × 25 mm × 1 mm), and capable of energy harvesting and capturing one ECG lead at a time (lead I, II, or III).[10] Nawrocki et al. fabricated and tested an ultrathin (sub-300 nm) biopotential electrodes claiming them to be low-noise and motion artifactless. The electrodes were tested by wearing them on the arm and by vibrating the skin with an electromechanical vibrator.[18] Dong et al. presented a stretchable biopotential electrode for long-term ECG signal recordings and the device was tested with one male volunteer.[19] Temperature sensor together with gel-less sticky ECG sensor was developed by Yamamoto et al. The ECG sensor was tested with one volunteer so that the sensor patch was attached to the volunteer's chest and the patch was wire-connected to measuring devices.[20]

Long-term wearability, stretchability of mechanically different materials, permeability, and physiological differences between users are critical challenges that need to be overcome before epidermal electronics can be used in real-life applications.[10,18,21,22] For example, to minimize the skin irritation of the gel electrodes a lot of research is done to develop gel-free dry electrodes.[23–27] Several studies present new stretchable electrode, sensor, and measurement system designs. Nevertheless, these studies lack the comprehensive tests, with both males and females, where the sensors and the processing unit are placed in the exact place where the measurement would be done in real-life situations. While in most of the earlier studies the developed patch electrodes are made for single-lead ECG measurement and aimed for monitoring cardiac rhythm, more measurement leads observing the heart from several directions are needed. Multiple leads enable more comprehensive view about the cardiac activity and, for example, monitoring the level of ST segment in the ECG and detecting ischemic events.

In this study, we compared a printed, multilead ECG electrode with Ambu Blue Sensor R-00-S electrodes during different physical activities to estimate differences in their vulnerability to motion artifacts. We recruited volunteers with different body types to verify the functioning in variety of people. The subjects performed two identical ≈30 min long tests with a resting period in between them. Both test rounds were done by wearing either printed ECG electrodes or traditional electrodes. Faros 360 (Bittium Biosignals) recording device was used to

record the signals in both cases. Volunteers were both males and females, with different level of physical performance, from age 23 to 50. We have validated the signal quality obtained with printed multilead patch ECG electrode and showed that signal quality, comparable to electrodes currently used in healthcare, can be achieved with compact unobtrusive electrode structure. The long-term wearability (72 h) of the multilead patch is presented in ref. [28].

2. Results and Discussion

Figure 1a presents the structure and the layers of the developed bandage. Layer 1 is 50-µm-thick thermoplastic polymer film. Layer 2 is the same material with screen-printed stretchable silver conductors. Layer 3 is polyurethane film with an acrylic adhesive layer. Cutout holes are made to the layer 3 and layers 1–3 are then heat-laminated together. Finally, round-shaped pieces of hydrogel were attached to the structure to improve the electrical contact with the skin. Figure 1b shows how the bandage is cut to its final shape by removing excess adhesive material around the print. More detailed description of the bandage structure is presented in the Experimental Section.

To analyze similarities and differences of the signals recorded with traditional electrodes and the proposed bandage, a signal quality comparison study was conducted with 29 volunteers (14 females, 15 males) with no diagnosed cardiac problems. In four cases, the subject's data had to be rejected a posteriori due to occurrence of technical problems in the recording leaving a totality of 50 data records, 25 with each electrode type. The most likely cause for the problems was considered to be related to connectivity between the electrode connector and the cabling to the recording device. Participants' characteristics such as age, weight, height, and body mass index are listed in **Table 1**.

Table 1. Participants' characteristics.

	Age [years]	Weight [kg]	Height [cm]	Body mass index
Mean SD	32.2 ± 7.6	70.2 ± 9.5	171.3 ± 9.9	24.0 ± 3.0
Range	23–50	54–93	153–195	19.3–30.0

ADVANCED
SCIENCE NEWS
www.advancedsciencenews.com

ADVANCED
MATERIALS
TECHNOLOGIES
www.advmattechnol.de
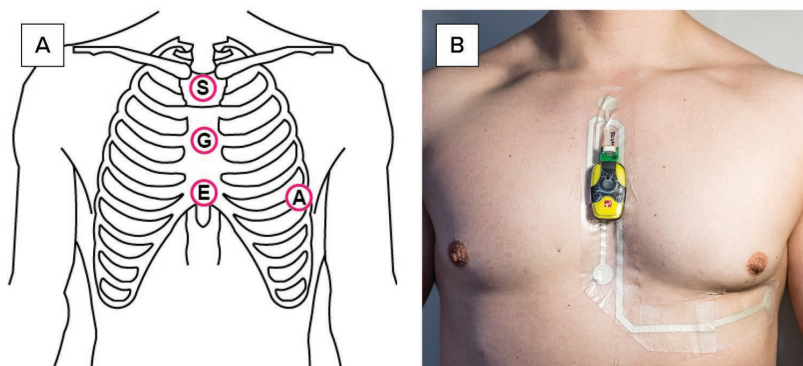
Figure 2. a) Electrode locations in EAS electrode system and b) a picture of a volunteer wearing the bandage and the data collecting device.

As concurrent measurements with the bandage and electrodes from the same electrode locations are not possible, two consecutive incremental exercise tests were made with each subject in a randomized order: one with the bandage and another one with regular electrodes placed at the bandage electrode sites. The measurement protocol included lying still (supine position), standing still, walking/running on a treadmill at increasing speeds, and finally recovering in sitting position. Between the measurements, there was a rest period of 1 h. Although the recordings were not made simultaneously, we can draw conclusions on differences in the average behavior and amounts of variation exhibited in the data at similar heart rate levels.

Figure 2 shows the electrode locations in EAS electrode system based on which the evaluated electrode was developed.[29] The electrode E is located on the lower part of the sternum, A on the standard V5 electrode location of the 12-lead system, and S on the manubrium. The electrode potentials are measured with respect to common reference electrode G and three bipolar leads are formed as potential differences between the electrode sites A, E, and S. Namely, the lead AE

is the voltage $u_{AE} = \phi_A - \phi_E$, AS is $u_{AS} = \phi_A - \phi_S$, and ES is $u_{ES} = \phi_E - \phi_S$, where ϕ_X denotes the electrical potential at the site X. It should be noted that there are only two independent leads in this set, and, for example, the lead ES is linearly dependent on the two other leads $u_{ES} = u_{AS} - u_{AE}$. Figure 2b presents the monitoring system and the printed electrodes secured in place for the measurements.

Figure 3 depicts the beat-to-beat variation of the ECG of one randomly selected subject in the AS lead of the EAS electrode configuration. The beat-to-beat variations in the AE and ES leads are shown in Figures S2 and S3 (Supporting Information). Superimposed heartbeat cycles with the characteristic P-waves, QRS complexes, and T-waves following each other are observed in Figure 3. The signals measured with the bandage are shown on the left, and those with the regular electrodes on the right. From top to down, the signals have been further grouped together according to the exercise test protocol phases of lying still (supine position), standing, walking, brisk walking, and running that represent the increasing work load portion of the test. In each phase, heart rate between the two measurements is similar, and the heart rate does not vary very much
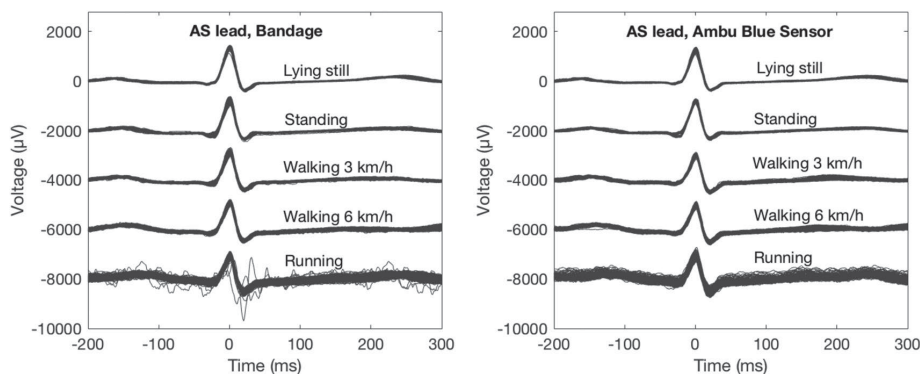
Figure 3. Superimposed beats in AS lead measured with the bandage (left) and ordinary electrodes (right) during lying still, standing, walking (3 km h^{-1}), brisk walking (6 km h^{-1}), and running (10 km h^{-1}). Each incremental activity level is biased by −2 mV from top to bottom to show the expected increasing beat-to-beat variability of the signals (Volunteer number 24).

**ADVANCED
SCIENCE NEWS**
www.advancedsciencenews.com

**ADVANCED
MATERIALS
TECHNOLOGIES**
www.advmattechnol.de
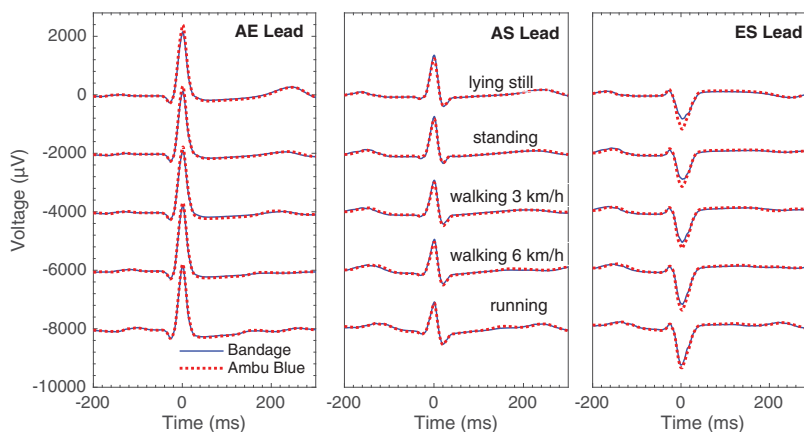
Figure 4. Mean beats in AE, AS, and ES leads measured with the bandage (solid line) and ordinary electrodes (dotted line) during lying still, standing, walking (3 km h^{-1}), brisk walking (6 km h^{-1}), and running (10 km h^{-1}). Each incremental activity level is biased by −2 mV from top to bottom (Volunteer number 24).

within a phase leading to rather stable superimposition. Due to the more varied heart rate range, however, the recovery phase (sitting) of the exercise test is not depicted. Regarding the variation seen in the figures, some changes of the QT intervals can be seen caused by the changing heart rate within each phase. In addition, the natural beat-to-beat variation caused, for example, by respiration, movement, and noise can also be seen. Overall, the signals measured with the bandages and the regular electrodes have very similar beat-to-beat variability patterns. Nevertheless, electromyographic noise during the walking phase in the regular electrode measurements seems to have been more abundant in this case (middlemost signals on the right), and the bandage signals seem to include a bit lower frequency variation during running (lowest signals on the left).
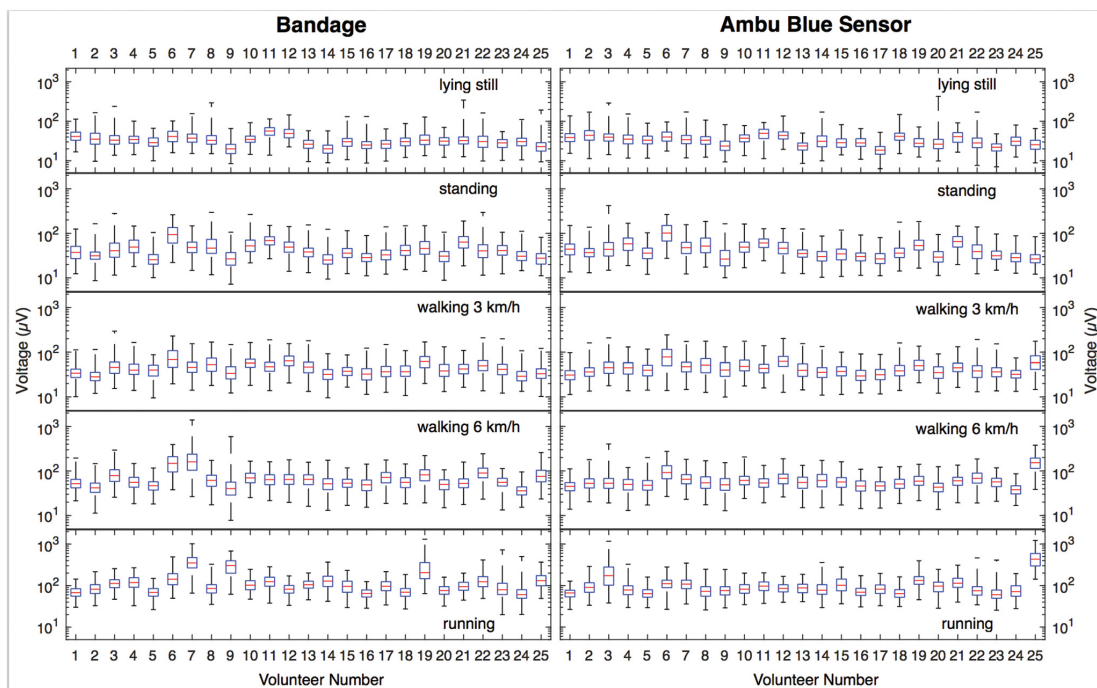
In addition to the similar beat-to-beat variation, the mean shape of the signals measured with the bandage and the regular electrodes look similar. This is more clearly depicted in **Figure 4** that shows the average heartbeat waveform in each of the leads and test phases for the same subject. The remaining levels of discrepancy, for example, at the R-peak amplitudes are explained mostly by minute differences in electrode positioning, heart rate, respiration, and movements between the two measurements.

In the previous figures, we have shown examples of data of one subject. To better summarize the beat-to-beat variability of the signals of all the subjects, we calculated how much variation there is with respect to the average shape of the QRS complex. More precisely, we subtracted the mean beats (Figure 4) from the individual beats (Figure 3, Figures S2 and S3, Supporting Information), and calculated the amount of residual variation using the root-mean-square formula within a fixed time windows of 50 ms around the R-peak. **Figure 5** shows the boxplot of the deviations in the AS lead. Deviations in AE and ES are shown in Figures S4 and S5 (Supporting Information), respectively. Again, the results of the bandage measurements are illustrated on the left, and the ones obtained with regular electrodes on the right; and the measurement phases group

the data from top to bottom in increasing work load order. The distribution of the beat-to-beat deviations of each subject is presented with a box with whiskers. Within each box, the horizontal line mark indicates the median, and the bottom and top edges of the box indicate the lower and upper quartiles, respectively. The whiskers show the smallest and largest deviations.

Generally, the deviations between the two measurements (left vs right) are similar, but the distribution is highly dependent on the subject. Especially, the median RMS deviations of the bandage and regular electrode measurements seem very similar, the mean absolute difference between them being 16.5, 22.3, and 29.3 µV, in the leads AS, AE, and ES, respectively, averaged across all the phases. This is further summarized in **Figure 6** that collects the median discrepancies of each subject. There are some cases in which subject's median beat-to-beat deviations in a certain exercise phase differ between the bandage and the electrodes, which is seen as a departure from the diagonal line. Although overall these deviations seem to be rather small and occur randomly in favor of the bandage or the regular electrodes, for example, due to some electromyographic artifact occurring in one test but not the other one, there is a slight tendency for this to happen mostly in the running phase with notably larger median deviations for the bandage for about half of the subjects. Mostly, this is explained by the somewhat larger low-frequency baseline wander of the bandage signals during intensive exercise such as running, similar to what is seen in Figure 3, Figures S2 and S3 (Supporting Information, left bottom).

Table 2 lists the corresponding Pearson correlation coefficients (*r*) of the median variabilities shown in Figure 6 to further quantify the aforementioned behavior. The correlation is strong when lying still, and very strong when standing, in all the leads. During normal and brisk walking, the correlation is strong in the AS and ES leads, but only moderate in the AE lead. The correlation is lowest being moderate in the AS and ES leads, and weak in the AE lead during running. Overall, the

ADVANCED
SCIENCE NEWS

www.advancedsciencenews.com

ADVANCED
MATERIALS
TECHNOLOGIES

www.advmattechnol.de

Figure 5. RMS [µV] beat-to-beat variability of the QRS complex in the AS lead compared to the mean complex with the bandage (left) and ordinary electrodes (right) during lying still, standing, walking (3 km h⁻¹), brisk walking (6 km h⁻¹), and running (10 km h⁻¹) in all the subjects. The QRS complexes are selected with a fixed ±50 ms window around the R-peak.

correlation in the AS and ES leads is strong and moderate in the AE lead, across all the phases. Stronger correlation arises from clear interindividual differences in the beat-to-beat variability that are similarly represented in the intraindividual electrode and bandage measurements. Despite the overall slight tendency of decreasing correlation with increasing level of activity, the correlation is most notably weakened due to the few

distinct outlier cases especially in the AS lead during running and partly brisk walking.

Finally, we also considered the amount of discrepancy of the mean beats (Figure 4) of all the subjects in clinical terms by extracting a portion of the ST segment, and measuring the RMS error between the mean bandage and the mean regular electrode beat in each of the leads. For the purposes of this
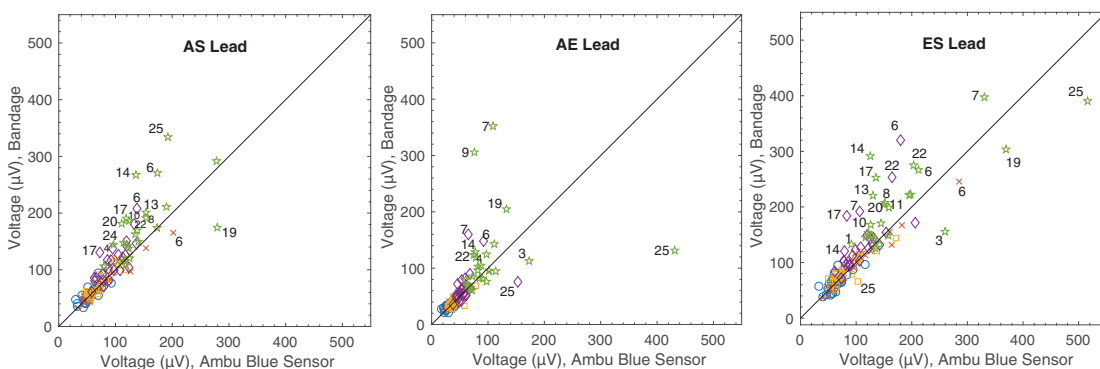
Figure 6. Scatter plot comparison of median RMS [µV] beat-to-beat variabilities of the QRS waves in electrodes and bandages in all three channels AS, AE, and ES during lying still (circle o), standing (cross x), walking 3 km h⁻¹ (square □), brisk walking 6 km h⁻¹ (diamond ◇), and running 10 km h⁻¹ (star ☆). Subject numbers for median RMS deviations of over 35 µV are annotated.

**ADVANCED
SCIENCE NEWS**
www.advancedsciencenews.com

**ADVANCED
MATERIALS
TECHNOLOGIES**
www.advmattechnol.de

Table 2. Correlations of the median RMS beat-to-beat variabilities of QRS waves between the electrode and bandage leads.

Phase	AS lead	AE lead	ES lead
Lying still	0.78	0.76	0.78
Standing	0.97	0.95	0.99
Walking	0.90	0.76	0.88
Brisk walking	0.79	0.41	0.71
Running	0.52	0.13	0.41
All combined	0.74	0.52	0.67

study, the relevant ST segment portion was defined to be the interval from 60 to 100 ms following the magnitude signal R-peak to capture relevant differences.
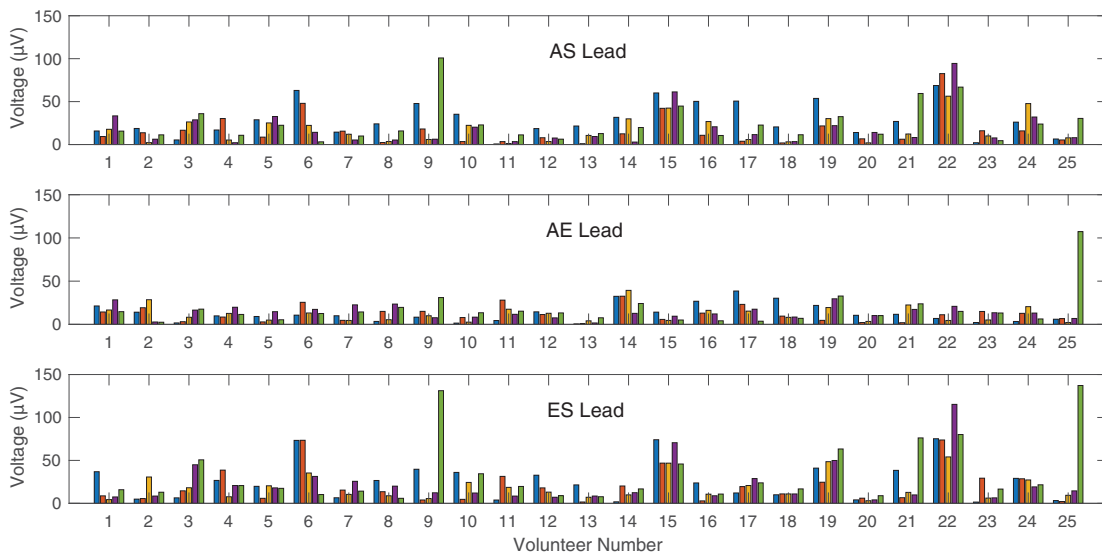
Figure 7 shows the RMS differences of the ST segment portions of the mean beats. Current clinical guidelines for traditional 8/12-lead ECG (at rest) consider new ST elevations or depressions at the J point in at least two contiguous leads larger than 100–200 µV—the exact threshold depending on the leads considered and subject's gender—to signify an ST-elevation myocardial infarction.[30] In most cases, the observed differences in Figure 7 are well below 50 µV with some notable exceptions. In the case of subject 22, for instance, the heart rate during the regular electrode measurements has been higher throughout most of the exercise protocol causing changes in the observed mean shape morphology. In this case, the recovery period between the tests may have not been long enough. The same is true for subject 15 but in this case, there has also been sizeable low-frequency noise in the bandage signal starting already at the walking speed instead of the tendency

of it to occur at a higher exercise intensity. For subject 25, the traditional electrode in S location exhibits movement artifact and contact issues during running phase which affects both AS and ES leads. Similar issue is encountered with subject 9 in which case the bandage E electrode shows contact problems. It is also worth noting that in cases such as subjects 6, 9, 16, 17, and 19 somewhat high ST-level differences are observed during the rest phase lying supine but the discrepancy is diminishing with the increasing intensity.

3. Conclusion

Interindividual variation in, for example, electromyographic noise levels and the amount of movement artifacts were large in both measurement modalities during exercise. However, the overall signal quality is similar to the proposed bandage compared to the traditional electrodes in both average behavior as well as in beat-to-beat variation of the signals intraindividually throughout the exercise modalities. Differences between the mean beat ST levels between the regular electrodes and the bandage were small for most subjects, but a few showed differences during supine rest which diminished toward increasing exercise intensity. This could be related to the characteristics of the persons, such as their anatomy and exact body position during lying pose, as well as physiological status such as cold or warm skin and amount of perspiration.

The bandage seems to be slightly more susceptible to the development of low-frequency noise with a frequency related to the cadence and a power related to the exercise intensity. The noise is likely caused by upper torso soft tissue motion due to

Figure 7. RMS differences in ST segments of the mean beats between bandage and electrodes signals in all three channels AS (top), AE (middle), and ES (bottom). For each of the 25 subjects, the grouped bars show the RMS difference during lying still, standing, walking (3 km h^{-1}), brisk walking (6 km h^{-1}), and running (10 km h^{-1}) from left to right.

ADVANCED
SCIENCE NEWS
www.advancedsciencenews.com

ADVANCED
MATERIALS
TECHNOLOGIES
www.advmattechnol.de

heel strike impacts, upper limb movements, and torso rotations, as the bandage system ties skin tissues on the upper torso together more rigidly than individual electrodes. More comprehensive explanation is presented in the Supporting Information (Figures S6–S9, Supporting Information). Bandage–measurement device interface and the shape of the bandage should be carefully designed to accommodate certain physiological characteristics such as persons with large breasts. More elastic and stretchable construction between the electrode sites could make the whole bandage system less rigid on the skin lessening susceptibility to movement-related low-frequency interference and disturbance.

4. Experimental Section

Printed Electrodes Fabrication: The outline of the fabrication process for the printed bandage is presented in ref. [31]. Printed electrodes and the circuitry were screen printed using TIC SCF-300 screen printer and CI-4040 stretchable Ag/AgCl ink (ECM, USA). The ink contains 40–50 wt% silver powder and 5–15 wt% silver chloride powder diluted in a diethylene glycol ethyl ether acetate solvent. Printing was done on a 50-μm-thick Platilon 4201 AU thermoplastic polymer substrate (Covestro, Germany). Tensile strain at break is 550% and tensile stress at 50% strain is 5–7 MPa and at break 550 MPa for this polyurethane film according to the manufacturer. After printing, the printed pattern was annealed in a convection oven at 130 °C for 30 min.

The print, with the polyurethane substrate, was heat laminated with Opsite Flexifix which is a transparent polyurethane film with an acrylic adhesive layer. The adhesive layer was used to attach the bandage to the skin. One additional 50-μm-thick polyurethane layer was laminated on top of the bandage material and print layers. Round shape pieces of 0.89-mm-thick AG635 sensing gel (Axelgaard Manufacturing Co., Ltd., USA) were used at the electrode–skin interface to form a stable electrical contact. This hydrogel material was designed and formulated specifically for electrocardiogram and electromyogram monitoring applications and according to the measurements the impedance of the bandage is at the acceptable level for ECG measurements.

Signal Quality Testing Protocol: Chest hair was shaved prior to the recordings underneath the bandage location area. Next, the skin was wiped with Desinfectol H (Berner Oy, Finland) disinfectant and dead skin cells were scraped off with Red Dot prep tape (3M). The bandage was then fixed in place and Faros 360 data recording device, configured in unipolar measurement mode, was attached to the bandage with a micro-USB connector. Micro-USB connector contained 100 kΩ series resistors used for high voltage protection. Flexifix adhesive film was used to secure Faros in place and to minimize any mechanical stress to the micro-USB connector. Faros 360 was turned on and the participant was asked to perform the physical activities presented the following activities: lying still in supine position (5 min), standing (5 min), walking 3 km h^{-1} (5 min), walking 6 km h^{-1} (5 min), running 10 km h^{-1} (2 min), and sitting (5 min). After activities the data collection device was switched off, bandage was removed, and the participant had a 1 h rest.

Commercially available Ambu Blue Sensor R-00-S sensors were placed on participants' skin in the beginning of the second measurement using the same electrode locations as with the printed electrode bandage. The data collection device was turned on and the participant performed the previously mentioned physical activities. The data collection device was then switched off, the electrodes were removed, and the test ended. The test arrangement was randomized so that the volunteers started the tests randomly either with the bandage or the Ambu Blue sensors.

ECG signals were measured at the sampling rate of 1000 Hz. As a preprocessing step before further analysis, baseline wandering was reduced by applying a digital 12th order Butterworth filter having 0.67 Hz cutoff frequency in both the forward and reverse directions using the zero-phase method in accordance with clinical guidelines.[32,33] QRS complexes were detected using a simple multilead R-peak detector that operated on the magnitude signal of the a band-pass filtered AS and AE leads, that is, on

$$u_{MAG} = \sqrt{u_{AS}^2 + u_{AE}^2} \tag{1}$$

where u_{AS} and u_{AE} are the band-pass filtered (1–40 Hz) lead signals. In the magnitude signal, the R-peaks were detected as local maxima agreeing to fixed constraints on peak amplitudes and interpeak distances (amplitude 1.3 and 1 mV higher with respect to neighboring peaks; RR interval larger than 270 ms). Results of the QRS detection were also manually validated. Ectopic beats such as premature ventricular contractions (PVCs) were rejected based on abnormal width of the QRS complex. A beat was considered ectopic if it was 20% wider than the median width of all the complexes at half QRS height. Beats containing sudden level changes, for example, due to connector movement were rejected as artifacts (>1 mV/sample). For each exercise test protocol phase, the cardiac cycles were grouped together within the same phase based on the protocol time table leaving 10 s ambiguity/transition regions around the phase changes in both directions. All the nonrejected cycles considered normal were extracted using a fixed window from −200 to 300 ms around the detected magnitude signal R-peak. Finally, it should be noted that the band-pass filtering step was only used for the QRS and ectopic beat detection, and all further analysis is based on the baseline wander reduced signal.

Ethical Statement: This study was accepted by the Ethics Committee of the Tampere Region. All volunteer test subjects were informed on the purpose of the study and informed signed consents were obtained from them.

Supporting Information

Supporting Information is available from the Wiley Online Library or from the author.

Conflict of Interest

The authors declare no conflict of interest.

[1] WHO, "Cardiovascular diseases (CVDs)," https://www.who.int/news-room/fact-sheets/detail/cardiovascular-diseases-(cvds) (accessed: May 2017).

[2] S. R. Steinhubl, E. D. Muse, E. J. Topol, *Sci. Transl. Med.* **2015**, *7*, 283rv3.

[3] J. P. DiMarco, J. T. Philbrick, *Ann. Intern. Med.* **1990**, *113*, 53.

[4] F. Ershad, K. Sim, A. Thukral, Y. S. Zhang, C. Yu, *APL Mater.* **2019**, *7*, 031301.

[5] A. K. Yetisen, J. L. Martinez-Hurtado, B. Ünal, A. Khademhosseini, H. Butt, *Adv. Mater.* **2018**, *30*, 1706910.

[6] E. Fung, M.-R. Järvelin, R. N. Doshi, J. S. Shinbane, S. K. Carlson, L. P. Grazette, P. M. Chang, R. S. Sangha, H. V. Huikuri, N. S. Peters, *Front. Physiol.* **2015**, *6*, https://doi.org/10.3389/fphys.2015.00149.

[7] C.-H. Chen, J.-S. Wen, C.-K. Wang, *Circulation* **2015**, *132*, 1284.

[8] D.-H. Kim, N. Lu, R. Ma, Y.-S. Kim, R.-H. Kim, S. Wang, J. Wu, S. M. Won, H. Tao, A. Islam, K. J. Yu, T.-I. Kim, R. Chowdhury, M. Ying, L. Xu, M. Li, H.-J. Chung, H. Keum, M. McCormick, P. Liu, Y.-W. Zhang, F. G. Omenetto, Y. Huang, T. Coleman, J. A. Rogers, *Science* **2011**, *333*, 838.

[9] J.-W. Jeong, W.-H. Yeo, A. Akhtar, J. J. S. Norton, Y.-J. Kwack, S. Li, S.-Y. Jung, Y. Su, W. Lee, J. Xia, C. Huanyu, Y. Huang, W.-S. Choi, T. Bretl, J. A. Rogers, *Adv. Mater.* **2013**, *25*, 6839.

[10] S. P. Lee, G. Ha, D. E. Wright, Y. Ma, E. Sen-Gupta, N. R. Haubrich, P. C. Branche, W. Li, G. L. Huppert, M. Johnson, H. B. Mutlu, K. Li, N. Sheth, J. A. Wright, Y. Huang, M. Mansour, J. A. Rogers, R. Ghaffari, *NPJ Digital Med.* **2018**, *1*, 2.

[11] E. Bihar, T. Roberts, Y. Zhang, E. Ismailova, T. Hervé, G. G. Malliaras, J. B. De Graaf, S. Inal, M. Saadaoui, *Flexible Printed Electron.* **2018**, *3*, 034004.

[12] S. Nie, C. Zhang, J. Song, *Sci. Rep.* **2018**, *8*, https://doi.org/10.1038/s41598-018-32152-4.

[13] S. R. Krishnan, C.-J. Su, Z. Xie, M. Patel, S. R. Madhvapathy, Y. Xu, J. Freudman, B. Ng, S. Y. Heo, H. Wang, T. R. Ray, J. Leshock, I. Stankiewicz, X. Feng, Y. Huang, P. Gutruf, J. A. Rogers, *Small* **2018**, *14*, 1803192.

[14] J. Kim, J. R. Sempionatto, S. Imani, M. C. Hartel, A. Barfidokht, G. Tang, A. S. Campbell, P. P. Mercier, J. Wang, *Adv. Sci.* **2018**, *5*, 1800880.

[15] S. R. Madhvapathy, Y. Ma, M. Patel, S. Krishnan, C. Wei, Y. Li, S. Xu, X. Feng, Y. Huang, J. A. Rogers, *Adv. Funct. Mater.* **2018**, *28*, 1802083.

[16] J. Sun, Y. Zhao, Z. Yang, J. Shen, E. Cabrera, M. J. Lertola, W. Yang, D. Zhang, A. Benatar, J. M. Castro, D. Wu, L. J. Lee, *Nanotechnology* **2018**, *29*, https://doi.org/10.1088/1361-6528/aacc59.

[17] J. Kim, I. Jeerapan, S. Imani, T. N. Cho, A. Bandodkar, S. Cinti, P. P. Mercier, J. Wang, *ACS Sens.* **2016**, *1*, 1011.

[18] R. A. Nawrocki, H. Jin, S. Lee, T. Yokota, M. Sekino, T. Someya, *Adv. Funct. Mater.* **2018**, *28*, 1803279.

[19] W. Dong, X. Cheng, T. Xiong, X. Wang, *Biomed. Microdevices* **2019**, *21*, 6.

[20] Y. Yamamoto, D. Yamamoto, M. Takada, H. Naito, T. Arie, S. Akita, K. Takei, *Adv. Healthcare Mater.* **2017**, *6*, 1700495.

[21] M. Mosallaei, J. Jokinen, M. Honkanen, P. Iso-Ketola, M. Vippola, J. Vanhala, M. Kanerva, M. Mäntysalo, *IEEE Trans. Compon., Packag., Manuf. Technol.* **2018**, *8*, 1344.

[22] Z. G. Yan, B. L. Wang, K. F. Wang, *Composites, Part B* **2019**, *166*, 65.

[23] L. Ren, S. Xu, J. Gao, Z. Lin, Z. Chen, B. Liu, L. Liang, L. Jiang, *Sensors* **2018**, *18*, 1191.

[24] M. Chi, J. Zhao, Y. Dong, X. Wang, *Materials* **2019**, *12*, 971.

[25] W. Liu, W. Zhou, S. Liu, C. Zhang, S. Huang, Y. Li, K. S. Hui, *Sens. Actuators, A* **2018**, *269*, 515.

[26] G. Li, S. Wang, Y. Y. Duan, *Sens. Actuators, B* **2018**, *277*, 250.

[27] T. Takeshita, M. Yoshida, Y. Takei, A. Ouchi, A. Hinoki, H. Uchida, T. Kobayashi, *Sci. Rep.* **2019**, *9*, 5897.

[28] M. Mantysalo, T. Vuorinen, V. Jeihani, A. Vehkaoja, *Proc. SPIE* **2017**, *10366*, 103660D.

[29] V. Jeyhani, T. Vuorinen, K. Noponen, M. Mäntysalo, A. Vehkaoja, in *XIV Mediterranean Conf. Medical and Biological Engineering and Computing 2016* (Eds: E. Kyriacou, S. Christofides, C. Pattichis), Springer, Cham, Switzerland **2016**, pp. 1144–1149.

[30] P. T. O'Gara, F. G. Kushner, D. D. Ascheim, D. E. Casey, M. K. Chung, J. A. de Lemos, S. M. Ettinger, J. C. Fang, F. M. Fesmire, B. A. Franklin, C. B. Granger, H. M. Krumholz, J. A. Linderbaum, D. A. Morrow, L. K. Newby, J. P. Ornato, O. Narith, M. J. Radford, J. E. Tamis-Holland, C. L. Tommaso, C. M. Tracy, Y. J. Woo, D. X. Zhao, *Circulation* **2013**, *127*, 529.

[31] T. Vuorinen, A. Vehkaoja, V. Jeyhani, K. Noponen, A. Onubeze, T. Kankkunen, A.-K. Puuronen, S. Nurmentaus, S. P. Preejith, J. Joseph, T. Seppanen, M. Sivaprakasam, M. Mantysalo, presented at *6th Electronic System-Integration Technology Conf., ESTC 2016*, Grenoble, France, September **2016**.

[32] A. V. Oppenheim, R. W. Schafer, J. R. Buck, *Discrete-Time Signal Processing*, 2nd ed., Prentice-Hall, Upper Saddle River, NJ **1999**.

[33] P. Kligfield, L. S. Gettes, J. J. Bailey, R. Childers, B. J. Deal, E. W. Hancock, G. van Herpen, J. A. Kors, P. Macfarlane, D. M. Mirvis, O. Pahlm, P. Rautaharju, G. S. Wagner, M. Josephson, J. W. Mason, P. Okin, B. Surawicz, H. Wellens, *Circulation* **2007**, *115*, 1306.

PUBLICATION
IV

Unobtrusive, Low-Cost Out-of-Hospital and In-Hospital Measurement and Monitoring System

Vuorinen T., Noponen K., Jeyhani., Aslam A., Junttila J., Tulppo M., Kaikkonen S., Huikuri H., Seppänen T., Mäntysalo M., and Vehkaoja A.

Unobtrusive, Low-Cost Out-of-Hospital, and In-Hospital Measurement and Monitoring System

Tiina Vuorinen,* Kai Noponen, Vala Jeyhani, Muhammad Awais Aslam, Matti Juhani Junttila, Mikko Paavo Tulppo, Kari Sakari Kaikkonen, Heikki Veli Huikuri, Tapio Seppänen, Matti Mäntysalo, and Antti Vehkaoja

Continuous monitoring of vital signs can be a life-saving matter for different patient groups. The development is going toward more intelligent and unobtrusive systems to improve the usability of body-worn monitoring devices. Body-worn devices can be skin-conformable, patch-type monitoring systems that are comfortable to use even for prolonged periods of time. Herein, an intelligent and wearable, out-of-hospital, and in-hospital four-electrode electrocardiography (ECG) and respiration measurement and monitoring system is proposed. The system consists of a conformable screen-printed disposable patch, a measurement unit, gateway unit, and cloud-based analysis tools with reconfigurable signal processing pipelines. The performance of the ECG patch and the measurement unit was tested with cardiac patients and compared with a Holter monitoring device and discrete, single-site electrodes.

1. Introduction

Cardiovascular diseases (CVDs)-related deaths (17.9 million deaths in 2016) are the most common causes of death and their number is rapidly increasing due to growth and aging of population, changes of living habits, and other epidemiologic factors. Identifying the people at the highest risk of CVDs and making sure that they receive proper treatment and monitoring can prevent premature deaths.[1,2] Both out-of-hospital and in-hospital cardiac monitoring for risk groups are needed to improve this global problem.

Traditional body monitoring systems have bulky electrodes, wires, connectors, and stationary or portable separate central units. The development is currently going toward more unobtrusive patch-type monitoring systems to improve usability and comfortability.[3–5] In addition, energy-storage and harvesting issues are important research topics in a field of wearable electronics.[6–8]

A lot of research is done in the field of wearable systems and cardiac disease monitoring.[9,10] ECG devices can be classified, for example, by the number of leads they are measuring, and the 12-lead ECG is considered as the standard practice to asses cardiac activity.[11] In a single-lead system one electrode pair ("lead") records the heart activity. As an example, Pradhan et al. studied ambulatory arrhythmia detection with single-channel ZIO XT Patch in pediatric patients and compared it with a regular Holter monitor.[12] Other patch-type single-lead devices are for example NUVANT and CAM.[13,14] There are also single-lead devices, such as AliveCor and ECG Check, that utilize a separate sensor unit that measures the ECG from the finger-tips.[15,16] Proesmans et al. studied a mobile phone-based use of the photoplethysmography technique to detect atrial fibrillation in primary care.[17]

In multilead systems several leads record the cardiac activity signals. As a result, the multilead systems provide more information from different angles of the heart. Lin et al. developed an artificial intelligence of things (AIoT) system for ECG analysis and cardiac disease detection.[18] In their study they used conventional wire-connected electrodes and an ECG-sensing device with 84.55 mm × 39.38 mm × 18.31 mm dimensions. Mishra et al. proposed a three-lead wearable ECG for real-time P-QRS-T detection and classification of various arrhythmias.[19] The measurement unit consists of conventional electrodes, wires, and a printed circuit board (PCB), and the last two are covered with a casing.

To further improve the possibilities for continuous monitoring of vital signs, we are proposing an intelligent, multilead,

T. Vuorinen, Prof. M. Mäntysalo
Faculty of Information Technology and Communication Sciences
Tampere University
33720 Tampere, Finland
E-mail: tiina.vuorinen@tuni.fi

K. Noponen, M. A. Aslam, Prof. T. Seppänen
Center for Machine Vision and Signal Analysis
University of Oulu
90570 Oulu, Finland

V. Jeyhani, Prof. A. Vehkaoja
Faculty of Medicine and Health Technology
Tampere University
33720 Tampere, Finland

Prof. M. J. Junttila, Prof. M. P. Tulppo, Dr. K. S. Kaikkonen,
Prof. H. V. Huikuri
Research Unit of Internal Medicine
Medical Research Center Oulu
University of Oulu and Oulu University Hospital
90570 Oulu, Finland

unobtrusive, low-cost system for both out-of-hospital and in-hospital monitoring. The proposed system follows the iHome Health-IoT concept proposed in a previous study[20] that included three main parts: Health-IoT on body, Health-IoT at home, and Health-IoT in cloud. There is, however, modifications and adaptations based on the observed needs and necessities. In this article, the proposed system has four main parts, which are shown in **Figure 1**. They are 1) measurement unit and printed electrodes, 2) gateway unit, 3) cloud-based data analysis and storing tools, and 4) front-end tools for data viewing and decision-making.

The system is designed with various different applications in mind, the primary ones including in-hospital and in-home clinical purposes. The system is designed for different modes of measurement, each having specific requirements, limitations, and advantages, enabling it to fit into a variety of applications ranging from online patient monitoring to Holter-type ECG data acquisition for post-hoc analysis. The proposed monitoring system was tested with cardiac patients in collaboration with Oulu University Hospital to verify its functionality.

The required duration of monitoring, required number of leads, and utility of real-time monitoring depend on clinical indications. A key benefit of the proposed architecture and system is its ability to accommodate different requirements with various ECG plaster design variations, automated distributed software component deployment changes, and different measurement modes. This makes the monitoring system a versatile tool suitable for various healthcare providers in cases that do not require the full 12-lead ECG due to clinical guidelines and recommendations.

The proposed system can increase the user acceptability, which have been shown[9] to increase study completion rates and clinical yields of arrhythmias diagnoses, for example, for atrial fibrillation due to the longer measurement durations. What is more, the developed electrode plaster with multiple channels and longer intraelectrode distances is able to capture both atrial and ventricular activity, enabling differential diagnosis of arrhythmias as well as other cardiac problems, such as ischemic events. Consequently, this also gives the proposed system the ability to verify the absence of abnormal cardiac findings during a long study period with a high enough certainty. This is also very critical information for correct clinical diagnosis. It should also be noted that the diagonal AS lead (electrode locations are shown in **Figure 2**a) is recommended for exercise

ECG PATCH   GATEWAY UNIT   CLOUD-BASED ANALYSIS TOOLS   FRONT-END FOR DATA VIEWING
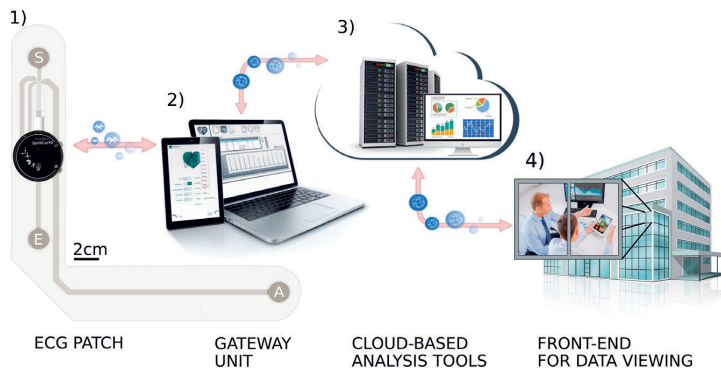
Figure 1. The system architecture that consists of four parts: the measurement unit and the electrode, the gateway unit, the cloud-based data analysis and storing tools, and front-end application for viewing the analysis results in real time or later.
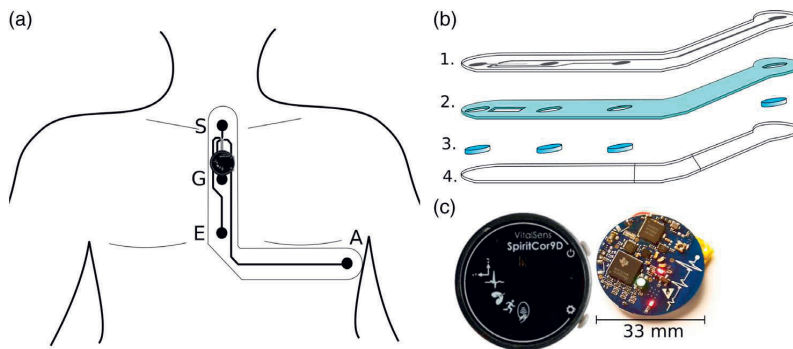
Figure 2. a) An illustration of the patch and the measurement unit in place. b) Electrode patch material layers. 1. thermoplastic polyurethane, 2. silicone adhesive, 3. hydrogel, and 4. PET supportive layer. c) The measurement unit and its PCB.

ADVANCED
SCIENCE NEWS
www.advancedsciencenews.com

ADVANCED
INTELLIGENT
SYSTEMS
Open Access

www.advintellsyst.com

testing, as it has high sensitivity for exercise-induced ischemia detection.[21–23] Hence, the presented system is also very applicable for ambulatory measurements with physical activity and exercise testing for which it has been separately validated.[24] Both the tolerance to motion-related artifacts and the possibility for lead-off detection with the impedance measurement lessen the false-alarm burden (e.g., pause and asystole). This has been identified as one of the key issues leading to sentinel events in the hospital setting.[25]

2. System Architecture

The measurement unit is responsible for signal acquisition, simple and low-level processing, and finally transmitting the measured data. The measurement unit is also able to store the data if needed. The unit is equipped with a flexible electrode bandage that provides a comfortable and consistent measurement of biosignals.

The gateway unit acts as a bridge between the measurement unit and the cloud-based analysis tools. Compared with the measurement unit, the gateway unit has a much more extensive processing power, battery resource, and various wireless communication technologies to satisfy the more complicated and demanding needs of the data-transmitting tunnels to the cloud. The connection between the measurement unit and the gateway unit is wireless. S2 shows the operation principles of the measurement unit and the graphical user interface in the mobile gateway unit.

The cloud provides data management solutions, which are essential to make it user-friendly and simple for interaction by medical experts, nurses, and patients. It also hosts powerful, reliable, and scalable signal processing pipelines to analyze the recorded data. The results are transferred and visualized to the related medical administrators in a well-managed and illustrative way. Depending on the application they can also be relayed back to the user.

As already said, the system is designed to work in different measurement modes to enable efficient use in different applications. The system can be used for real-time data viewing (only sending the data to the gateway) or only storing the data in the measurement unit. But it can be also used for both storing and transmitting or only transmitting and storing on the cloud.

2.1. Electrode Patch

Figure 2a shows the patch and measurement unit secured in place for monitoring. The electrode patch has four electrodes according to the EAS electrode system. EAS is a subset of the EASI electrode system that is a reduced lead system used mainly by Phillips in their cardiotelemetry systems. ECG recorded with EASI system is often mathematically converted to regular 12-lead ECG signals.[26] The electrode S is located on the manubrium, E is located on the lower part of the sternum, and A on the standard V5 electrode location of the 12-lead system. The electrode potentials are measured with respect to the common reference electrode G (between S and E) and three bipolar leads are formed as potential differences between the electrode sites S, E, and S.

These electrode patches were previously tested for movement artifacts and long-term wearability.[24,27]

Figure 2b shows the layer structure of the electrode patch. Layer 1 is thermoplastic polyurethane with silver and silver/silver chloride prints. Silicone adhesive (layer 2) provides firm adherence to the skin and circle-shaped hydrogel patterns ensure good signal quality. Layer 4 is a supportive PET film that will both protect the silicone adhesive layer and help in the installation of the electrode to a measurement subject. The PET film has two cuts so that the electrode patch can be put in place section by section and it is removed when applying the sensor.

2.2. Wireless Technologies

Bluetooth low energy (BLE), also referred to as Bluetooth Smart, is used as the wireless technology between the measurement and the gateway units. BLE offers a suitable power consumption profile for ambulatory devices and the data bandwidth still satisfies the needs of this work and also most other telemonitoring applications. The topology of BLE allows a multiconnection between a central device (a handheld device in this work) and several peripherals (measurement units in this work), meeting the needs of the proposed architecture.

BLE features different approaches to overcome the security problems in the wireless communication, among which, Out of Band (OOB) pairing satisfies the requirements in this application. OOB uses a different wireless technology such as Near Field Communication (NFC) to exchange the Term Key (TK) to encrypt the data. The TK in this pairing method can be up to 128 bits, significantly enhancing the security of the connection. As a result, assuming that the OOB channel is protected from man-in-the-middle (MITM) attacks and passive eavesdropping, the connection is also immune to those attacks. In addition, BLE is able to change the device address periodically to overcome the identity-tracking problems.

Additional benefit of BLE is its good tolerance for interference from other radios possibly located in the same space (in-home environment includes mainly WiFi) and operating in the same 2.4 GHz frequency band. Three advertising channels of BLE that are used in forming of a connection are located outside and between the WiFi channels and due to the frequency-hopping communication scheme (changing of the communication channel for each connection interval, i.e., tens of times per second) the data transmission is not compromised even though additional radio traffic would exist in the same frequencies.

The UART service is utilized for sending the raw data from the measurement device to the gateway unit. This service is able to transfer up to 20 bytes of data in one packet. Depending on the receiving device, there may be up to six packets sent in one BLE connection interval, which can be set as short as 7.5 ms. This sets the maximum theoretical limit for the rate of transmitted data when not considering the packet retransmissions. The structure of the 20-byte packet varies depending on the nature of the information being transmitted, being either command packets or data packets. The data packets, in addition to the actual data, include packet header and packet counter. Therefore, the central device is able to recognize which channel of data is received and if any packet has been dropped.

The command packets are used to transfer measurement configurations, status, and other types of information that concern the user. The measurement configuration consists of the settings selected by the user in interaction with the gateway device prior to starting the measurement. Settings such as the mode of the measurement, enabled channels and sensors, and selected data rate for each enabled channel are included in the configuration packet. Additionally, this type of packet includes some other information such as the time, date, and the subject ID.

The status packet is transmitted periodically to report the status of the measurement device to the gateway unit. Information such as battery level, status of lead-off detection flags, and number of BLE packets left in the buffer are sent via the status packet.

The nature of BLE brings a good level of compatibility with other devices. For instance, inclusion of the heart rate service in the measurement unit enables it to communicate directly with Android and iOS sports applications (assuming that the underlying hardware of the handheld device supports BLE). However, the self-defined data structure in the UART service limits the compatibility in sending the raw measurement data to other gateway unit software, which do not implement the same data structure.

2.3. Gateway Unit

The gateway unit can play different roles in the described architecture. For applications such as in-home monitoring, a handheld device such as a smartphone or a tablet is a beneficial choice. Using these devices, which are currently an inseparable part of our lives, not only is the cost of the system reduced but also the user adaptation to the system is simplified. Additionally, the handheld devices nowadays are equipped with powerful features and computing capabilities, which may be utilized in the system with only designing an app.

In this work, an Android application was designed that makes use of the BLE module of the mobile device to transmit and receive data from the measurement unit. The user configuring the monitoring system is able to choose the mode of the measurement and customize it according to her/his needs. Depending on the selected mode, the software is able to monitor the measured signals in real time, along with other useful information such as battery level.

2.4. Measurement Unit

The measurement device includes an nRF52832 Microcontroller Unit (MCU), which has a powerful BLE capable radio module and integrated BLE protocol stack. It also has a 32-bit ARM Cortex-M4F processor, 512 kB of flash memory and 64 kB of RAM, on-chip NFC unit, and several peripherals, which are required for the device, e.g., counters and analog-to-digital converters.

In this study, the device is used to measure three channels of ECG and impedance pneumography (IP). In addition, it can be used to record three channels of accelerometers and three channels of gyroscope signals. This is a combination that is not currently available in any of the commercial small-sized wearable monitoring devices, to the best of our knowledge.

The three channels of ECG can be utilized in measuring the EASI lead set or a subset of the standard 12-lead ECG e.g., limb leads and one channel of the chest leads. The IP signal is simultaneously measured through two of the ECG electrodes. The ECG and IP acquisition are powered by the ADS1294R analog-front-end circuit from Texas Instruments, providing additional features such as pacemaker detection, Central Wilson Terminal calculation, lead-off detection, and right-leg drive.

The electrode patch is connected to the device through a micro USB connector. The same connector is also used for connecting the measurement unit to a computer when extracting locally stored data and for charging it. A memory of two gigabytes is embedded in the device. The data structure is strictly controlled by the MCU to provide reliable and fast read and write processes. According to the designed data structure for the local memory, an empty memory can hold up to 5.4 days of measurement data including three channels of ECG with a data rate of 500 samples per second and a resolution of 24 bits. Obviously, the number of enabled channels, their resolution, and data rate have a direct impact on the amount of consumed memory per a unit of time.
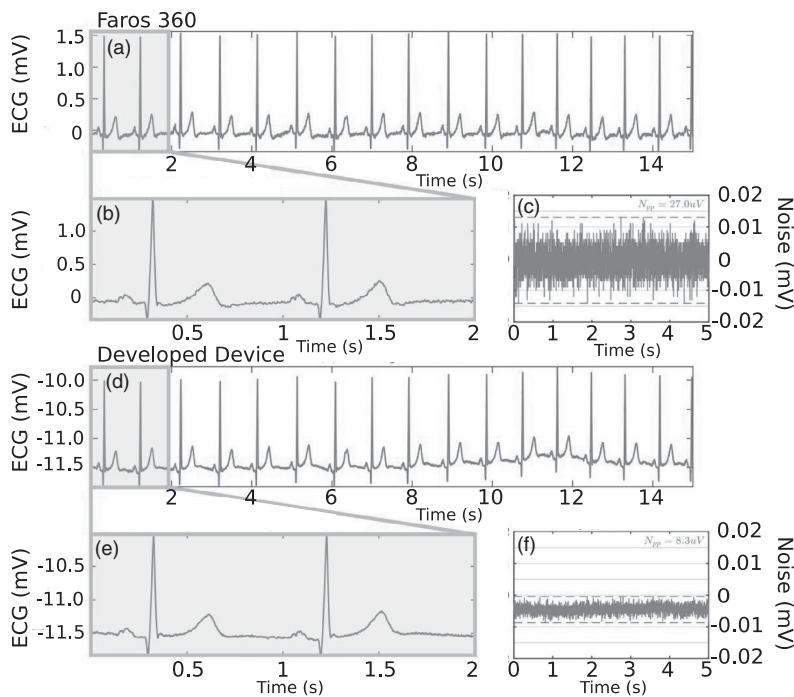
Figure 2c shows the measurement unit and its PCB. The unit has a circular shape with a diameter of 33 mm and the PCB consists of 4 layers and about 200 components. The tallest components on the top and bottom layers have a height of 1.83 and 2.51 mm, which are a red-green-yellow light-emitting diode (LED) and the micro USB connector. The PCB weighs 3.7 g with all the components assembled (except the battery), including an SD card. The total weight including a prismatic 300 mAh battery and the enclosure is 13.4 g.

The power consumption of the device naturally varies according to the measurement mode used and the number of measured signals. When all the measurement channels are activated and the data are both stored locally and transmitted over BLE, the average current consumption is 8.62 mA and the battery lifetime is approximately 35 h. When operated as a Holter device i.e., only ECG is measured and the data are stored locally, the battery lifetime extends to more than 100 h.

3. Preliminary Evaluation of Measurement Performance

To assess the quality of the measured ECG signal, lead II of the standard 12-lead system was measured simultaneously by two devices: the developed device and Faros 360 Holter device manufactured by Bittium Biosignals Ltd. Two pairs of electrodes were placed as close as possible to each other, one pair on the right forearm and one on the left ankle. The sampling rate in both of the devices was set to 1000 samples per second. Another test was made to compare the internal noise of the two devices by attaching the measurement input terminals together. In Faros device, a 196 kΩ resistance was connected between the inputs to emulate the fault current limiting series resistance of its electrode cables. In the proposed device this series resistance is built inside the device.

Figure 3 shows the result of the measurements. The signal measured with the developed device shows an equal quality in comparison with the reference device. The offset in the signal of the developed device (Figure 3d,e) is due to a difference in

**ADVANCED
SCIENCE NEWS**
www.advancedsciencenews.com

**ADVANCED
INTELLIGENT
SYSTEMS**
www.advintellsyst.com

Figure 3. a–c) Signal quality comparison between Faros 360 and d–f) the developed measurement device.
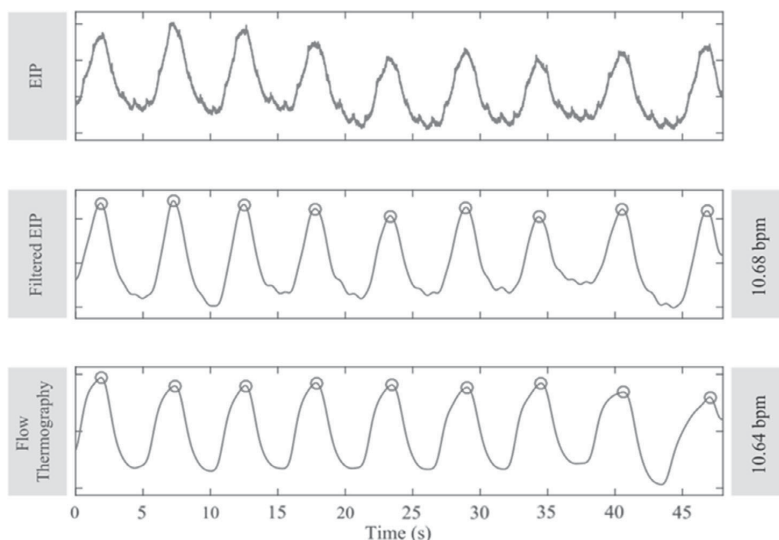
the half-cell potential of the measurement electrodes and the absence of any high-pass filtering of the measurement signal. The approach of not removing the baseline before the analog-to-digital conversion is advantageous as more powerful digital filtering methods can be used, which are able to preserve the desired low-frequency signal components' better analog filters. Figure 3c,f shows the internal noise signal of the two devices. About 8.3 µV peak-to-peak noise voltage was measured for the proposed device, which is over two-thirds smaller than 27.0 µV measured for the reference device. The difference is likely caused by different design choices and components used in the two devices but more accurate evaluation is not possible as the internal structure and components used in the commercial device are not public information.

Another test was made to optimize and verify the performance of the IP measurement. First, the coupling of cardiac components to the impedance signal was minimized by testing various excitation frequencies and measurement phase combinations in a measurement setting where electrodes were placed on V6 and VR6 locations. Excitation frequency of 32 kHz and phase of 67.5° were found as the optimal combinations. An example of the respiration signal measured with the aforementioned settings is shown in **Figure 4**. To evaluate the measurement signal, flow thermography was also performed simultaneously by a negative temperature coefficient (NTC) thermistor placed inside a breathing mask that was worn in front of the mouth and nostrils. The original measured IP signal and its filtered version are shown

in the first and second panels, respectively. The third panel illustrates the output of the NTC thermistor. The used filter was a band-pass infinite impulse response (IIR) filter with cut-off frequencies of 0.06 and 1 Hz, applied by the forward–backward technique. The quality of the filtered signals compared well with the quality of the gold standard flow thermography reference. The respiration rates calculated from the two signals are 10.68 and 10.64 breaths per minute. The advanced counting method proposed by Jeyhani et al. was utilized for estimating the respiration cycle length.[28]

4. Signal Processing and Cloud Service Architecture

We developed a scalable monitoring platform architecture for distributed signal processing. This enables efficient, reliable, and robust extraction of clinical markers from biosensor data in the presence of noise and artefacts stemming from the uncontrolled remote monitoring context. The architecture encompasses the whole system (measurement unit, gateway, and cloud) and is organized into configurable distributed pipelines of software components. The pipelines represent computational chains, e.g., starting from raw measurement data up to a specific arrhythmia alarm. The individual computational software components of the pipeline can be deployed on the wearable unit, the gateway, and/or the cloud as needed. This makes the system intelligently capable of adapting to the expectations, as also the

ADVANCED
SCIENCE NEWS
www.advancedsciencenews.com

ADVANCED
INTELLIGENT
SYSTEMS
Open Access
www.advintellsyst.com

Figure 4. IP signal measured with the proposed device in comparison with a gold standard flow thermography signal.

different pipeline configurations can be activated and automatically configured at will based on the clinical needs, to achieve desired quality of service and optimize power consumption and communication costs. The adaptation occurs via use case rules that activate predefined sets of components and set their parameters accordingly. This eases the setup procedure and facilitates large-scale deployment of the system for the masses. The components are interchangeable pieces of executable software that can be implemented in any suitable programming language and that communicate through the tcp/ip stack via predefined protocols, allowing for distributed deployment.

A working implementation of the platform was created using Python language. In this instance, all the signal processing pipelines for real-time remote ECG monitoring are deployed on the cloud service and interfaced by the signal routing component running on the gateway device. We used Web Application Messaging Protocol (WAMP) as a middleware solution to interconnect the software components. It is an open standard web socket protocol having implementations in Autobahn framework
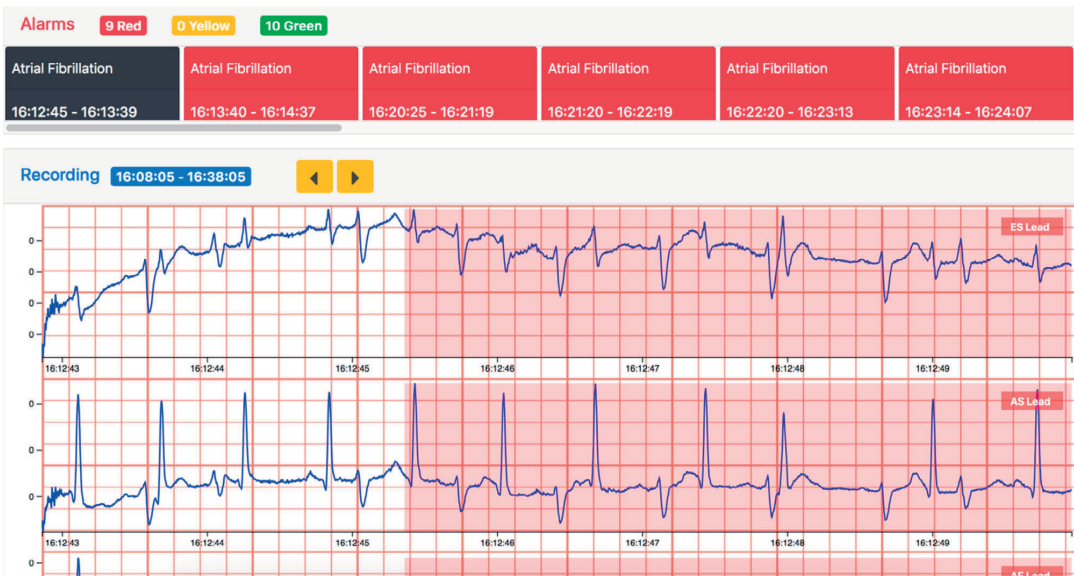
and Crossbar router which we also utilized. The utilization of WAMP and real-time performance considerations in ECG monitoring are described in more detail in a previous study.[29] The implemented signal processing pipelines detect heartbeats and extract the R-peak locations from the ECG, classify the beats, and calculate RR-interval tachogram signal and heart rate variability (HRV) features. There are also pipelines to detect arrhythmias such as pauses or asystoles, brady- and tachycardias, and atrial flutter or fibrillation categorized into three different levels of severity. These three categories are the following: green for suspected single-time events, yellow for potentially dangerous, and red for life critical events. Examples of previous categories are shown and described in **Table 1**.

The gateway unit sends the raw data from the measurement unit to the cloud where it is processed by the aforementioned computational pipelines. Next, the relevant results are returned back to the gateway device in a reasonable amount of time (in a couple of seconds). Some of the results are also transmitted to the physicians and nurses responsible for the ongoing

Table 1. Examples of arrhythmia diagnoses rules and respective alarm ratings.

Red alarms	Yellow alarms	Green alarms
HR exceeds 240 bpm for longer than 4 s, Ventricular fibrillation is diagnosed and red alarm is raised.	Average HR over 160 bpm, extreme tachycardia is diagnosed, and yellow alarm is raised.	Average HR of three consecutive beats lower than 40 bpm, bradycardia is diagnosed, and green alarm is raised.
Three consecutive ventricular beats with HR over 120 bpm, ventricular tachycardia is diagnosed, and red alarm is raised.	Average HR under 35 bpm, severe bradycardia is diagnosed, and yellow alarm is raised.	Three consecutive ventricular beats with HR under 120 bpm, ventricular rhythm is diagnosed, and green alarm is raised.
RR-interval of two consecutive beats is more than 4 s, asystole is diagnosed, and red alarm is raised.	–	RR-interval of two consecutive beats is more than 2 s, pause is diagnosed, and a green alarm is raised.

ADVANCED
SCIENCE NEWS
www.advancedsciencenews.com

ADVANCED
INTELLIGENT
SYSTEMS
Open Access
www.advintellsyst.com

Figure 5. A sample view of the web browser-based GUI for viewing the ECG data the cloud service.

measurement. Additionally, the outcomes of the pipeline analyses along with the raw data are stored in a database in the cloud. **Figure 5** shows the cloud service user interface implemented for data viewing. A test case is presented wherein supraventricular tachycardia is progressing into atrial fibrillation and the atrial fibrillation alarm is raised from the onset of arrhythmia.

5. Clinical Testing

The monitoring system was tested at Oulu University Hospital, with eight volunteers (two females, six males), as a substudy of ESCAPE-Part-II study (Clinical Utility of Home Monitoring of Electrocardiogram and other Vital Functions). The primary objectives of ESCAPE-Part-II research project were to examine the effects of exercise training on glucose control and cardiac autonomic function in patients with impaired glucose tolerance. There were no significant arrhythmias in the data of the subjects, which, however, was not unexpected as they were chosen based on glucose control to the study. There were premature ventricular contractions (PVCs) especially in subject three, but no other ventricular arrhythmias or atrial fibrillation. Overall, the proposed system could confirm the absence of aberrancy similarly to the analysis of the Faros 360 data.

A comparison of the signal quality in the ambulatory clinical use case was performed posthoc. QRS complexes were detected
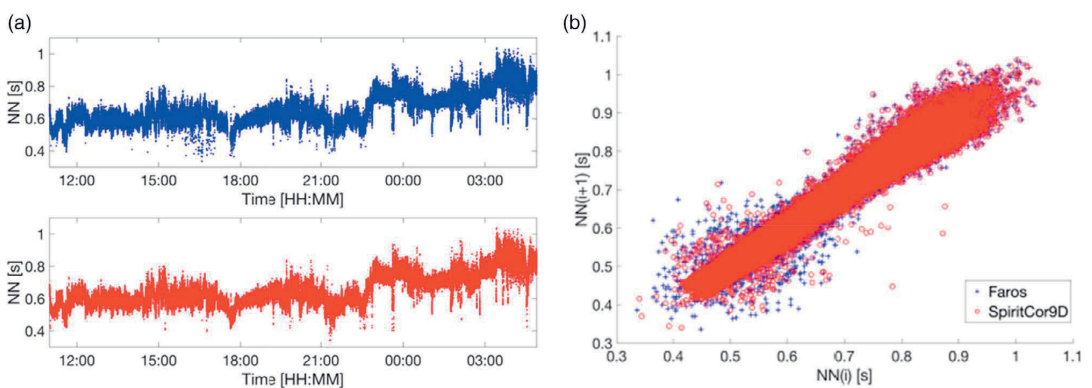
Figure 6. a) NN-tachograms of Faros 360 (top) and measurement unit (bottom) for the subject one. b) Superimposed Poincaré plots of the NN beats from Faros 360 (blue +) and measurement unit (red circle) for the subject one.

ADVANCED
SCIENCE NEWS
www.advancedsciencenews.com

ADVANCED
INTELLIGENT
SYSTEMS
Open Access
www.advintellsyst.com

from the magnitude signal from both devices using the R-peak detector implemented in the data analysis pipeline. The sampling rate of the developed device was set to 500 Hz during the long-term recording, to save storage space. Faros 360 data were upsampled with cubic splines from 250 to 500 Hz to match the sampling rate used in the proposed device. The magnitude signals were formed as the square root of the sum of squared channels after baseline wander removal with a zero-phase digital high-pass filter (0.67 Hz cutoff). Deviating beats and intervals were automatically filtered out from the RR-interval series by the following rules: the interval differs by more than 13.5% from the ten-beat average or R-peak amplitude is higher than 1.5 mV. Overall, the Faros 360 signal was more prone to noise for example due to the movement of cabling. This led to the removal of 5.9% of the Faros 360 RR-intervals compared with that of 1.4% of the measurement unit RR-intervals for subject one. Removed beats included ectopic beats such as PVCs and noise artefact detections. The larger amount of artefact signal in the commercial system may be due to the cabling of the individual electrodes being more influenced by movement and being more susceptible to tangling to clothing. **Figure 6**a shows the resulting NN-intervals of the subject one, and in Figure 6b the corresponding Poincaré plots are overlaid on each other to show the agreement between the consecutive intervals.

Over the course of the concurrent 24 h measurements, the clock rate(s) of either of the two devices or both of them wandered slightly with respect to each other when comparing the tachograms closely. Nevertheless, a good overall agreement can be seen from the plot shapes of Figure 6, and the clear similarity over the short-time durations is witnessed in Figure 6b.

6. Conclusion

In this study, the developed unobtrusive measurement and monitoring system is used to measure and record three channels of ECG and IP using a comfortable ECG patch. These recordings can provide extensive information on a person's health and also on the measurement context, helping to arrive at the correct diagnosis. Performed clinical tests indicate that the system provides HRV analysis capability comparable with and even exceeding the performance of a commercially available product conforming to medical device standards. They also indicate that the plaster ECG can be less susceptible to motion artifacts than

conventional electrodes using cabling, leading to the reduced rate of artifact beats.

There are many use cases for the proposed system. According to expert consensus, ambulatory ECG (AECG) monitoring can be recommended either for diagnosis or for risk stratification in patients with for example unexplained syncope or palpitations, atrial fibrillation, Wolf–Parkinson–White syndrome, cryptogenic stroke, newly diagnosed nonischemic cardiomyopathy or hypertrophic cardiomyopathy, arrhythmogenic right ventricular dysplasia, and after acute myocardial infarction or with a healed myocardial infraction and borderline ejection fraction.[9] It is also recommendable in monitoring the efficacy of arrhythmia suppression, especially with outpatient initiation of antiarrhythmic drugs, and to detect adverse drug responses.[30] The proposed system could be used in the hospital setting in scenarios wherein telemetry with reduced lead sets is warranted for arrhythmia or ST-level monitoring, for example, according to the American Heart Association (AHA) recommendations.[25]

We see that the proposed system for remote monitoring of vital functions is especially intriguing in the context of clinical practice. Currently, medical staff is under pressure to further shorten the hospitalized inpatient times, and relocation of patients to step-down units such as patient hotels has been discussed. Patient care in these step-down units can be made possible with such innovations expanding remote monitoring systems to patient hotels and ultimately to domestic environments in the future. In addition, the possibilities of the proposed kinds of systems in noncardiac units, such as orthopedic, should be explored further.

In the future, the user comfort could be improved with more conformable substrate materials that would also enable longer wearing time for the electrode patch. If this could be combined with a lower power consumption, the lifetime of the system could be prolonged up to a week or even to a month. In addition, extending the range of signal processing algorithms and diagnosis tools would enable the use of the system in a wider range of applications.

7. Experimental Section

Sample Fabrication: The manufacturing process as well as the material choices were designed in collaboration with Screentec Ltd. that produced the bandages according to our design and instructions. Circular electrode

Table 2. Subject demographics.

Gender	Age [year]	Height [cm]	Weight [kg]	SBP [mmHg]	DBP [mmHg]	Hba1C [mmol mol]	Diabetes medication	BP medication
F	50	155	83	111	85	37	Yes	No
M	56	175	93	137	103	43	No	No
M	55	180	123	126	81	42	No	Yes
M	53	178	117	160	112	42	Yes	No
M	59	175	106	125	82	43	No	No
F	53	161	98	134	91	54	Yes	Yes
M	54	178	98	130	80	41	No	No
M	57	175	94	149	95	37	Yes	No
	54.6 ± 2.8	172.1 ± 9.0	101.4 ± 13.3	134.0 ± 15.1	91.1 ± 11.6	42.4 ± 5.3		

ADVANCED
SCIENCE NEWS
www.advancedsciencenews.com

ADVANCED
INTELLIGENT
SYSTEMS
Open Access
www.advintellsyst.com

areas were screen printed using CI-4040 stretchable Ag/AgCl ink (ECM) and the circuitry was screen printed with stretchable silver ink. Ag/AgCl ink contained 40–50 wt% silver powder and 5–15 wt% silver chloride powder diluted in diethylene glycol ethyl ether acetate solvent. Printing was done on a 125 µm-thick stretchable thermoplastic polyurethane substrate (T 391, Policrom Screens) and the pattern was annealed in a convection oven after printing. A silicone adhesive layer was placed on top of the print and circular hydrogel pieces were placed at the electrode locations. In addition, the adhesive layer was used to attach the bandage to the skin. The used adhesive layer was so strong that normal body movements such as arm swing or rotation of upper body did not influence adhesion. Round-shape pieces of 0.89 mm-thick AG635 sensing gel (Axelgaard) were used at the electrode–skin interface to form a stable electrical contact.

Clinical Testing: Concurrent measurements were made with the measurement unit and a three-channel Faros 360 device. Chest hair was shaved prior to the recordings underneath the bandage. Next the skin was wiped with alcohol and dead skin cells were scraped off with Red Dot prep tape (3M). The bandage was then fixed in place and a data recording device attached to the bandage with a micro-USB connector. Flexifix adhesive film was used to secure the device in place and minimize any mechanical stress to the micro-USB connector. A similar process was followed to attach the Faros 360 electrodes but additionally the cabling was secured with skin tape. The recording was turned on and the participant was able to go home for the next 24 h. The recording stopped automatically after 24 h and patients returned the devices at the next day. **Table 2** shows the characteristics of the eight subjects who participated in this substudy.

The study was performed according to the Declaration of Helsinki, and the local committee of research ethics of the Northern Ostrobothnia Hospital District approved (#88/2015) the protocol and all the subjects provided written informed consent.

Supporting Information

Supporting Information is available from the Wiley Online Library or from the author.

Acknowledgements

Conflict of Interest

The authors declare no conflict of interest.

Keywords

[1] G. A. Roth, M. H. Forouzanfar, A. E. Moran, R. Barber, G. Nguyen, V. L. Feigin, M. Naghavi, G. A. Mensah, C. J. L. Murray, *N. Engl. J. Med.* **2015**, *372*, 1333.

[2] W. H. O. (WHO), *World Health Statistics 2018: Monitoring Health for the SDGs, Sustainable Development Goals*, WHO, Geneva **2018**.

[3] D.-H. Kim, N. Lu, R. Ma, Y.-S. Kim, R.-H. Kim, S. Wang, J. Wu, S. M. Won, H. Tao, A. Islam, K. J. Yu, T.-i. Kim, R. Chowdhury, M. Ying, L. Xu, M. Li, H.-J. Chung, H. Keum, M. McCormick, P. Liu, Y.-W. Zhang, F. G. Omenetto, Y. Huang, T. Coleman, J. A. Rogers, *Science* **2011**, *333*, 838.

[4] W.-H. Yeo, Y.-S. Kim, J. Lee, A. Ameen, L. Shi, M. Li, S. Wang, R. Ma, S. H. Jin, Z. Kang, Y. Huang, J. A. Rogers, *Adv. Mater.* **2013**, *25*, 2773.

[5] Y. Liu, M. Pharr, G. A. Salvatore, *ACS Nano* **2017**, *11*, 9614.

[6] Y. Zou, P. Tan, B. Shi, H. Ouyang, D. Jiang, Z. Liu, H. Li, M. Yu, C. Wang, X. Qu, L. Zhao, Y. Fan, Z. L. Wang, Z. Li, *Nat. Commun.* **2019**, *10*, 2695.

[7] B. Shi, Z. Liu, Q. Zheng, J. Meng, H. Ouyang, Y. Zou, D. Jiang, X. Qu, M. Yu, L. Zhao, Y. Fan, Z. L. Wang, Z. Li, *ACS Nano* **2019**, *13*, 6017.

[8] H. Ouyang, Z. Liu, N. Li, B. Shi, Y. Zou, F. Xie, Y. Ma, Z. Li, H. Li, Q. Zheng, X. Qu, Y. Fan, Z. L. Wang, H. Zhang, Z. Li, *Nat. Commun.* **2019**, *10*, 1821.

[9] E. Fung, M.-R. Järvelin, R. N. Doshi, J. S. Shinbane, S. K. Carlson, L. P. Grazette, P. M. Chang, R. S. Sangha, H. V. Huikuri, N. S. Peters, *Front. Physiol.* **2015**, *6*, 149.

[10] L. Y. Chen, N. S. Roetker, A. R. Folsom, A. Alonso, S. R. Heckbert, *Circulation* **2015**, *132*, A11721.

[11] P. Guzik, M. Malik, *J. Electrocardiol.* **2016**, *49*, 894.

[12] S. Pradhan, J. A. Robinson, J. K. Shivapour, C. S. Snyder, *Pediatr. Cardiol.* **2019**, *40*, 921.

[13] J. M. Engel, V. Mehta, R. Fogoros, A. Chavan, in *Annual Int. Conf. of the IEEE Engineering in Medicine and Biology Society*, IEEE, San Diego, CA **2012**, pp. 2440–2443.

[14] W. M. Smith, F. Riddell, M. Madon, M. J. Gleva, *Am. Heart J.* **2017**, *185*, 67.

[15] J. P. J. Halcox, K. Wareham, A. Cardew, M. Gilmore, J. P. Barry, C. Phillips, M. B. Gravenor, *Circulation* **2017**, *136*, 1784.

[16] H. T. Haverkamp, S. O. Fosse, P. Schuster, *Indian Pacing Electrophysiol. J.* **2019**, *19*, 145.

[17] T. Proesmans, C. Mortelmans, R. Van Haelst, F. Verbrugge, P. Vandervoort, B. Vaes, *JMIR Mhealth Uhealth* **2019**, *7*, e12284.

[18] Y. Lin, C. Chuang, C. Yen, S. Huang, P. Huang, J. Chen, S. Lee, in *IEEE Biomedical Circuits and Systems Conf.* IEEE, Nara **2019**, pp. 67–70.

[19] B. Mishra, N. Arora, Y. Vora, in *11th International Conference on Communication Systems & Networks*, IEEE, Bengaluru **2019**, pp. 870–875.

[20] G. Yang, L. Xie, M. Mäntysalo, X. Zhou, Z. Pang, L. D. Xu, S. Kao-Walter, Q. Chen, L. Zheng, *IEEE Trans. Ind. Informatics* **2014**, *10*, 2180.

[21] G. F. Fletcher, P. A. Ades, P. Kligfield, R. Arena, G. J. Balady, V. A. Bittner, L. A. Coke, J. L. Fleg, D. E. Forman, T. C. Gerber, M. Gulati, K. Madan, J. Rhodes, P. D. Thompson, M. A. Williams, *Circulation* **2013**, *128*, 873.

[22] M. Puurtinen, T. Nieminen, M. Kähönen, T. Lehtimäki, R. Lehtinen, K. Nikus, J. Hyttinen, J. Viik, *Clin. Physiol. Funct. Imaging* **2010**, *30*, 308.

[23] A. A. Quyyumi, T. Crake, L. J. Mockus, C. A. Wright, A. F. Rickards, K. M. Fox, *Br. Heart J.* **1986**, *56*, 372.

[24] T. Vuorinen, K. Noponen, A. Vehkaoja, T. Onnia, E. Laakso, S. Leppänen, K. Mansikkamäki, T. Seppänen, M. Mäntysalo, *Adv. Mater. Technol.* **2019**, *0*, 1900246.

[25] K. E. Sandau, M. Funk, A. Auerbach, G. W. Barsness, K. Blum, M. Cvach, R. Lampert, J. L. May, G. M. McDaniel, M. V. Perez, S. Sendelbach, C. E. Sommargren, P. J. Wang, *Circulation* **2017**, *136*, e273.

[26] K. Nikus, J. Lähteenmäki, P. Lehto, M. Eskola, *J. Electrocardiol.* **2009**, *42*, 473.

ADVANCED
SCIENCE NEWS

www.advancedsciencenews.com

ADVANCED
INTELLIGENT
SYSTEMS
Open Access

www.advintellsyst.com

[27] M. Mäntysalo, T. Vuorinen, V. Jeihani, A. Vehkaoja, in *Proc. SPIE – Int. Soc. Opt. Eng.*, **2017**.

[28] V. Jeyhani, T. Vuorinen, M. Mäntysalo, A. Vehkaoja, *Health Technol.* **2017**, *7*, 21.

[29] A. Aslam, A. Tiulpin, K. Noponen, T. Seppänen, *EMBEC & NBC 2017. EMBEC 2017, NBC 2017. IFMBE Proceedings*, Springer Singapore **2018**.

[30] J. S. Steinberg, N. Varma, I. Cygankiewicz, P. Aziz, P. Balsam, A. Baranchuk, D. J. Cantillon, P. Dilaveris, S. J. Dubner, N. El-Sherif, J. Krol, M. Kurpesa, M. T. La Rovere, S. S. Lobodzinski, E. T. Locati, S. Mittal, B. Olshansky, E. Piotrowicz, L. Saxon, P. H. Stone, L. Tereshchenko, G. Turitto, N. J. Wimmer, R. L. Verrier, W. Zareba, R. Piotrowicz, *Hear. Rhythm* **2017**, *14*, e55.

2000030 (10 of 10)

PUBLICATION
V

High resolution E-jet Printed Temperature Sensor on Artificial Skin

Vuorinen T., Laurila M.-M., Mangayil R., Karp M., and Mäntysalo M.

High Resolution E-Jet Printed Temperature Sensor on Artificial Skin

T. Vuorinen[1], M.-M. Laurila[1], R. Mangayil[2], M. Karp[2] & M. Mäntysalo[1]

[1] Tampere University of Technology, Faculty of Computing and Electrical Engineering, Tampere, Finland
[2] Tampere University of Technology, Faculty of Natural Sciences, Tampere, Finland

Abstract—**Skin-conformable electronics research field has grown rapidly during the recent years. Body monitoring systems are shrinking in size and integrating more seamlessly with the human skin. To make these monitoring systems feasible options, new suitable materials and manufacturing processes needs to be studied. This paper presents materials and a simple fabrication process for skin-conformable, E-jet printed silver temperature sensors. Utilizing printing processes and biodegradable substrate materials, the skin-conformable electronics may become attractive for disposable systems by decreasing the manufacturing costs and reducing the amount of waste materials. In this study, the temperature sensors are fabricated with E-jet printed silver nanoparticle ink and the printing is done on a bacterial nanocellulose substrate. During the characterization, the silver temperature sensors were able reach more than 0.06 % per degree Celsius sensitivity and they exhibited positive temperature dependence.**

Keywords— **E-jet, printed electronics, temperature sensor, bacterial nanocellulose**

I. Introduction

One development direction in vital sign monitoring is to make the monitoring devices as user friendly as possible. The progress is done by shrinking the device dimensions, especially thickness, which helps the devices to integrate seamlessly with a human body. This requires wireless monitoring systems and new kind of device structures, such as skin-like electronics. Skin-conformable structures, that measure for example ECG [1][2], chronic wounds [3], and temperature [4–6], have already being studied with plastic substrates and the next step is to make the substrate material to integrate with the skin even more seamlessly. This can be done, for instance, by using temporary tattoo type of a materials to attach the electronics to the skin. In addition, to reduce the environmental impact in disposable systems, other materials than synthetic polymers need to be studied.

Cellulose, obtained from plants, is the most abundant biopolymer on Earth and is the biomaterial of choice for various industrial applications, for example, textile, pulp and paper [7]. However, the process of harvesting the cellulose content from lignocellulose requires harsh pretreatment steps with high-energy input and often generates byproducts (aromatic lignin derivatives) and/or toxic sulfoxide residues

[7][8]. In addition to plants, production of extracellular cellulose in some bacterial genera has also been established [9–11]. Cellulose synthesized by microorganisms is highly pure (devoid of lignin and hemicellulose impurities) compared to plant-based cellulose. Thus, bacterial nanocellulose aids to circumvent the harsh processing step, making the production process sustainable. In terms of biopolymer characteristics, bacterial nanocellulose has high level of crystallinity, superior structural integrity, mechanical, optical, biodegradable and water holding properties [7].

In addition to suitable substrate materials, the skin-conformable electronics requires the functionalities found from a human skin. To match the receptor density in the skin, the manufacturing methods need to be able to fabricate very high resolution sensor structures for skin-conformable electronics. One option is to use electrohydrodynamic inkjet (E-jet) printing [12]. Compared to the conventional piezo or thermal actuator based inkjet devices, the E-jet offers up to ten times higher resolution and thousand fold ink viscosity range (10-20 mPa·s [13] vs 0.1-10000 mPa·s [14]). This enables the continued device miniaturization in the field of printed electronics, while still using the same low temperature inks developed for conventional inkjet devices.

In this paper, we report a manufacturing process and materials for high resolution E-jet printed silver temperature sensors. The sensors were fabricated using screen-printed, stretchable silver flake ink, E-jet printed silver nanoparticle ink, and bacterial nanocellulose substrate material. Sensors were characterized in ambient atmosphere to verify the temperature coefficient of resistance (TCR) of the printed sensors. Both the inks and the substrate material enable the printing fabrication of disposable, skin-conformable systems.

II. Materials and methods

A. Bacterial nanocellulose cultivation

The bacterial nanocellulose films were prepared from *Komagataeibacter xylinus*, a natural cellulose producer. To prepare the seed cultures for bacterial nanocellulose production, *K. xylinus* (from glycerol stocks) were inoculated into 5 ml glucose (20 g L^{-1}) amended buffered Hestrin-Schramm (HS, pH 6.0) growth medium [g L^{-1}: peptone, 5; yeast extract, 5; di-sodium hydrogen phosphate, 2.7 and citric acid, 1.15) and

grown at 30°C/180 rpm for 4 days. For bacterial nanocellulose production, the seeds cultures were inoculated to 30 ml of similar growth medium in sterile petri dish and incubated statically at 30°C for 4 days.

At the end of the cultivation, bacterial cells entrapped within the produced cellulose were inactivated by rinsing the nanocellulose sheets with ultrapure water (Milli-Q, EMD Millipore, Germany) and incubating overnight in 0.5 M sodium hydroxide solution at 60°C. The alkali solution was removed by repeated washing with ultrapure water until neutral pH was attained. Subsequently, the washed bacterial nanocellulose sheets were dried at 60°C for 16 hours and the dried nanocellulose films were used in this study.

B. Substrate preparation and screen printing process

The nanosellulose films are too thin to be used in the printing process without a carrier. To make the carrier, a 125 μm thick Melinex ST506 polyethylene terephthalate (PET) films were coated with a layer of Sylgard 184 polydimethylsiloxane (PDMS). A layer of PDMS, with 200 μm wet thickness, was spread using a CX202 bar coater together with an applicator. The coating speed was 18 mm/s, and the coated samples were cured in a convection oven at 130°C for 10 minutes. The PET film provides mechanical support and the PDMS functions as a release layer, so that the nanocellulose could be removed from the carrier without softening the cellulose with water.

Silver conductors were screen printed using TIC SCF-300 screen printer and CI-4040 stretchable Ag/AgCl ink (ECM). The silver ink contains 40 – 50 wt% silver powder and 5 – 15 wt% silver chloride powder diluted in a diethylene glycol ethyl ether acetate solvent. The printed pattern was defined by a polyester screen with a mesh count of 79 threads cm^{-1}, a mesh opening of 69 μm, and a stretching angle of 22.5°. After printing, the silver patterns were annealed in a convection oven at 130 °C for 30 minutes.

C. High resolution inkjet printing process

The meander sensor structures were fabricated using a commercially available E-jet device, Super Inkjet (Super Inkjet Technology Inc., Japan). In the current application, the sensors are printed using DGP 40TE-20C silver nanoparticle ink (Advanced Nano Products Ltd, Korea). The ink had a solid content of 30 – 35 wt% diluted in triethylene glycol monoethyl solvent [15]. After printing the ink was sintered at 150 °C for 1 h.

The operation of E-jet is based on electric field generated droplet emission from ink meniscus at the tip of a glass nozzle. The size of the droplets can be controlled by adjusting the field intensity between the meniscus and grounded xy-stage i.e. by changing the DC-, or peak voltage (V_{DC}, V_{peak}) and nozzle-to-substrate distance (d). The conductor width is further controlled by the relationship between droplet ejection frequency (f) and printing speed (v), while the conductor thickness is principally controlled by the number of printed layers. The printing parameters are presented in Table 1.

Table 1. E-Jet print parameters for meander structure

Parameter	Value
V_{DC} (V)	0
V_{peak} (V)	440
f (Hz)	10
v (μm/s)	130
d (μm)	20
number of layers	20

The print was performed in ambient atmosphere with recorded temperature of 21.1°C and relative humidity of 20 %.

D. Electrical characterization setup

A resistance measurement setup was used, together with a heating/cooling unit, to assess the resistance dependence on
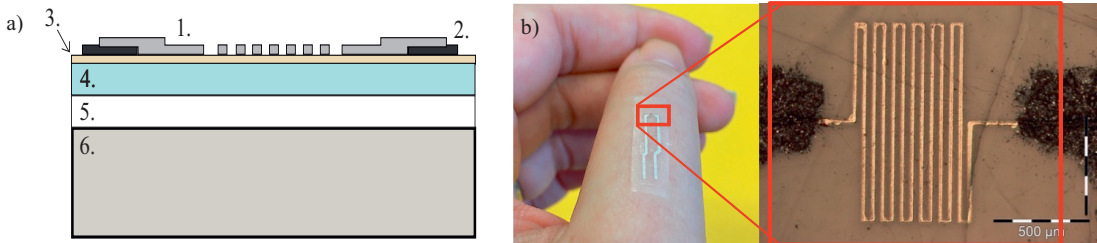

Fig. 1 A) Cross section of the sample on the Peltier element. B) A photograph and an optical microscope image of the silver temperature sensor.
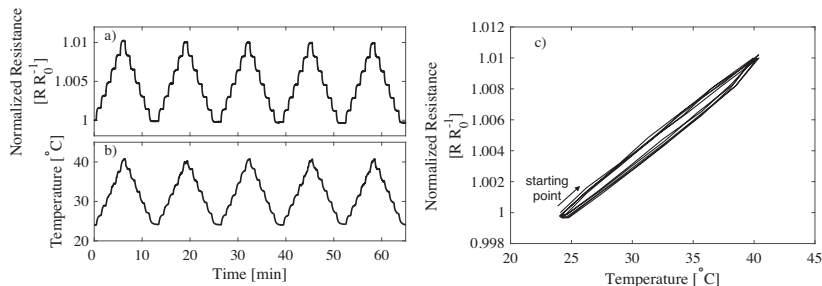
Fig. 2 a) normalized resistance and b) measured temperature from the samples. Temperature was increased and decreased between 24 °C and 41 °C during the measurements and this cycling was done five times for the samples. The measured data from a) and b) is presented in form of normalized resistance as a function of temperature c) during the five temperature cycles between 24 °C to 41 °C.

temperature in ambient conditions. In the resistance measurement setup, a LabVIEW system design software driven digital multimeter in a VirtualBench (National Instruments) measured the resistance of the samples with a 1 Hz sampling rate. VirtualBench also drove the heating/cooling unit, which consisted of a Peltier element and Silverstone Tundra TD03 liquid cooler that kept one side of the Peltier at a constant room temperature. TC-08 thermocouple Data Logger (Pico Technology) was used to measure the temperature of the plaster surface. During the electrical characterization, VirtualBench increased and decreased the Peltier voltage stepwise using 0.4 V steps and the voltage was kept constant for 1 min. The temperature cycling fluctuated approximately between 24 °C and 41 °C, and complete cycles (increase from 24 °C to 41 °C and decrease form 41 °C to 24 °C) were done five times for the samples.

III. RESULTS

Fig. 1 a) shows the multilayered structure of the samples. E-jet printed silver nanoparticle sensor (1.) is fabricated on top of the screen-printed silver conductors (2.). Nanocellulose substrate (3.) is spread on the PDMS release layer (4.). PET film (5.) provides mechanical support during the processing steps and measurements. The sample is placed on a Peltier element (6.) in the electrical characterization setup. Fig. 1 b) presents a photograph of the sample being attached to the skin and an optical microscope image of the E-jet printed sensor part. The meander shaped sensor had approximately 20 µm conductor width with 50 µm spacing.

The temperature cycling was repeated five times for the samples and results from one sample is presented in Fig. 2. Fig. 2 a) shows the results as normalized resistance and (b) corresponding temperature values. In Fig. 2 c) the measured data from a) and b) is transformed in form of normalized resistance as a function of temperature during the five temperature cycles.

Fig. 3 presents a response time and a recovery time for one sample. In Fig. 3 (left side) the input voltage of the Peltier element is increased by 0.4 V and is then kept unaltered for 1 minute. The 90th percentile response time was 15 seconds with this Peltier element setup. It needs to be noticed that the Peltier element also has a response time which reflects to the response time of the temperature sensor. Fig. 3 (right side) shows a 90th percentile recovery time of 17 seconds for the sensor when the Peltier voltage is decreased by 0.4 V.

IV. DISCUSSION

Dielectric substrates, such as nanocellulose, pose additional challenges for E-jet printing process since the remaining charge in printed droplets takes longer to decay and may therefore affect the droplet generation during printing of subsequent layers. One approach to compensate for this effect is to print alternately positive and negative droplets (i.e. by setting V_{DC} to 0 Volts) [16]. The spraying of droplets on dielectric surfaces can be minimized by reducing the nozzle-to-substrate distance and print frequency. As a trade-of, the printing speed must be reduced which will limit the throughput of the process. Taking these restrictions in the account, the print parameters were calibrated to produce approximately 20 µm conductor width (Table 1).
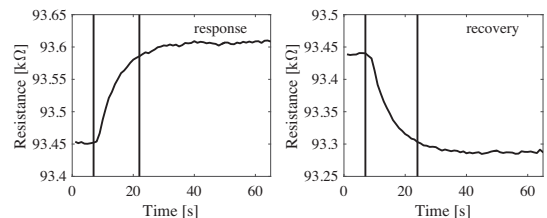

Fig. 3 *One heating step and one cooling step to visualize the response time and the recovery time. The 90th percentile response time was 15 seconds and the 90th percentile recovery time was 17 seconds.*

During the temperature cycling the resistance was increasing when the temperature was increasing, as was expected from the silver sensor since the silver is a positive temperature coefficient (PTC) material. The level of hysteresis stays low and the TCR is 0,0602 % per degree Celsius. The sensor would not compete in efficiency with already existing temperature sensors but the sensor could be used in its present form to indicate if the local body temperature is going up or down. This can be a beneficial indicator of fever or healing infections.

V. Conclusions

The fabrication process presented in this paper, enable a straightforward fabrication procedure for E-jet printed silver temperature sensors compatible with skin-conformable bacterial nanocellulose substrate. Ideally the printed skin-like sensors are targeted for disposable systems. This is due to the decreased number of fabrication steps, reduced amount of waste material and possibility to use new kind of substrate materials, compared to the traditional lithography processed devices. Using bacterial nanocellulose as the substrate material minimizes the negative environmental impact remarkably compared to plastic substrates.

The sensors were fabricated with E-jet printed nanoparticle silver ink and screen printed silver fake ink on top of a skin-formable nanocellulose substrate, which provides temporary-tattoo type of base for the system. The completed printed system is light-weight, thin, and can seamlessly integrate with the skin. The device has the possibility to monitor temperature changes directly on human skin with a TCR value 0.06% per degree Celsius in ambient conditions.

Conflict of Interest

The authors declare that they have no conflict of interest.

References

1. Vuorinen T, Vehkaoja A, Jeyhani V, et al (2016) Printed, skin-mounted hybrid system for ECG measurements. 2016 6th Electron Syst Technol Conf 1–6. doi: 10.1109/ESTC.2016.7764710
2. Khan Y, Garg M, Gui Q, et al (2016) Flexible Hybrid Electronics: Direct Interfacing of Soft and Hard Electronics for Wearable Health Monitoring. Adv Funct Mater 26:8764–8775. doi: 10.1002/adfm.201603763
3. Farooqui MF, Shamim A (2016) Inkjet printed wireless smart bandage. 2016 IEEE Middle East Conf Antennas Propag 1–2. doi: 10.1109/MECAP.2016.7790102
4. Hong SY, Lee YH, Park H, et al (2016) Stretchable Active Matrix Temperature Sensor Array of Polyaniline Nanofibers for Electronic Skin. Adv Mater 28:930–5. doi: 10.1002/adma.201504659
5. Bali C, Brandlmaier A, Ganster A, et al (2016) Fully Inkjet-Printed Flexible Temperature Sensors Based on Carbon and PEDOT:PSS1. Mater Today Proc 3:739–745. doi: 10.1016/j.matpr.2016.02.005
6. Vuorinen T, Niittynen J, Kankkunen T, et al (2016) Inkjet-printed graphene/PEDOT:PSS temperature sensors on a skin-conformable polyurethane substrate. Sci Rep. doi: 10.1038/srep35289
7. Jozala AF, de Lencastre-Novaes LC, Lopes AM, et al (2016) Bacterial nanocellulose production and application: a 10-year overview. Appl Microbiol Biotechnol 100:2063–2072. doi: 10.1007/s00253-015-7243-4
8. Lee K-Y, Buldum G, Mantalaris A, Bismarck A (2014) More Than Meets the Eye in Bacterial Cellulose: Biosynthesis, Bioprocessing, and Applications in Advanced Fiber Composites. Macromol Biosci 14:10–32. doi: 10.1002/mabi.201300298
9. Schramm M, Hestrin S (1954) Factors affecting production of cellulose at the air/liquid interface of a culture of Acetobacter xylinum. J Gen Microbiol 11:123–129. doi: 10.1099/00221287-11-1-123
10. Hungund BS, Gupta SG (2010) Production of bacterial cellulose from Enterobacter amnigenus GH-1 isolated from rotten apple. World J Microbiol Biotechnol 26:1823–1828. doi: 10.1007/s11274-010-0363-1
11. Tanskul S, Amornthatree K, Jaturonlak N (2013) A new cellulose-producing bacterium, Rhodococcus sp. MI 2: Screening and optimization of culture conditions. Carbohydr Polym 92:421–428. doi: 10.1016/j.carbpol.2012.09.017
12. Laurila MM, Khorramdel B, Mäntysalo M (2017) Combination of E-Jet and Inkjet Printing for Additive Fabrication of Multilayer High-Density RDL of Silicon Interposer. IEEE Trans Electron Devices 64:1217–1224. doi: 10.1109/TED.2016.2644728
13. Hutchings IM, Martin GD (2012) Introduction to Inkjet Printing for Manufacturing. In: Inkjet Technol. Digit. Fabr. John Wiley & Sons, Ltd, pp 1–20
14. Murata K, Masuda K (2011) Super Inkjet Printer Technology and Its Properties. Convert e-Print 108–111.
15. Advanced Nano Products Ltd. ANP Silverjet datasheet at:http://anapro.com/eng/product/silver_inkjet_ink.html.
16. Wei C, Qin H, Ramírez-Iglesias NA, et al (2014) High-resolution ac-pulse modulated electrohydrodynamic jet printing on highly insulating substrates. J Micromech Microeng 24:45010.

Enter the information of the corresponding author:

Author: Tiina Vuorinen
Institute: Tampere University of Technology
Street: Korkeakoulunkatu 3
City: Tampere
Country: Finland
Email: tiina.vuorinen@tut.fi

PUBLICATION
VI

Inkjet-Printed Graphene/PEDOT:PSS Temperature Sensors on a Skin-Conformable Polyurethane Substrate

Vuorinen T., Niittynen J., Kankkunen T., Kraft T., and Mäntysalo M.

SCIENTIFIC REP⚙RTS

OPEN

Inkjet-Printed Graphene/PEDOT:PSS Temperature Sensors on a Skin-Conformable Polyurethane Substrate

Tiina Vuorinen, Juha Niittynen, Timo Kankkunen, Thomas M. Kraft & Matti Mäntysalo

Epidermal electronic systems (EESs) are skin-like electronic systems, which can be used to measure several physiological parameters from the skin. This paper presents materials and a simple, straightforward fabrication process for skin-conformable inkjet-printed temperature sensors. Epidermal temperature sensors are already presented in some studies, but they are mainly fabricated using traditional photolithography processes. These traditional fabrication routes have several processing steps and they create a substantial amount of material waste. Hence utilizing printing processes, the EES may become attractive for disposable systems by decreasing the manufacturing costs and reducing the wasted materials. In this study, the sensors are fabricated with inkjet-printed graphene/PEDOT:PSS ink and the printing is done on top of a skin-conformable polyurethane plaster (adhesive bandage). Sensor characterization was conducted both in inert and ambient atmosphere and the graphene/PEDOT:PSS temperature sensors (thermistors) were able reach higher than 0.06% per degree Celsius sensitivity in an optimal environment exhibiting negative temperature dependence.

Vital sign monitoring is evolving from stationary, wire-connected monitoring to a more mobile monitoring with wireless sensor systems. Monitoring devices are shrinking in physical size and weight, and the monitoring electronics are brought closer to the patient, as is already done with wearable measurement devices. Low levels of electrical current drive many physiological functions, and the human body is constantly radiating heat through the skin. Due to these phenomena, several kinds of physiological parameters can be measured using skin mounted devices. One of the interesting parameters is skin temperature, and for that reason a skin thermometer can be utilized in the investigation of cardiovascular health, physical activity and ulcer prediction and prevention[1–4]. A variety of body monitoring systems are already familiar in both the hospital environment and more casual environments for tracking physical activity. To improve the skin/sensor interface and wearability (comfort and ease of application) in these tracking situations, the development is transitioning from rigid and planar electronic systems towards more adaptable, skin-like electronics[5,6]. These types of soft, stretchable, thin-film devices are referred to as epidermal electronic systems (EESs)[7]. EESs are electronic systems which can be placed on human skin, and their structure and mechanical properties mimic the behaviour of the epidermis.

The EES structures need to be very thin and soft to be able to seamlessly integrate with the skin[8]. These properties, however, make the EESs very prone to wrinkling and self-adhesion, or the adhesive may wear down, when they are peeled off from the epidermis. For this reason, the full potential of EESs can be utilized in form of low-cost, disposable epidermal measurements systems[9]. For example, the disposability may be a preferred feature in medical devices where a high level of cleanliness is required. Common fabrication processes for EESs are, for example, spin coating, vacuum deposition of materials, photolithography and etching. However, these can be complex and consume a high degree of materials[7,10–12]. Rigid carrier wafers, used in these processes, are incompatible with targeted roll-to-roll (R2R) manufacturing. In addition, photolithography and etching require chemicals and create waste material, and the vacuum deposition of materials is time consuming and has a substrate area limited by the vacuum chamber size[9]. Efficient manufacturing of disposable devices requires simple,

Tampere University of Technology, Department of Electronics and Communications Engineering, Korkeakoulunkatu 3, 33720, Tampere, Finland. Correspondence and requests for materials should be addressed to T.V. (email: tiina. vuorinen@tut.fi)

material-sparing, and low cost manufacturing processes. Furthermore, exploiting additive printing processes in manufacturing reduces both process steps and waste materials along the EES fabrication process.

To fabricate epidermal electronics, the electronic structures need to withstand the dynamic behaviour and uneven character of the skin. This can be achieved by designing patterns so that the 3D structure of the pattern improves the mechanical properties of the electronic structures. A so-called stretching-patterning-release process, where the substrate is strained prior to material deposition and released afterwards, can be used to pattern stretchable "wavy" patterns[13]. Another possibility is to use in-line horseshoe-like structures which can be found in several applications[7,10–12,14]. In addition to increasing the stretchability of the 3D structure, the functional material itself can be stretchable. Stretchable, functional materials may be single- or multi-component composites containing functional polymers, nanostructural carbon and metal components[15–17]. In previously mentioned materials the functional component itself may be stretchable, or rigid components are dispersed in a more mechanically deformable matrix. Stretchable, functional materials can also be diluted in solvents, and hence used in form inks. Matsuhisa *et al.* have developed a highly conductive silver ink which consists of silver flakes, fluorine rubber, and fluorine surfactants. Remarkably, with 215% stretching strain the initial conductivity of 738 S cm^{-1} did not decrease lower than 182 S cm^{-1}[18]. Bandodkar *et al.* used the conductive polymer poly(3,4-ethylenedioxythiophene): poly(styrenesulfonate) (PEDOT:PSS) and silver/silver chloride (Ag/AgCl) inks where the conductive material was mixed with silicone-based elastomeric material and a non-ionic surfactant[15].

Conductive polymers are organic polymers, which conduct electricity and may exhibit electrical characteristics that are either like a metal or semiconductor. The widely used PEDOT:PSS has a relatively high conductivity and optical transparency in its doped state[18]. Due to its favourable electrical and optical properties, PEDOT:PSS has been utilized in various applications. This includes, but is not limited to, transparent electrodes for indium tin oxide-free organic light emitting diodes (OLEDs) and polymer solar cells (PSCs), anode material together with ZnO/C hierarchical porous nanorods for lithium ion batteries, and composite electrodes with multi-walled carbon nanotubes for supercapacitors[19–22]. Moreover, related to this study, PEDOT has also been used for thermal sensors[23]. The temperature dependent behaviour of the PEDOT:PSS originates from the microstructure of the polymer material. PEDOT:PSS forms so-called core-shell structured grains in which the core of the grain is a PEDOT nanocrystal and a PSS-rich shell surrounds the core[24]. The insulating PSS boundaries have a major effect to the overall resistivity of the PEDOT:PSS. At high temperatures the total number of particle boundaries is smaller and the effective "size" of the boundaries is reduced which will reduce the resistance. When the temperature decreases the electrons may not possess enough thermal energy anymore to overcome these boundaries and the resistance increases[25]. In addition to its electrical, thermal and optical properties, PEDOT:PSS has shown interesting mechanical properties to be used in EESs. One such property is its stretchability which is one of the most important mechanical properties for EESs. Lipolmi *et al.* have fabricated transparent conductive films of PEDOT:PSS on a poly(dimethoxysiloxane) (PDMS) substrate, and they have been able to stretch the films up to 188% strain and still retain significant conductivity[26].

Several kinds of materials and process combinations have been used to fabricate skin-mountable temperature sensors. Furthermore, polymer materials have been used in the fabrication of highly sensitive temperature sensors. Screen printed PEDOT:PSS/CNT temperature sensors were able to reach Temperature Coefficient of Resistance (TCR or α) as high as ~0.61% per degree Celsius[27]. Inkjet-printed temperature sensors, based on carbon and PEDOT:PSS, has been reported to achieve TCR value of 0.25% per degree Celsius[28]. Also other polymers, such as polyaniline nanofibers, have been used to fabricate temperature sensors. Hong *et al.* have been able to manufacture sensors using electrochemical polymerization deposited polyaniline on a PET substrate achieving a 1.0% per degree Celsius sensitivity[29]. Even though these polymer sensors had good sensitivities, they were fabricated on a flexible but not on a stretchable substrate. Temperature sensors have also been fabricated onto stretchable substrates, but by utilizing more conventional fabrication techniques. Chen *et al.* fabricated sputtered Au/Cr temperature sensors on semipermeable stretchable film (Opsite, Smith & Nephew) and the TRC of this device was 0.002778 per degree Celsius[14]. Young *et al.* used a so-called cut-and-paste method with thermal evaporated gold on a PET substrate. The gold pattern was transferred onto the target substrate, which could be a temporary tattoo paper (Silhouette) or a medical tape, such as 3M Tegaderm transparent dressing[9]. However, a new material and manufacturing process combination is required so that the high sensitivity of the polymer material can be combined with a simple fabrication method and still be able to use stretchable substrates.

To simplify the manufacturing process, but at the same time to enable the use of polymer materials with high sensitivities for epidermal electronic systems, we have developed a fabrication method for inkjet-printed graphene/PEDOT:PSS temperature sensors. The choice of the graphene/PEDOT:PSS composite was done based on previous case studies that were performed in our lab that shed light on the electrical properties of the ink and the potential for stretchable applications[30–31]. The compatibility of the ink composite (Innophene Phene plus I3015) for inkjet printing was also studied independently by other groups, providing further rationale for the ink's suitability for our needs[32]. For instance, PEDOT:PSS has already being proven to have high temperature sensitivity and Honda *et al.* presented in their research that CNT/PEDOT:PSS composition ink had higher sensitivity than CNT or PEDOT:PSS itself[33]. The higher sensitivity was explained to most likely result from electron hopping at the interface of PEDOT:PSS and CNTs. Similar to the role of the CNTs, the graphene flakes in the PEDOT:PSS matrix provides a means for printable, bendable, conductive films[34].

Our fabrication process utilizes additive printing methods, and thus provides an opportunity to fabricate low-cost and material sparing EESs compatible with disposable devices. In this study, inkjet-printed graphene/PEDOT:PSS temperature sensors with stretchable silver conductors were fabricated on top of a stretchable polyurethane substrate with native adhesive. Just like a bandage, stretchable polyurethane substrates can be used to simulate the mechanical and surface properties of human skin[35]. The main topic is to present a novel fabrication method compatible with stretchable materials but no stretching tests are included in this article. Subsequently, the samples were characterized in ambient and inert atmosphere to analyse their resistance as a function of
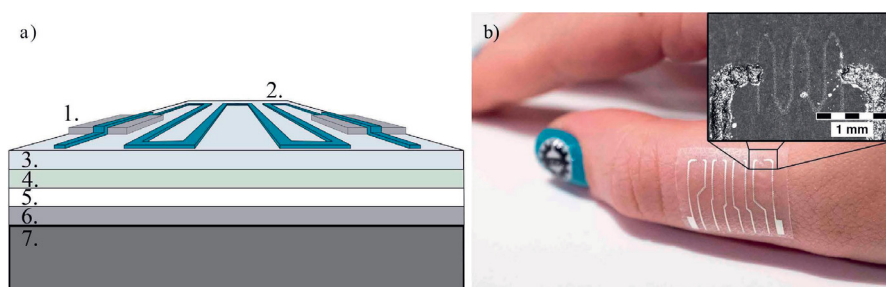
Figure 1. (**a**) Temperature sensor has a multilayered structure of printed functionalities and different bandage layers. Different components are: 1. Screen printed silver conductors, 2. wave patterned graphene/PEDOT:PSS temperature sensor, 3. PU surface layer, 4. adhesive layer, 5. protective paper, 6. PET film and 7. cooling/heating element. (**b**) Photograph of the sample, with sensor array of four sensors, being attached to the skin.
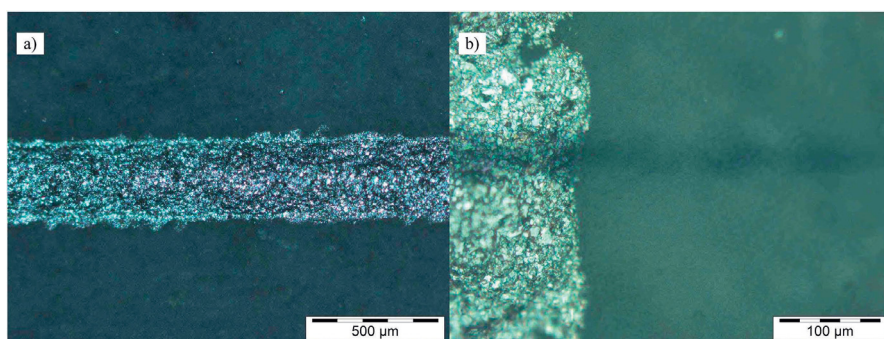
Figure 2. Optical microscope pictures of (**a**) printed silver conductor and (**b**) printed graphene/PEDOT:PSS (horizontal) line crossing the printed silver conductor (vertical line).

temperature. Through these measurements, the influence of ambient air was illustrated. Hence, three samples were coated with a fluorochemical acrylic polymer material to prevent, as much as possible, moisture and oxygen from affecting the results. Electrical measurements were repeated after coating to observe the effect of encapsulation.

Results and Discussion

Printing process.   Figure 1(a) shows the final multilayered structure of the printed temperature sensors. The topmost layers are the printed functional structures with screen printed silver conductors and inkjet-printed graphene/PEDOT:PSS temperature sensors. The functional layers were printed on top of an adhesive bandage (plaster), which had polyurethane (PU) surface and polyacrylate adhesive layer. The bottom layer of the plaster was a protective paper, which prevents the adhesive layer from adhering before it is required. The plaster, with printed functionalities, was then placed on top of a polyethylene terephthalate (PET) sheet which provided good mechanical support so that damage during handling was reduced. Figure 1(b) shows the final device attached to the skin.

Figure 2(a) presents an optical microscope picture of the stretchable silver conductor, whose conductivity under strain was evaluated in a recent study[36]. The line width for the silver conductor was approximately $320\,\mu m$. The cross section of the screen printed silver conductor (vertical line) and the inkjet-printed graphene/PEDOT:PSS sensor can be seen in Fig. 2(b). The width of the graphene/PEDOT:PSS sensor was approximately $32\,\mu m$ and the wetting on top of the polyurethane surface was fairly good. Printing the sensors were done so that the long lines of the sensors were formed in cross-process direction to give some time for the droplets to dry before the next sweep. The printing stability and repeatability of the graphene/PEDOT:PSS ink was good as long as the printing was done continuously. Printing pauses tend to clog the print head nozzles and the best printing stability was achieved with new, freshly filled print heads. If clogging occurred, wiping the nozzle plate with ethanol proved to be the best cleaning procedure.

Electrical characterization.   The initial resistance values were $8.7\,k\Omega$, $9.4, k\Omega$ and $9.7\,k\Omega$ for the three characterized samples before the temperature cycling measurements. During measurements, the samples were heated from $35\,°C$ to $45\,°C$ and then cooled back down to $35\,°C$, using a Peltier element. Human skin temperature may
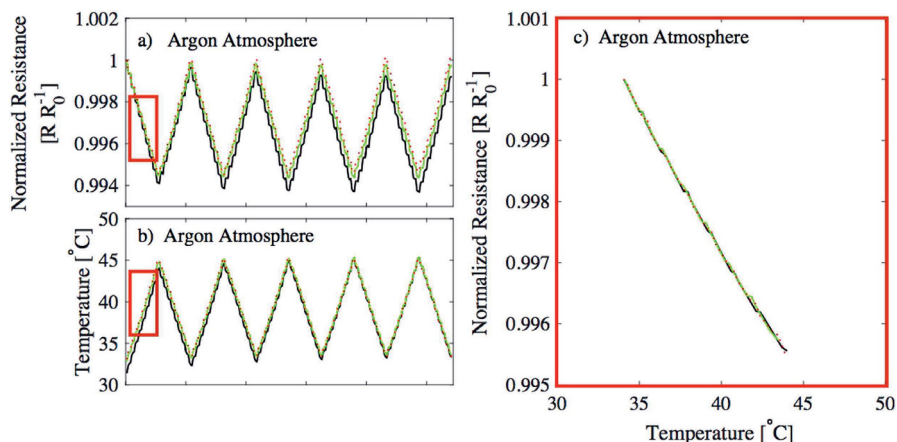
Figure 3. (**a**) normalized resistance and (**b**) temperature from three different samples measured in argon atmosphere. Temperature was increased and decreased between 35 °C and 45 °C along the measurements and this cycling was done five times for each sample. (**c**) The measured data from (**a,b**) is transformed in form of normalized resistance as a function of temperature during the first increase from 34 °C to 44 °C.
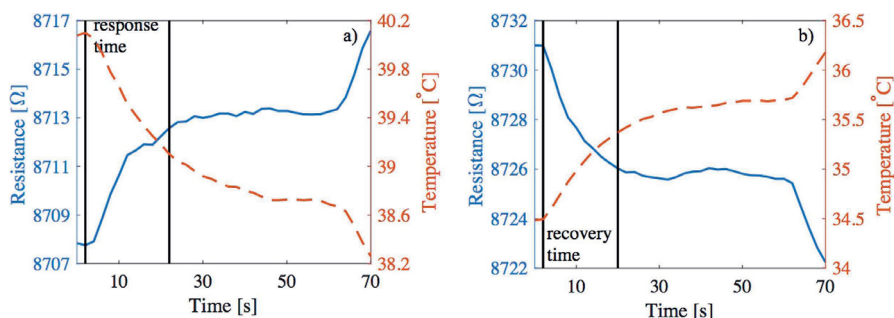

Figure 4. One cooling step (**a**) and one heating step to visualize the response time and the recovery time. The 90 percentile response time was 20 seconds and the 90 percentile recovery time was 18 seconds. The resistance is plotted using a solid line and the temperature is plotted with a dashed line.

vary depending on the skin location, ambient temperature and possible infection caused fever[37–38]. The utilized temperature range in the experiments was chosen due to environmental testing constraints whilst being within the possible temperature deviations on top of the human epidermis.

The temperature cycle was repeated five times for each sample and results from the measurements are presented in Fig. 3. The electrical characterization was conducted in an inert argon atmosphere to minimize the impact of ambient atmosphere factors, such as oxygen or moisture. Figure 3(a) shows normalized resistance and (b) corresponding temperature measurements from three different samples in individual graphs. Resistance decreases when the temperature increases, as was expected according to the other studies done with PEDOT:PSS and graphene, and with other nanostructural carbon/PEDOT:PSS composites, thus graphene/PEDOT:PSS behaves as a negative temperature coefficient (NTC) material[25,39–40]. Figure 3(c) presents the same results as in Fig. 3(a,b), during the first increase in temperature (from 34 °C to 44 °C), but in this figure, the normalized resistances are shown as a function of temperatures. Those parts of the measurements, where the data is collected for Fig. 3(c), are marked with red rectangles in Fig. 3(a,b). The average TCR of the samples, according to the measurements, is 0.047% per degree Celsius.

Figure 4 presents a response time and a recovery time for one sample. In Fig. 4(a) the input voltage of the Peltier element is decreased by 0.2 V and is then kept unaltered for 1 minute. More detailed description about the measurements can be found from the Methods section. The 90 percentile response time was 20 seconds with this Peltier element setup. It needs to be noticed that the Peltier element also has a response time which reflects to the response time of the temperature sensor. Figure 4(b) shows a 90 percentile recovery time of 18 seconds for the sensor when the Peltier voltage is increased by 0.2 V.
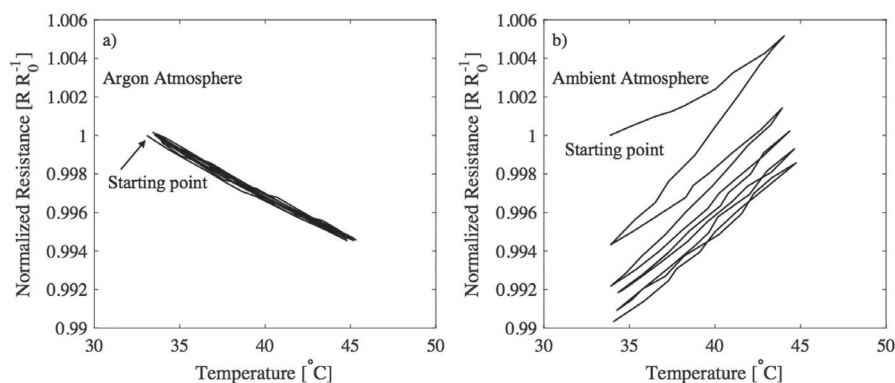
Figure 5. Sample characterized first in (**a**) argon and then moved to (**b**) ambient atmosphere.

Figure 5(a) shows the results from Fig. 3, but now the normalized resistance from one sample is expressed as a function of temperature from all five temperature cycles. Characterization results from all three samples can be found from Supplementary Information (Figure S1). The results show that the temperature sensors exhibit linear NTC behaviour in this temperature range, and the level of hysteresis stays very low. After confirming the functionality in inert atmosphere, the samples were removed from the glove box for additional measurements. Figure 5(b) presents the normalized resistance as a function of temperature in ambient atmosphere. A dramatic divergence can be observed with the non-encapsulated sample's behaviour relating not only to the slope but also the hysteresis. The slope of the resistance vs. temperature plot turns from negative to positive, which implies that the sensor no longer behaves as an NTC thermistor. This indicates that the device's temperature sensing ability is skewed by other environmental factors, like humidity. Similarly, humidity has been proven to have an effect on other organic conductors like polyaniline and CNT/PEDOT:PSS nanocomposites[41–42]. Likewise, our sensor which utilizes PEDOT:PSS as the conductive matrix and graphene to increase conductivity, is also greatly affected by water vapour. This phenomena was also utilized when Kuberský *et al.* fabricated a humidity sensor using PEDOT:PSS, and they expressed that the change in impedance is based on the dissociation of OH groups in PSS chain and the formation of free charge carriers in PEDOT chain[43]. In fact, it was recently shown that PEDOT:PSS films act as a mixed ionic-electronic conductor and exhibit a variation in its charge transport property as the humidity level is altered[44,45]. Furthermore, Nardes *et al.* found that the conductivity of pristine PEDOT:PSS increases by nearly one order of magnitude at 50% relative humidity, as compared to dry films[46]. These studies illustrate that in dry PEDOT:PSS films the charge transport is primarily electronic in nature, whereas the films with elevated water content exhibit an ionic charge transport mechanism. These previous literature results, support the observed effect in our unprotected sample (Fig. 5b) that exhibits a decrease in the organic film's conductivity as the relative humidity is reduced (via increased temperature). When our samples are removed from the glove box they slowly begin to absorb the ambient water throughout the characterization cycles. As the cycles progress, the overall moisture content of the sample increases and subsequently reduces the overall resistance of the sample. However, even as this secondary effect stabilizes over time, the general trend remains the same; as the temperature is increased there is decreased conductivity as the relative moisture content decreases. This provides further evidence that humidity dramatically affects the PEDOT:PSS/graphene film and that outside the glove box the primary charge transport mechanism is ionic and inside the glove box the dry films charge transport is electronic in nature.

The results above show that ambient conditions had a severe impact on the results, and for that reason, Novec 1700 Electronic Grade Coating (EGC) coating was used to encapsulate the sensors to reduce the effects of ambient atmosphere. EGC coating provides efficient moisture, chemical and corrosion protection[47]. Three sensors were coated with the EGC and these samples went through the same temperature cycling as in the previous measurements (5 times from 35 °C to 45 °C and back to 35 °C). These characterization results of the coated samples are presented in Fig. 6. Figure 6 shows results only from one sample, and the characterization results from all three samples can be found from Supplementary Information (Figure S2). From Fig. 6(a) it can be seen that the results from measurements done in the inert argon atmosphere after the samples were coated with the EGC. These results illustrated a TRC value of 0.064% per degree Celsius among the samples. Like the previous trials, the samples were then moved from the glove box in an ambient atmosphere and subsequently characterized again (Fig. 6). In this scenario, the sensitivity dropped down to 0.034% per degree Celsius and exhibited an increased hysteresis, however, but the device's resistance versus temperature was not divergent from the behaviour of the device characterized in a dry environment. This implies that there is a mixed electronic and ionic conductive mechanism, with the former being the primary action of charge transport. Moreover, the reason why the sensors did not function identically in an argon atmosphere and in an ambient air environment, although they were covered with electronic grade coating, is that the coating is only dispensed directly on top of the sensing area. A picture illustrating the covered areas is presented in the Supplementary Information (Figure S3). The ambient atmosphere (i.e. humidity) can still affect the sensors through the bandage material, both from above and underneath the substrate, which is permeable to water and other compounds. The substrate material was chosen so that
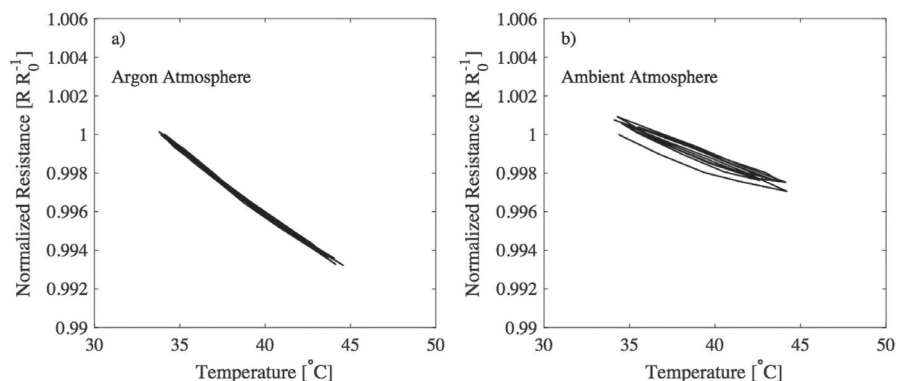
Figure 6. After coating the sample with EGC it was characterized both in (**a**) argon and (**b**) ambient atmosphere.

it would be able to be attached to the skin (medical grade material) and for that reason adding additional coating material on the underside of the substrate was not suitable. In the future, studies to find a more efficient encapsulation to improve the sensor's behavior under ambient atmospheric conditions will be performed.

Conclusions

The materials and fabrication processes presented in this paper, enable simple and straightforward fabrication method for inkjet-printed temperature sensors compatible with epidermal electronic systems. Ideally, the printed sensors are targeted for disposable systems, due to the decreased number of fabrication steps and reduced amount of waste material, compared to the traditional lithography processed devices. The sensors were fabricated with inkjet-printed graphene/PEDOT:PSS ink and screen printed silver flake ink. Temperature sensors were printed on top of a skin-formable bandage type substrate, which also provides good adhesion to skin. The completed electronic system is light-weight, thin, and can seamlessly integrate with the skin. The device has the possibility to monitor temperature changes directly on human skin with a TRC value higher than 0.06% per degree Celsius under optimal conditions (35–45 °C). The ambient atmosphere had a severe impact to the results of non-encapsulated devices, nevertheless, the effects not associated with temperature could be reduced using a fluoropolymer coating. The device does not yet compete in efficiency with already existing temperature sensors but the device could be used in its present form as a simple fever indicator on human skin (normal skin temperature about 33 °C). This is due to the simple fabrication process, which enables low-cost fabrication of epidermal electronics with the added value of disposability. Scalable and simple manufacturing process combined with the stretchable, functional materials makes it possible to manufacture epidermal temperature sensors, which are comfortable to use with an excellent skin/device interface.

Methods

Substrate preparation.   Transparent plasters, adhesive bandages, (Hansaplast) were used as a substrate for the graphene/PEDOT:PSS temperature sensors. These plasters have a transparent PU top layer and an adhesive polyacrylate layer underneath the PU. There is a wound pad, made of PU with hydrocolloid, at the centre of the plasters. This wound pad was cut out from the plasters and only the flat outer sections were used. The plasters were unwrapped from their packaging so that only the supportive film was removed on top of the plaster, and this revealed the outermost PU layer from the plasters. The protective paper underneath the adhesive was kept in place. Pieces of plaster were then attached to Melinex ST506 PET (Teijin DuPont Films) sheet to provide mechanical support during the printing and characterization. This was done to keep the samples unaltered and to prevent possible changes in the structures, and hence the resistance, due to handling.

Screen printing process.   Silver conductors were screen printed using TIC SCF-300 screen printer and CI-1036 stretchable silver ink (ECM). The silver ink contains 50–60 wt% silver flakes and 1–5 wt% polymer material diluted in a diethylene glycol ethyl ether acetate solvent. Pattern was defined by a polyester screen with a mesh count of 79 threads cm^{-1}, mesh opening of 69 μm, and stretching angle of 22,5°. Printed silver conductors were annealed in the convection oven at 130 °C for 13 minutes.

Inkjet printing and coating process.   Temperature sensors were inkjet-printed on the plasters using a Phene Plus I3015 transparent graphene/PEDOT:PSS ink (Innophene). The ink contains 1–5 wt% graphene, the same amount of PEDOT:PSS, and a small amount of diethylene glycol and ethanol (according to the manufacturer). A Dimatix Materials Printer DMP-2831 with a 10 pl drop volume print head was used for the ink deposition. Three layers of graphene/PEDOT:PSS ink with 1270 dpi printing resolution, which equates to 20 μm drop spacing, were printed to fabricate the temperature sensors. The printing process was optimized in a way that the highest possible resistance (to overcome resistance from wires, contacts and other parasitic sources) was achieved with high yield. Three layers with 20 μm drop spacing formed conductive sensors repeatedly. Bringing the layer

count down to two decreased the yield significantly and increasing the layer count to four decreased the resistance unnecessarily. Using identical printing parameters for each sample, which all had uneven substrates, caused some variation in sensor resistances. Both the printing plate temperature and the print head temperature were kept at 40 °C. After printing, the sensors were cured in a convection oven at 130 °C for 10 minutes. Three samples were coated with Novec 1700 Electronic Grade Coating (EGC) material (3M). EGC was deposited via pipette on top of the sensors in an argon atmosphere, and subsequently dried at room temperature.

Electrical characterization setup.   To assess the resistance dependence on temperature, a resistance measurement setup was used together with a heating/cooling unit. In the resistance measurement setup, a LabVIEW system design software driven digital multimeter in a VirtualBench (National Instruments) measured the resistance of the samples with a 4.3 Hz sampling rate. VirtualBench also drove the heating/cooling unit, which consisted of a Peltier element and Silverstone Tundra TD03 liquid cooler that kept one side of the Peltier at a constant room temperature. TC-08 Thermocouple Data Logger (Pico Technology) was used to measure the temperature of the plaster surface.

During the electrical characterization of non-encapsulated samples, VirtualBench increased and decreased the Peltier voltage stepwise using 0.2 V steps and the voltage was kept constant for 1 min. For EGC-coated samples the temperature was kept constant for 30 seconds. The temperature cycling fluctuated approximately between 35 °C and 45 °C, and complete cycles (increase from 35 °C to 45 °C and decrease form 45 °C to 35 °C) were done five times for each sample. Electrical measurements were done both in ambient conditions and under inert (argon) atmosphere.

References

1. Priego Quesada, J. I. *et al.* Relationship between skin temperature and muscle activation during incremental cycle exercise. *J. Therm. Biol.* **48,** 28–35 (2015).
2. Sawka, M. N., Cheuvront, S. N. & Kenefick, R. W. High skin temperature and hypohydration impair aerobic performance. *Exp. Physiol.* **97,** 327–332 (2012).
3. Houghton, V. J., Bower, V. M. & Chant, D. C. Is an increase in skin temperature predictive of neuropathic foot ulceration in people with diabetes? A systematic review and meta-analysis. *J. Foot Ankle Res.* **6,** 31–31 (2013).
4. Addor, G. *et al.* A comparative study of reactive hyperemia in human forearm skin and muscle. *Physiol. Res.* **57,** 685–692 (2008).
5. Sillanpää, H. *et al. In Proc. of Electronic System and Technology Conference (ESTC)*, Helsinki, Finland, Sept. 16–18 (2014).
6. Yang, G. *et al.* Bio-Patch Design and Implementation Based on a Low-Power System-on-Chip and Paper-Based Inkjet Printing Technology. *IEEE Trans Inf Technol Biomed* **16,** 1043–1050 (2012).
7. Yeo, W. *et al.* Multifunctional Epidermal Electronics Printed Directly Onto the Skin. *Adv. Mater.* **25,** 2773–2778 (2013).
8. Webb, R. C. *et al.* Thermal Transport Characteristics of Human Skin Measured *In Vivo* Using Ultrathin Conformal Arrays of Thermal Sensors and Actuators. *PLoS One* **10,** e0118131 (2015).
9. Yang, S. *et al.* "Cut-and-Paste" Manufacture of Multiparametric Epidermal Sensor Systems. *Adv. Mater.* **27,** 6423–6430 (2015).
10. Kim J. *et al.* Epidermal electronics with advanced capabilities in near-field communication. *Small* **11,** 906–912 (2015).
11. Son, D. *et al.* Multifunctional wearable devices for diagnosis and therapy of movement disorders. *Nat. Nanotechnol.* **9,** 397–404 (2014).
12. Webb, R. C. *et al.* Ultrathin conformal devices for precise and continuous thermal characterization of human skin. *Nat. Mater.* **12,** 938–944 (2013).
13. Yao, S. & Zhu, Y. Nanomaterial-Enabled Stretchable Conductors: Strategies, Materials and Devices. *Adv. Mater.* **27,** 1480–1511 (2015).
14. Chen, Y., Lu, B., Chen, Y. & Feng, X. Breathable and Stretchable Temperature Sensors Inspired by Skin. *Sci. Rep.* **5,** 11505, 10.1038/srep11505 (2015).
15. Bandodkar, A. J., Nuñez-Flores, R., Jia, W. & Wang, J. All-Printed Stretchable Electrochemical Devices. *Adv. Mater.* **27,** 3060–3065 (2015).
16. Chun, K. Y. *et al.* Highly conductive, printable and stretchable composite films of carbon nanotubes and silver. *Nat. Nanotechnol.* **5,** 853–857 (2010).
17. Guo, C. F. *et al.* Highly stretchable and transparent nanomesh electrodes made by grain boundary lithography. *Nat. Commun.* **5,** 3121, 10.1038/ncomms4121 (2014).
18. Matsuhisa, N. *et al.* Printable elastic conductors with a high conductivity for electronic textile applications. *Nat. Commun.* **6,** 7461, 10.1038/ncomms8461 (2015).
19. Fallahzadeh, A., Saghaei, J. & Saghaei, T. Ultra-smooth poly(3,4-ethylene dioxythiophene):poly(styrene sulfonate) films for flexible indium tin oxide-free organic light-emitting diodes. *JOL* **169,** Part A, 251–255 (2016).
20. Zhang, X. *et al.* Highly conductive PEDOT:PSS transparent electrode prepared by a post-spin-rinsing method for efficient ITO-free polymer solar cells. *Sol. Energ. Mat. Sol. Cells* **144,** 143–149 (2016).
21. Xu, G.-L. *et al.* PEDOT-PSS coated ZnO/C hierarchical porous nanorods as ultralong-life anode material for lithium ion batteries. *Nano Energy* **18,** 253–264 (2015).
22. Lee, K. Y. T., Shi, H. H., Lian, K. & Naguib, H. E. Flexible multiwall carbon nano-tubes/conductive polymer composite electrode for supercapacitor applications. *Smart Mater. Struct.* **24** (2015).
23. Culebras, M., López, A. M., Gómez, C. M. & Cantarero, A. Thermal sensor based on a polymer nanofilm. *Sens. Actuators A-Phys* **239,** 161–165 (2016).
24. Takano, T. *et al.* T. PEDOT Nanocrystal in Highly Conductive PEDOT:PSS Polymer Films. *Macromolecules* **45,** 3859–3865 (2012).
25. Zhou, J. *et al.* The temperature-dependent microstructure of PEDOT/PSS films: insights from morphological, mechanical and electrical analyses. *J. Mater. Chem. C* **2,** 9903–9910 (2014).
26. Lipomi, D. J. *et al.* Electronic Properties of Transparent Conductive Films of PEDOT:PSS on Stretchable Substrates. *Chem. Mater.* **24,** 373–382 (2012).
27. Honda, W. *et al.* Wearable, Human-Interactive, Health-Monitoring, Wireless Devices Fabricated by Macroscale Printing Techniques. *Adv. Func. Mater.* **24,** 3299–3304 (2014).
28. Bali, C. *et al.* Fully Inkjet-Printed Flexible Temperature Sensors Based on Carbon and PEDOT:PSS. *Materials Today: Proceedings* **3,** 739–745 (2016).
29. Hong, S. Y. *et al.* Stretchable Active Matrix Temperature Sensor Array of Polyaniline Nanofibers for Electronic Skin. *Adv. Mater.* **28,** 930–935 (2016).
30. Vuorinen, T. *et al.* Printable, Transparent, and Flexible Touch Panels Working in Sunlight and Moist Environments. *Adv. Func. Mat.* **24,** 6340–6347 (2014).

31. Tuukkanen, S. *et al.* Stretching of solution processed carbon nanotube and graphene nanocomposite films on rubber substrates. *Synth. Met.* **191,** 28–35 (2014).
32. Žlebič, Č. *et al.* Electrical properties of inkjet printed graphene patterns on PET-based substrate. *In 38th International Spring Seminar on Electronics Technology (ISSE),* 414–417 (2015).
33. W. Honda, S. *et al.* Printed wearable temperature sensor for health monitoring. *IEEE SENSORS* 2014 Proceedings, (2014).
34. Hong, W. *et al.* Transparent graphene/PEDOT–PSS composite films as counter electrodes of dye-sensitized solar cells. *Electrochem. Commun.* **10,** 1555–1558 (2008).
35. Dabrowska, A. K. *et al.* Materials used to simulate physical properties of human skin. *Skin. Res. Technol.* **22,** 3–14 (2016).
36. Suikkola, J. *et al.* Screen-Printing Fabrication and Characterization of Stretchable Electronics. *Sci. Rep.* **6,** 25784, 10.1038/srep25784 (2016).
37. Webb, P. Temperatures of skin, subcutaneous tissue, muscle and core in resting men in cold, comfortable and hot conditions. *Eur. J. Appl. Physiol. Occup. Physiol.* **64,** 471–476 (1992).
38. Ng, E. Y. K., Kawb, G. J. L. & Chang, W. M. Analysis of IR thermal imager for mass blind fever screening. *Microvasc. Res.* **68,** 104–109 (2004).
39. Benchirouf, A. *et al.* Electrical properties of multi-walled carbon nanotubes/PEDOT:PSS nanocomposites thin films under temperature and humidity effects. *Sens. Actuator B-Chem.* **224,** 344–350 (2016).
40. Kong, D., Le, L. T., Li, Y., Zunino, J. L. & Lee, W. Temperature-dependent electrical properties of graphene inkjet-printed on flexible materials. *Langmuir* **28,** 13467–13472 (2012).
41. Ryu, H., Cho, S. J., Kim, B. & Lim, G. A stretchable humidity sensor based on a wrinkled polyaniline nanostructure. *RSC Adv* **4,** 39767 (2014).
42. Benchirouf, A. *et al.* Electrical properties of multi-walled carbon nanotubes/PEDOT:PSS nanocomposites thin films under temperature and humidity effects. *Sens. Actuator B-Chem.* **224,** 344–350 (2016).
43. Kuberský, P. *et al.* Printed Flexible Gas Sensors based on Organic Materials. *Procedia Eng.* **120,** 614–617 (2015).
44. Ail, U. *et al.* Thermoelectric Properties of Polymeric Mixed Conductors. *Adv. Func. Mat.* 10.1002/adfm.201601106 (2016).
45. Wang, H., Ail, U., Gabrielsson, R., Berggren, M. & Crispin, X. Ionic Seebeck Effect in Conducting Polymers. *Adv. Energy Mater.* **5,** (2015).
46. Nardes, A. M. *et al.* Conductivity, work function, and environmental stability of PEDOT:PSS thin films treated with sorbitol. *Organic Electronics* **9,** 727–734 (2008).
47. Halonen, E. *et al.* Environmental protection of inkjet-printed Ag conductors. *Microelectron Eng.* **88,** 2970–2976 (2011).

Acknowledgements

Author Contributions

T.V. was responsible for designing and fabricating the samples, designing and conducting the experiments, analysing the data, and writing the manuscript. J.N. contributed to design and fabrication of the samples, as well as experimental methodology and device characterization. T.K. was responsible for assembling the electrical measurement unit and for programming the measurement software. T.M.K. contributed to analysis of data and revision of the manuscript. M.M. contributed to design of experiments and analysis of the results.

Additional Information

Supplementary information accompanies this paper at http://www.nature.com/srep

Competing financial interests: The authors declare no competing financial interests.

How to cite this article: Vuorinen, T. *et al.* Inkjet-Printed Graphene/PEDOT:PSS Temperature Sensors on a Skin-Conformable Polyurethane Substrate. *Sci. Rep.* **6**, 35289; doi: 10.1038/srep35289 (2016).